

Porous nanoparticle assemblies with enhanced properties for application in electrochemical thin film devices

Dissertation

Presented to the department of Biology/Chemistry, University of Osnabrück in partial fulfillment of the requirements for the degree of 'Doctor Rerum Naturalium'

submitted by

Jonas Klein

Osnabrück
March 2023

1st Reviewer: Prof. Dr. Markus Haase
2nd Reviewer: Prof. Dr. Martin Steinhart

Abstract

Porous structures of functional nanoparticles have several properties that are beneficial for their potential applications in optical devices. Structures of this kind can be created in the form of nanoparticle thin films on electrically conductive substrates for electrochemical applications. Mesoporous layers of antimony doped tin dioxide (ATO, $\text{SnO}_2:\text{Sb}$) nanoparticles, for example, can serve as an optically transparent scaffold, providing electrical conductivity over a broad potential range. Such conductive structures allow electrons to be transported to/from other electrochemically active materials located at the surface of the particles. In electrochromic devices, materials are used that change their optical behavior by oxidation/reduction. It is shown that layers composed of ATO particles with anchored viologen-based redox dyes exhibit remarkable switching times and good long-term stability. Both aspects are related to the rather unusual use of non-intercalating electrolytes, which can be used due to the intrinsic conductivity of ATO. In addition to the optically active layer, a charge storage layer is required in an electrochromic device to achieve high performance. For this purpose, ATO layers can be modified with cerium species that can be switched between +3 and +4 redox states. These layers offer high charge storage capacities with fast response times also in combination with non-intercalating electrolytes. In addition to nanoparticle layers that mainly provide electrical conductivity, the nanoparticles themselves can also have variable properties that depend on the redox state of the atoms in the particles. $\text{LaPO}_4:\text{Ce},\text{Tb}$ nanoparticles can be mentioned as an example where the redox state of the cerium atoms influences the luminescence of the particles. Small amounts of Ce^{4+} quench the luminescence otherwise exhibited by the particles when the cerium atoms are in the +3 oxidation state. With the help of redox shuttles, the luminescence of non-conductive $\text{LaPO}_4:\text{Ce},\text{Tb}$ nanoparticle layers can be reversibly switched with impressive switching times. The properties of porous structures of functional nanoparticles are, however, not only beneficial for optical devices but also for the synthesis of nanomaterials that show their properties only after calcination at high temperatures. One example is the n-type conductivity of ATO where the particle aggregates formed during calcination cannot be further processed into colloidal solutions. With respect to the latter, it is shown herein that nanoparticle aerogels are suitable for suppressing the formation of large aggregates of nanoparticles during the calcination process. In particular, by assembling aerogels from ATO (and titanium dioxide, TiO_2) nanoparticles, colloidal solutions of these particles can be prepared even after calcination at 500 °C.

Zusammenfassung

Poröse Strukturen funktionaler Nanopartikeln haben viele Eigenschaften, die für ihre potenzielle Anwendung in optischen Devices vorteilhaft sind. Für elektrochemische Anwendungen lassen sich Strukturen dieser Art in Form von Nanopartikel-Dünnschichten auf elektrisch leitenden Substraten erzeugen. So können beispielsweise mesoporöse Schichten aus antimondotierten Zinndioxid (ATO, $\text{SnO}_2:\text{Sb}$) Nanopartikeln als optisch transparente Gerüste dienen, welche elektrische Leitfähigkeit über einen weiten Potentialbereich bieten. Solche leitfähigen Strukturen erlauben es Elektronen zu/von anderen elektrochemisch aktiven Materialien, welche sich an der Oberfläche der Partikel befinden, zu transportieren. In elektrochromen Devices werden Materialien verwendet welche durch Oxidation/Reduktion ihr optisches Verhalten ändern. Es wird gezeigt, dass ATO-Schichten mit verankerten, viologenbasierten Redox-Farbstoffen bemerkenswerte Schaltzeiten und eine gute Langzeitstabilität aufweisen. Beide Aspekte stehen im Zusammenhang mit der eher ungewöhnlichen Verwendung von nicht interkalierenden Elektrolyten, die aufgrund der intrinsischen Leitfähigkeit von ATO eingesetzt werden können. Neben der optisch aktiven Schicht wird in einem elektrochromen Device eine Ladungsspeicherschicht benötigt. Für diesen Zweck können ATO-Schichten mit Cer-Spezies modifiziert werden, die zwischen den Redox-Zuständen +3 und +4 umgeschaltet werden können. Diese Schichten bieten hohe Ladungsspeicherkapazitäten mit schnellen Schaltzeiten, auch in Kombination mit nicht interkalierenden Elektrolyten. Neben Nanopartikel-Schichten, die elektrisch leitend sind, können diese selbst auch veränderbare Eigenschaften aufweisen, die vom Redox-Zustand der Atome in den Partikeln abhängen. $\text{LaPO}_4:\text{Ce},\text{Tb}$ -Nanopartikel können als Beispiel genannt werden bei welchen der Redox-Zustand der Cer-Atome die Lumineszenz der Partikel beeinflusst. Geringe Mengen an Ce^{4+} löschen die Lumineszenz, die sonst von den Partikeln gezeigt wird, wenn die Cer-Atome in der Oxidationsstufe +3 sind. Mit Hilfe von Redox-Shutteln kann die Lumineszenz von nicht leitenden $\text{LaPO}_4:\text{Ce},\text{Tb}$ -Nanopartikelschichten reversibel mit beeindruckenden Schaltzeiten geschaltet werden. Die Eigenschaften poröser Strukturen sind allerdings nicht nur für optische Devices interessant, sondern auch für die Synthese von Nanomaterialien welche ihre Eigenschaften nur nach Kalzination bei hohen Temperaturen erhalten. Ein Beispiel ist die n-Leitfähigkeit von ATO bei welchem die Partikel-Aggregate, die während dem Kalzinieren entstehen, sich nicht zu kolloidalen Lösungen weiterverarbeiten lassen. In Bezug auf Letzteres wird gezeigt, dass sich Nanopartikel-Aerogele dazu eignen, die Bildung großer Aggregate von Nanopartikeln während Kalzinierungsverfahren zu unterdrücken. Durch die Herstellung von Aerogelen aus ATO- (und Titandioxid-, TiO_2) Nanopartikeln können kolloidale Lösungen dieser Partikel auch nach der Kalzinierung bei 500 °C erhalten werden.

Contents

Abstract	I
Zusammenfassung	II
1 Introduction	1
2 Theoretical background	4
2.1 Functional nanomaterials	4
2.1.1 Preparation	4
2.1.2 Doped nanoparticles	7
2.1.3 Colloidal nanoparticle solutions	13
2.1.4 Nanoparticle thin films	16
2.2 Electrochromism	21
2.3 Aerogels	24
2.3.1 Gelation	26
2.3.2 Aging and solvent exchange	28
2.3.3 Drying	28
3 Dispersible SnO₂:Sb and TiO₂ nanocrystals after calcination at high temperature	30
3.1 Introduction	31
3.2 Experimental	32
3.3 Results and discussion	34
3.4 Conclusion	44
4 Intercalation-free, fast switching of mesoporous antimony doped tin oxide with cathodically coloring electrochromic dyes	45
4.1 Introduction	46
4.2 Experimental	48
4.3 Results and discussion	50
4.4 Conclusion	59

Contents

5 Cerium-modified mesoporous antimony doped tin oxide as intercalation-free charge storage layers for electrochromic devices	60
5.1 Introduction	61
5.2 Experimental	63
5.3 Results and discussion	64
5.4 Conclusion	75
6 Photo-electrochemical device enabling luminescence switching of LaPO₄:Ce,Tb nanoparticle layers	76
6.1 Introduction	77
6.2 Experimental	77
6.3 Results and discussion	79
6.4 Conclusion	84
7 Summary	86
Appendix	89
References	93
List of publications	112
Declaration of authorship	114

1 Introduction

A wide range of materials can be prepared as particles with relatively small dimensions (< 100 nm), and the study of their properties represents a dynamic field of research^[1,2]. One particular aspect of these nanoparticles is related to their very high surface-to-volume ratios, which raise their attraction for a variety of applications^[3,4]. For the present thesis, highly porous frameworks of solid nanoparticles are of special interest since they provide large internal surface areas^[5,6]. Electrochemical devices benefit from such structures, for example in the form of thin films on conductive substrates^[7-9]. In many cases, nanoparticles can also be dispersed into solvents as individual entities in such a way that they are resilient against aggregation^[10,11]. Being able to produce such colloidal solutions is advantageous for the characterization of the nanoparticles and the fabrication of the aforementioned thin films. From the wide range of accessible nanosized materials, nanocrystals that gain their functionality through the integration of dopant ions were chosen for this work. The first type are electrically conductive nanoparticles, specifically antimony doped tin oxide (ATO, $\text{SnO}_2:\text{Sb}$). While SnO_2 is a semiconductor with a large bandgap and low electrical conductivity at room temperature, it can become conductive via doping with suitable ions. These include antimony ions, as they have a higher valence (+5) than the tin ions (+4), which results in the presence of free electrons in the nanoparticle conduction band that account for the electrical conductivity^[12,13]. The focus of the second type of employed nanoparticles is related to their optical properties. Due to the doping of LaPO_4 nanoparticles with both Ce^{3+} and Tb^{3+} ions, they exhibit luminescent properties, i.e., they absorb ultra-violet light and emit visible green light^[14,15]. This work is divided into multiple chapters in which the preparation of the nanoparticles, their colloids, and their properties as porous structures are investigated. The contents of the individual projects are as follows:

1. For a large number of materials, full functionality is only achieved through a calcination process. However, calcination without appropriate safeguards generally results in aggregates of sintered particles with dimensions much larger than the primary particle size. Because the aggregates cannot usually be re-dispersed, this is a serious problem for the preparation of stable colloidal solutions of such materials. Because ATO is a high-temperature material, the first project focuses on the synthesis of small (< 5 nm), re-dispersible ATO nanoparticles. A strategy based on porous aerogels that allows for the re-dispersion of calcined nanoparticles is also presented. The appearance of colloidal solutions of ATO particles treated at different temperatures demonstrates the importance of calcination steps. In this case, calcination produces more free electrons, which are the origin of a plasmon absorption band in the infrared region.

2. Mesoporous metal oxide layers with anchored organic dye molecules are widely investigated for electrochromic devices. The key requirements for such layers are high transparency in the visible spectrum as well as fast electron transport throughout the layer. Titanium dioxide (TiO_2) is the standard mesoporous scaffold material used to anchor organic electrochromic dye molecules like cathodically coloring viologens. TiO_2 displays a particularly high performance when small cations, e.g., lithium, are present in the electrolyte. Under negative polarization, however, metal oxides like TiO_2 are known to intercalate lithium, which can lead to degradation of the nanoparticle layer owing to the mechanical stress associated with intercalation. Long-term stability, therefore, benefits from electrolytes with non-intercalating cations. In this regard, it is demonstrated that mesoporous ATO layers prepared from small particles with low antimony doping concentration outperform TiO_2 when non-intercalating electrolytes are used. This is particularly evident from the performance of a full device composed of two symmetrical ATO layers, each equipped with a complementary redox-active dye molecule.

3. To further explore the use of ATO in combination with non-intercalating electrolytes, the third project is concerned with the so-called counter electrode that provides the charge that is consumed by the coloring ATO/viologen electrode presented in the second project. For this purpose, modification of nanoparticle mesoporous layers is not only restricted to organic molecules. CeO_2 is a typical example of an inorganic material that is used as a charge storage layer in electrochromic devices. However, these types of materials also are commonly used with intercalating cations and are thus again susceptible to degradation due to the intercalation of these cations. Making use of the broad potential range in which ATO layers offer electrical conductivity, it is shown that the layers can be decorated with cerium species that can be oxidized/reduced at the surface of the nanoparticles. As a result, these layers can store significantly more charge compared to a bare ATO layer. A device combining an ATO/viologen and an ATO/Ce layer also shows promising performance.

4. Another nanomaterial containing cerium ($\text{LaPO}_4\text{:Ce,Tb}$ nanoparticles) is the subject of the last project. Nanocrystals of the material display strong luminescence. Oxidation of the Ce^{3+} ions at the particle surface to Ce^{4+} results in complete quenching of the luminescence, as shown by several groups using chemical oxidizers. Reducing agents restore the luminescence by converting Ce^{4+} back to Ce^{3+} . Using the same mechanism in an electrochemical device for on/off switching of the luminescence, however, was hitherto impossible because of the very low electrical conductivity of $\text{LaPO}_4\text{:Ce,Tb}$ electrode layers. In batteries, similar problems have been solved by embedding nanocrystalline electrode materials in carbon black or other conductive ma-

Introduction

terials. The same approach could not be applied here, however, due to the interfering optical properties of carbon black (i.e. its strong absorption). In this work, this problem was solved by introducing special optically transparent redox shuttles, i.e., small organic molecules dissolved in the electrolyte, enabling electron transfer between the current collector and the $\text{LaPO}_4:\text{Ce,Tb}$ nanoparticles. The redox potentials of the shuttles are chosen to allow oxidation and reduction of the cerium ions at the particle surface. The incorporation of this system into a complete device enables switching the luminescence of a $\text{LaPO}_4:\text{Ce,Tb}$ nanocrystal electrode layer via the applied potential.

2 Theoretical background

2.1 Functional nanomaterials

Nanoparticles are assemblies of atoms, ions, molecules, or polymers, with the resulting entities having a size in the range of 1–100 nm^[16]. The nanoparticles used in the work presented here are small inorganic crystals with dimensions in the low nanometer regime. Due to their small size, these nanocrystals exhibit large surface-to-volume ratios, as the surface region contains the majority of the atoms that therefore encounter a different chemical environment compared to the atoms that are located in the core of the particles. As a consequence, nanocrystals may inherit characteristic properties that differ from the macroscopic material^[17]. Additionally, nanoparticles may be accessible in a variety of geometric shapes, which gives further tools to tune their properties^[18,19]. Therefore, nanoparticles are attractive for a variety of applications. For instance, due to their small size, energy storage materials allow faster charging due to shorter diffusion path lengths^[20,21]. Large surface areas and the presence of defects in the nanoparticle surface layer account for improved behavior in the field of catalysis^[22,23]. Further, nanoparticles offer desired properties in biological applications, which include drug delivery, treatment of diseases, the imaging of structures, and the tracking of processes^[24–26].

2.1.1 Preparation

Due to the increasing interest in nanoparticles, a variety of methods have been utilized and optimized for their preparation. Depending on the method, nanoparticles with different characteristics may be obtained. These mainly relate to factors such as size, size distribution, shape/morphology, crystallinity, composition, or dispersibility. A selection of common approaches for the preparation of nanoparticles includes the following:

Ball milling: If the desired material is accessible in the form of a macroscopic powder, a process that breaks the material down into smaller units may yield nanoparticles. The ball milling process, schematically displayed in Figure 2.1, commonly achieves this. Here, the macrocrystalline powder is loaded into a chamber along with a grinding medium, such as metal balls. When the chamber is rotated, the force exerted on the primary particles due to collisions results in the division of the primary particles into smaller segments^[27]. Parameters such as rotation speed, time, number of balls, and others, influence the properties of the obtained nanoparticles^[28].

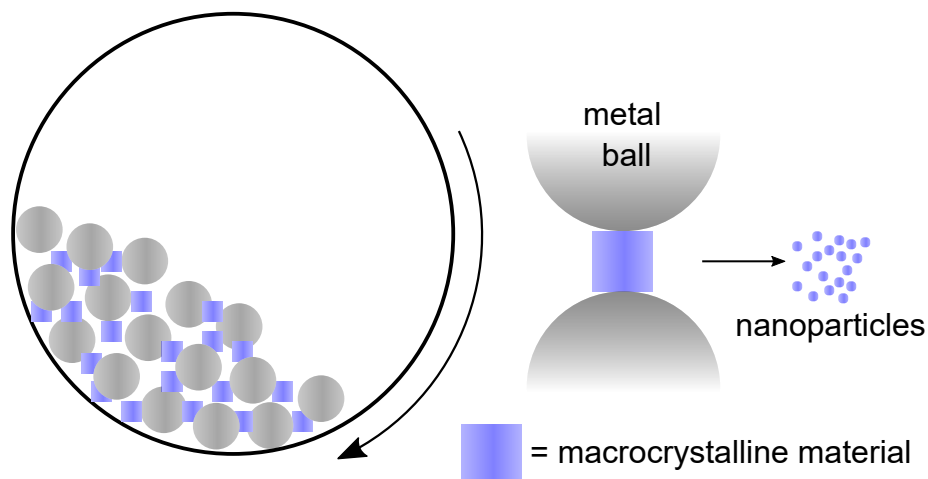


Figure 2.1: Schematic illustration of the ball milling process.

Thermal combustion: The procedure by which nanoparticles are prepared via thermal combustion is shown in Figure 2.2. Here, a solution containing the molecular precursors is initially prepared. Thereafter, the solvent is removed to yield a gel in which the precursors are well mixed. The formation of the particles is then induced by heating the gel at elevated temperatures^[29].

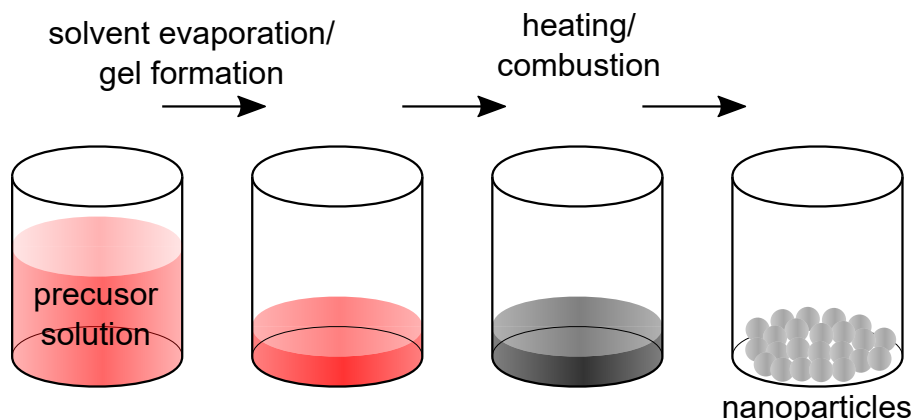


Figure 2.2: Schematic illustration of the preparation of nanoparticles via thermal combustion.

Vapor synthesis: Other typical procedures involve reactions of precursors in a vaporized state. A variety of methods have been used to vaporize the precursors, depending on the initial state of the precursors, e.g., if they are present as solids or as solutions. Simple heating or bombardment with ions may vaporize solid precursors^[30,31]. Precursor solutions, on the other hand, can be nebulized to obtain small droplets that are further subjected to high-temperature conditions^[32]. For the case of flame spray pyrolysis, this is depicted schematically in Figure 2.3. In either case, the vaporized state of the precursors is typically thermodynamically unstable, favoring nucleation and the formation of solid particulates^[33].

Theoretical background

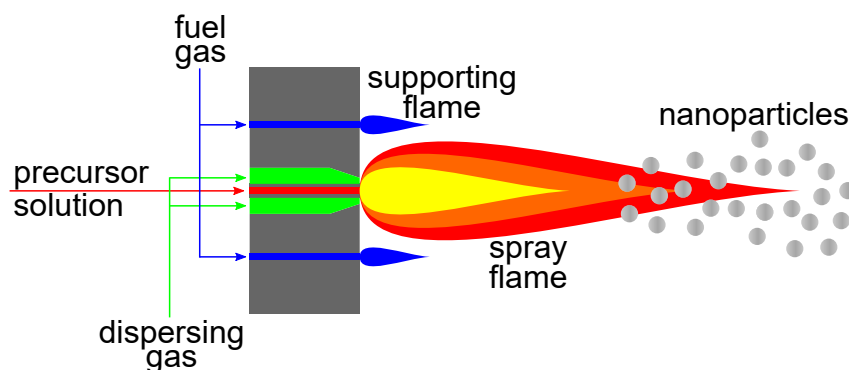


Figure 2.3: Schematic illustration of the preparation of nanoparticles via flame spray pyrolysis.

Solution processes: Finally, nanoparticles can be created through precursor reactions in a suitable solvent as the reaction medium. This category can also be subdivided into nanoparticle formation processes that rely on different mechanisms. Some of those reactions are schematically presented in Figure 2.4. Metallic nanoparticles are accessible via the addition of reducing agents to solutions of dissolved metal salts (path a in Figure 2.4)^[34]. In the case of aqueous precursor solutions, nanoparticles, especially

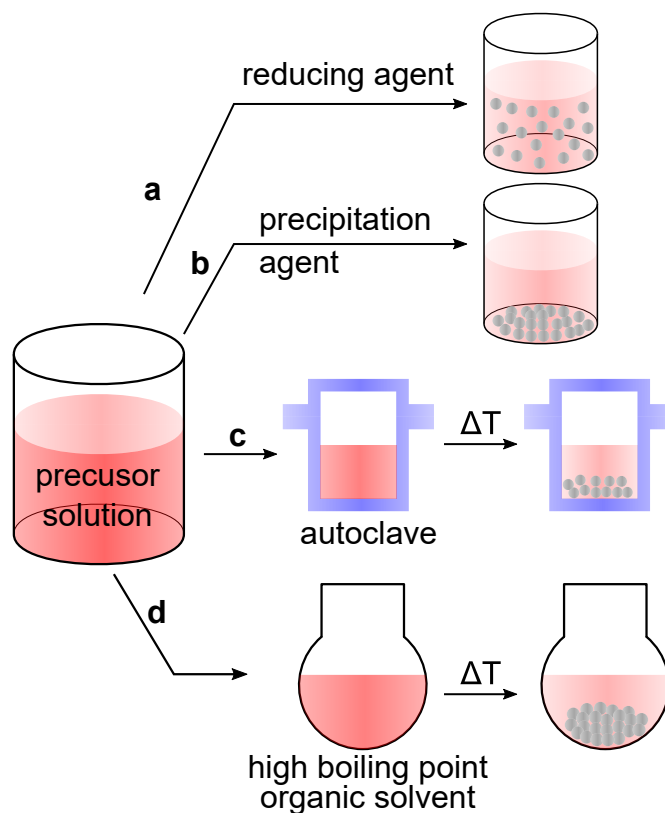


Figure 2.4: Schematic overview of preparation of nanoparticles in solution via a) addition of a reducing agent, b) addition of a precipitation agent, c) treatment in an autoclave, and d) heating in a high boiling point organic solvent.

those of metal oxides, can be readily synthesized by precipitation reactions through variations in the pH value of the solutions (path b in Figure 2.4)^[35]. Nanoparticle synthesis that relies on hydrolysis and condensation reactions is also very common and known as the sol-gel approach^[36]. The formation of nanoparticles also occurs when the precursor solutions are subjected to elevated temperatures and pressures in a sealed reaction chamber (path c in Figure 2.4)^[37]. These reactions are therefore typically performed in an autoclave. Finally, a variety of nanoparticles are accessible upon heating suitable precursors in organic solvents to temperatures typically in the range of 200–300 °C (path d in Figure 2.4)^[38].

2.1.2 Doped nanoparticles

The properties of nanoparticles can be tuned not only by varying their size or shape but also by a process termed doping. In this case, a fraction of the atoms that build the structure of the nanocrystals, the host lattice, are exchanged with foreign atoms, as displayed in Figure 2.5. Depending on the chemical nature of these atoms, doped nanoparticles might possess properties that are fundamentally different from those of undoped material. The effects of doping that are relevant for the research of the present thesis include n-conductivity, accompanied by plasmon absorption, and luminescence. Both of these phenomena are highlighted in the following sections.

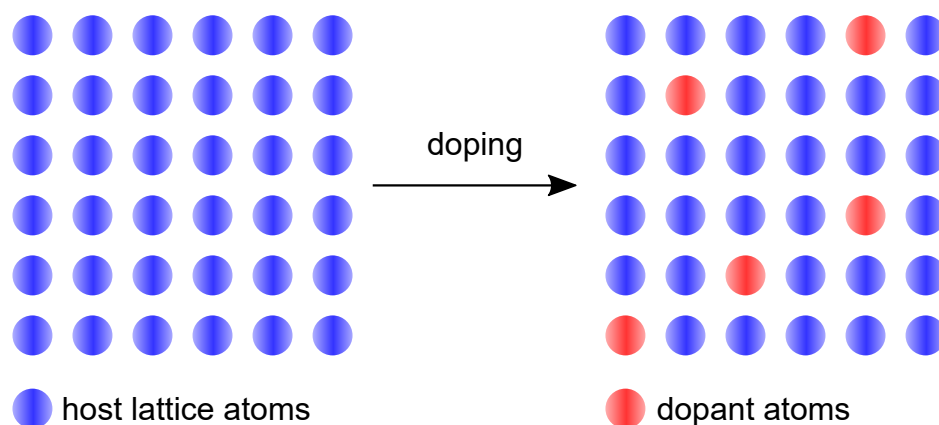


Figure 2.5: Schematic illustration of the replacement of atoms from a nanoparticle host lattice by dopant atoms.

n-conductivity and plasmon absorption

Semiconductors are of great interest for technical applications because of their specific electrical and optical properties. Semiconductors with a bandgap larger than 3 eV, for instance, show low absorption in the visible frequency spectrum^[39]. Several metal oxides, such as zinc oxide (ZnO), indium oxide (In₂O₃), titanium dioxide (TiO₂), and tin

Theoretical background

dioxide (SnO_2) exhibit these properties. While a large bandgap produces high transparency in the visible region, it also results in low electrical conductivity because the conduction band cannot be thermally populated. However, the electrical conductivity of semiconductors can be significantly increased by the incorporation of appropriate dopant ions leading to electron donor states near the conduction band of the material (Figure 2.6)^[40].

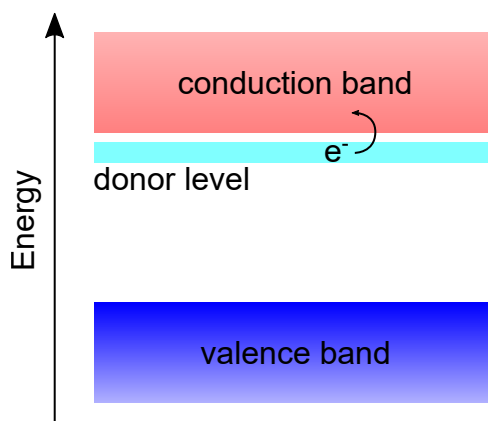


Figure 2.6: Schematic representation of the formation of donor levels near the conduction band of semiconductor nanoparticles due to n-doping.

Already at room temperature, the electrons in these donor states can be thermally excited to populate the conduction band, thereby providing mobile charge carriers. The effect of this doping mechanism is referred to as n-conductivity and the class of n-conductive oxides is known as transparent conductive oxides (TCO). In the case of the oxides listed above, n-conductivity is commonly achieved by doping with ions of higher valence. For instance, some of the Zn atoms in ZnO may be replaced by Al, Ga, or In atoms to yield aluminum doped zinc oxide (AZO), gallium doped zinc oxide (GZO), and indium doped zinc oxide (IZO), respectively^[41]. In the popular indium tin oxide (ITO), Sn atoms occupy In^{3+} sites^[42]. With TiO_2 , Nb, Mo, and W are commonly used^[43]. Doping of SnO_2 can be achieved by either replacing Sn sites with Sb (antimony doped tin oxide, ATO)^[44] or by replacing O^{2-} ions with F^- ions (fluorine doped tin oxide, FTO)^[45]. In all these cases, the dopant atom contains one more valence electron than the host atom. Achieving charge neutrality within the nanoparticles requires the presence of free electrons that compensate for the additional positive charge of the ionized dopant ion. The free electrons give rise to the n-conductive, at high dopant concentrations nearly metallic behavior. The electrical conductivity (σ) depends on the mobility (μ_e) of the electrons, their charge (e), and number density (n) as shown in equation 2.1.

$$\sigma = \mu_e \cdot n \cdot e \quad (2.1)$$

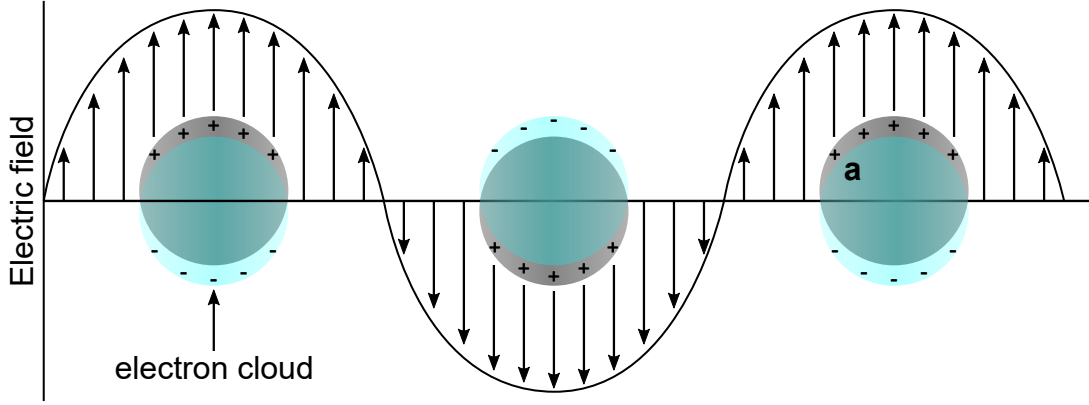


Figure 2.7: Illustration of the generation of localized surface plasmons in nanoparticles due to interaction of free electrons with the electric field of external radiation.

The presence of free electrons within nanoparticles not only influences their electrical properties but also accounts for a variation in their optical behavior. Subjecting such nanoparticles to external electromagnetic fields causes a displacement of the free electrons in the nanoparticle conduction band with respect to the immobile positive nuclei^[46]. In the case of small particles, whose diameters are smaller than the wavelength of the incident radiation, this creates a situation as displayed in Figure 2.7. Here, one side of the particle is negatively charged, and the opposite side is positively charged. This displacement accounts for a restoring force, based on Coulomb interactions, that results in collective oscillations of the free electrons and thereby creates an electric field in close proximity to the nanoparticle surface. The collective oscillation of electrons is referred to as plasmons. With nanoparticles, these can be specified as localized surface plasmons (LSP) based on the charges that are created at the nanoparticle surface. As a consequence, the nanoparticles absorb light with wavelengths that correspond to the resonance frequency of the plasmons^[47]. Experimentally obtained absorption spectra of such particles typically feature a plasmon absorption band as schematically depicted in Figure 2.8. From these measurements, two characteristic features can be extracted. First, the position of the plasmon absorption band, more precisely the frequency of the absorption maximum (ω_{\max}). This frequency may be written as:

$$\omega_{\max} = \frac{\omega_{\text{bulk}}}{\sqrt{2\epsilon_m + \epsilon^\infty}} \quad (2.2)$$

where ϵ_m and ϵ^∞ are the dielectric constant of the surrounding medium and the high-frequency dielectric constant of the material, respectively, and ω_{bulk} is the materials bulk plasma frequency^[48]. The latter can be expressed as:

$$\omega_{\text{bulk}} = \sqrt{\frac{n \cdot e^2}{\epsilon_0 \cdot m^*}} \quad (2.3)$$

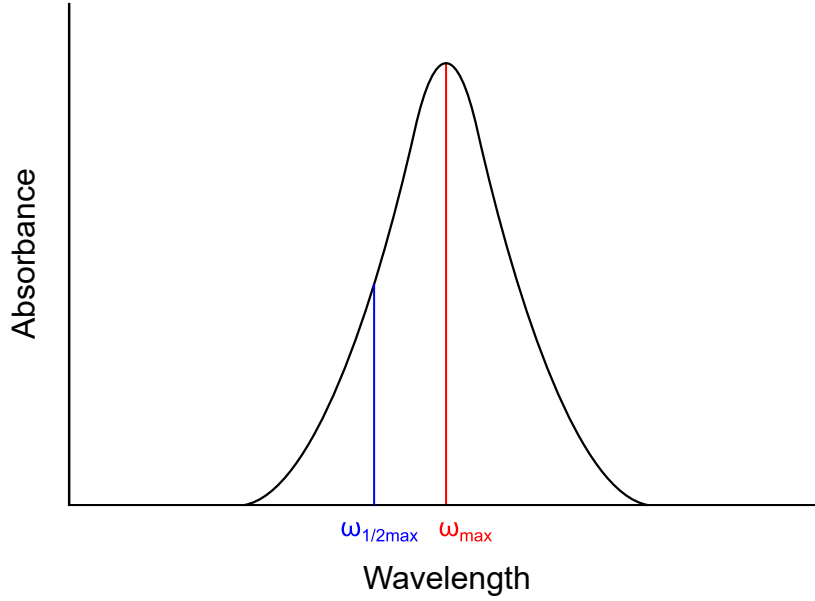


Figure 2.8: Schematic representation of a plasmon absorption band.

Here, e , n , and m^* are the charge, concentration, and effective mass of the free electrons, respectively, while ϵ_0 refers to the vacuum permittivity^[49]. Thus, the density of free electrons is primarily responsible for the position of the plasmon band. Metallic nanoparticles, especially gold and silver nanoparticles, are well known for their optical properties that are based on plasmon absorption^[50]. Since these materials have a very high density of free electrons, their absorption maxima are found in the visible frequency range. In the case of doped semiconductors, on the other hand, the plasmon band is usually located in the near-infrared region since they contain fewer free electrons. With the frequency of the absorption maximum and the frequency at half of the absorption maximum ($\omega_{1/2max}$), the damping frequency Γ may be expressed as:

$$\Gamma = \left| \frac{\omega_{1/2max}^2 - \omega_{max}^2}{\omega_{1/2max}} \right| \quad (2.4)$$

This damping frequency is related to the velocity (v_f) and the mean free path length (l) of the conduction band electrons^[51]:

$$\Gamma = \frac{v_f}{l} \quad (2.5)$$

Overall, tuning the absorption properties of the nanoparticles is also possible by varying other parameters. These include particle size^[52], shape^[53], and the refractive index of the surrounding material^[54].

Luminescence

Another method is to alter the optical properties of nanoparticles by doping their crystal lattice with luminescent ions. Luminescence refers to the emission of photons from atoms that are in an excited electronic state. In the specific case of photoluminescence, reaching the excited state is stimulated by the absorption of external radiation, usually from the ultraviolet (UV) and visible (VIS) spectrum^[55]. Trivalent rare-earth ions represent a very attractive choice as dopant luminescence ions since they have electrons located in the 4f orbitals. The latter are shielded by surrounding 5s and 5p orbitals and therefore account for a reduced crystal field splitting and low interactions with the lattice vibrations of the crystal, which are denoted as phonons. As a result, typical emission spectra of lanthanide ions feature narrow emission lines based on interconfigurational transitions between the f orbitals^[56]. The materials of interest for the present thesis are LaPO_4 nanoparticles, either co-doped with trivalent cerium (Ce^{3+}) and terbium (Tb^{3+}) or only doped with europium (Eu^{3+}). When excited with UV light (254 nm), colloidal solutions of these nanoparticles emit green ($\text{LaPO}_4:\text{Ce,Tb}$) or red ($\text{LaPO}_4:\text{Eu}$) light, as shown in Figure 2.9.

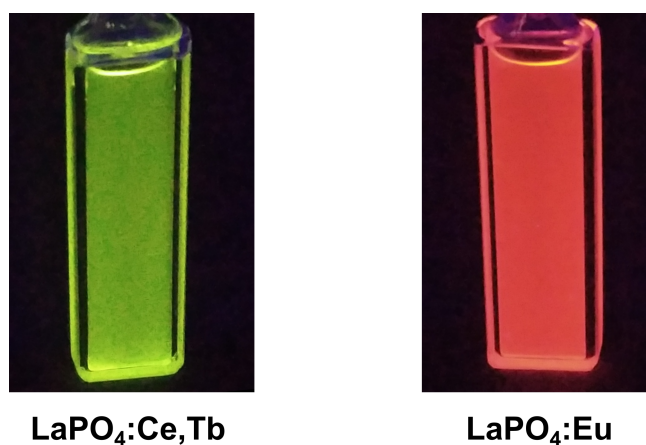


Figure 2.9: Images of colloidal $\text{LaPO}_4:\text{Ce,Tb}$ (left) and $\text{LaPO}_4:\text{Eu}$ (right) nanoparticle solutions under illumination with UV light (254 nm).

The origin of both emissions differs, depending on the choice of dopant ions, and will be briefly discussed in the following. In both cases, however, LaPO_4 is used as host material due to its chemical stability^[57]. Additionally, due to the similarity in ionic radii between the lanthanide ions, dopant ions can readily occupy La^{3+} sites. The luminescence mechanism of the $\text{LaPO}_4:\text{Ce,Tb}$ nanoparticles is displayed in Figure 2.10a. In this case, the Ce^{3+} ions are responsible for the absorption of external radiation, specifically UV light, which results in the excitation of the 4f electron into the 5d shell. Thereafter, the Ce^{3+} ion can return to its ground state either by the emission of radiation with

Theoretical background

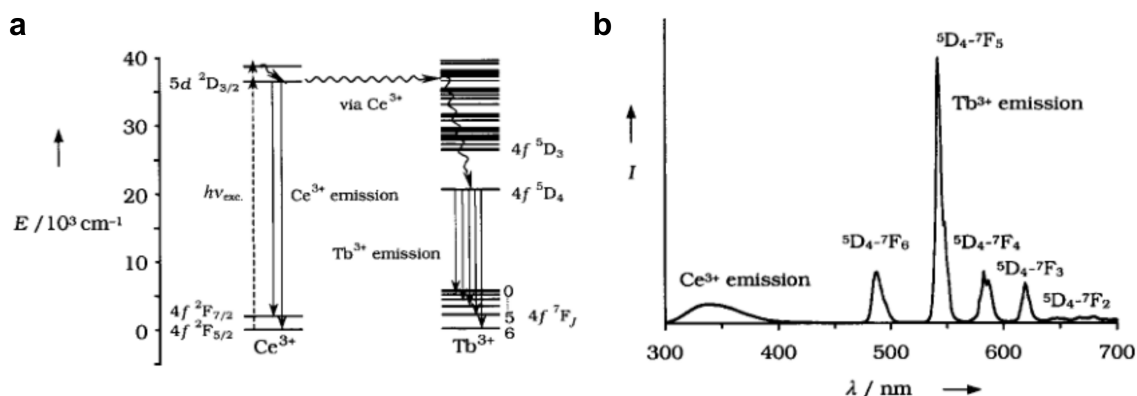


Figure 2.10: a) Schematic representation of the energy transfer between Ce^{3+} and Tb^{3+} in $\text{LaPO}_4:\text{Ce,Tb}$ nanoparticles. b) Emission spectra of $\text{LaPO}_4:\text{Ce,Tb}$ nanoparticles^[59].

wavelengths in the UV range or by the transfer of the excess energy to a Tb^{3+} ion. The latter phenomenon is known as Förster resonance energy transfer (FRET) and consequently yields an excited state of Tb^{3+} ions. Following non-radiative relaxation to the 5D_4 state, the Tb^{3+} emits light in the green spectral region based on transitions between the 5D_4 and 7F_J states. The highest emission intensity is observed at 542 nm (${}^5D_4-{}^7F_5$ transition)^[58]. Figure 2.10b shows the luminescence emission spectra of $\text{LaPO}_4:\text{Ce,Tb}$ nanoparticles that display a broad Ce^{3+} emission band in the UV range and distinct Tb^{3+} emission peaks. Thus, within these nanoparticles, the Ce^{3+} ions act as sensitizers (absorbing species), while the Tb^{3+} ions are the active emitting species (activator). For the present thesis, the $\text{LaPO}_4:\text{Ce,Tb}$ nanoparticles are of special interest since the emission of the particles can be quenched if the Ce^{3+} ions are partially oxidized to Ce^{4+} ^[60].

In the case of $\text{LaPO}_4:\text{Eu}$ nanoparticles, the Eu^{3+} ions are both responsible for absorption and emission. Figure 2.11a shows an excitation spectrum that displays distinct excitations between f orbitals and a broad absorption band at lower wavelengths

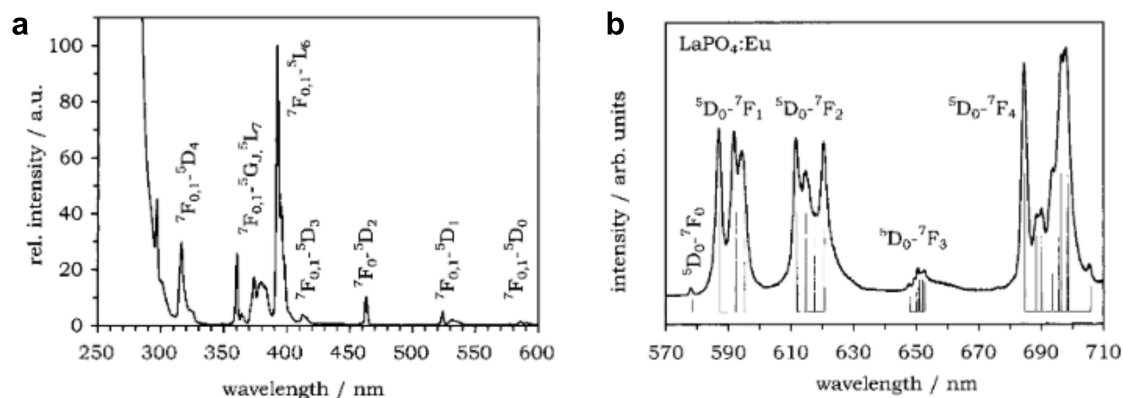


Figure 2.11: a) Excitation and b) emission spectra of $\text{LaPO}_4:\text{Eu}$ nanoparticles^[59].

that originates from a charge transfer between oxygen and europium ions^[61]. After radiationless relaxation, the emission of photons due to transitions between 5D_0 to 7F_J states occurs with wavelengths that correspond to the red region of the visible spectrum, as can be seen in the corresponding emission spectra of $\text{LaPO}_4:\text{Eu}$ nanoparticles displayed in Figure 2.11b.

2.1.3 Colloidal nanoparticle solutions

As previously outlined, nanoparticles possess unique properties that may be different from those of their respective bulk materials. An important difference is the large portion of their atoms located at their surface. For applications like catalysis and others, it is highly desired to have access to the complete surface of such nanoparticles, which in return requires them to be in a mainly single-particle, non-aggregated state^[62–64]. Additionally, having the nanoparticles in such a condition may also be favorable in post-processing steps, e.g., the formation of nanoparticle thin films^[65,66]. Well separated particles are commonly achieved by preparing colloidal solutions of the nanoparticles. Such colloids usually comprise a liquid phase as the main medium in which the solid nanoparticles are dispersed as single units^[67]. An important requirement of colloidal solutions concerns the stability of the nanoparticles against aggregation and sedimentation. In the case of uncharged particles, the main driving force responsible for the aggregation of particles in solution is based on long-range van der Waals interactions between the nanoparticles^[68]. As shown in Figure 2.12, induced dipoles cause their collective orientation, resulting in a net attraction of the particles.

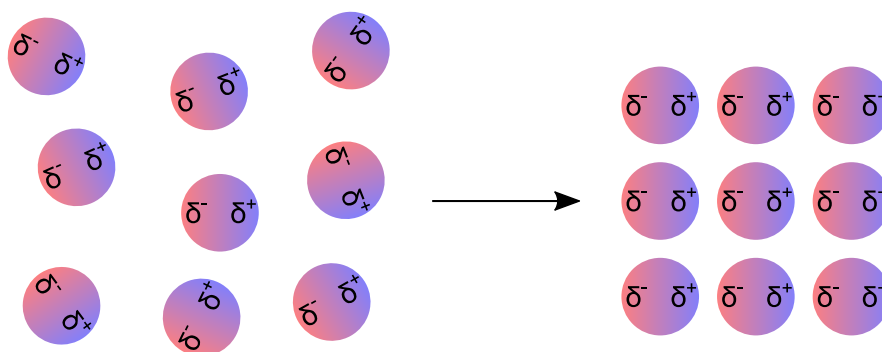


Figure 2.12: Schematic illustration of the collective orientation of nanoparticles due to induced dipoles.

Therefore, to achieve the desired stability, the attractive van der Waals forces have to be counteracted by repulsive forces. The two common approaches that are utilized to prepare colloidal nanoparticle solutions are based on electrostatic and steric stabilization. In the following, both of these mechanisms are briefly discussed.

Theoretical background

Electrostatic stabilization is possible when the surface of the nanoparticles is electrically charged, either positively or negatively. This mechanism is commonly realized by employing polar solvents as the dispersion medium for particles having a surface that can be, for instance, protonated and/or deprotonated. The effectiveness of this mechanism requires knowledge about the zeta potential of the particles, which usually depends on the pH value. As shown in Figure 2.13a, at low pH values, the particle surface may be positively charged and, consequently, exhibit a positive zeta potential. Typically, the value of the zeta potential should be greater than ± 30 mV to achieve colloidal stability^[69]. With increasing pH, the zeta potential drops (after a plateau region), reaching an uncharged state and finally regaining a stable region with negative values of the zeta potential. The pH at which the particle surfaces are uncharged is called the "point of zero charge" and presents the pH region in which the particles are most susceptible to aggregation. Charging of the nanoparticle surface results in the formation of an electrostatic double layer that consists of the surface-near Stern layer and a diffuse

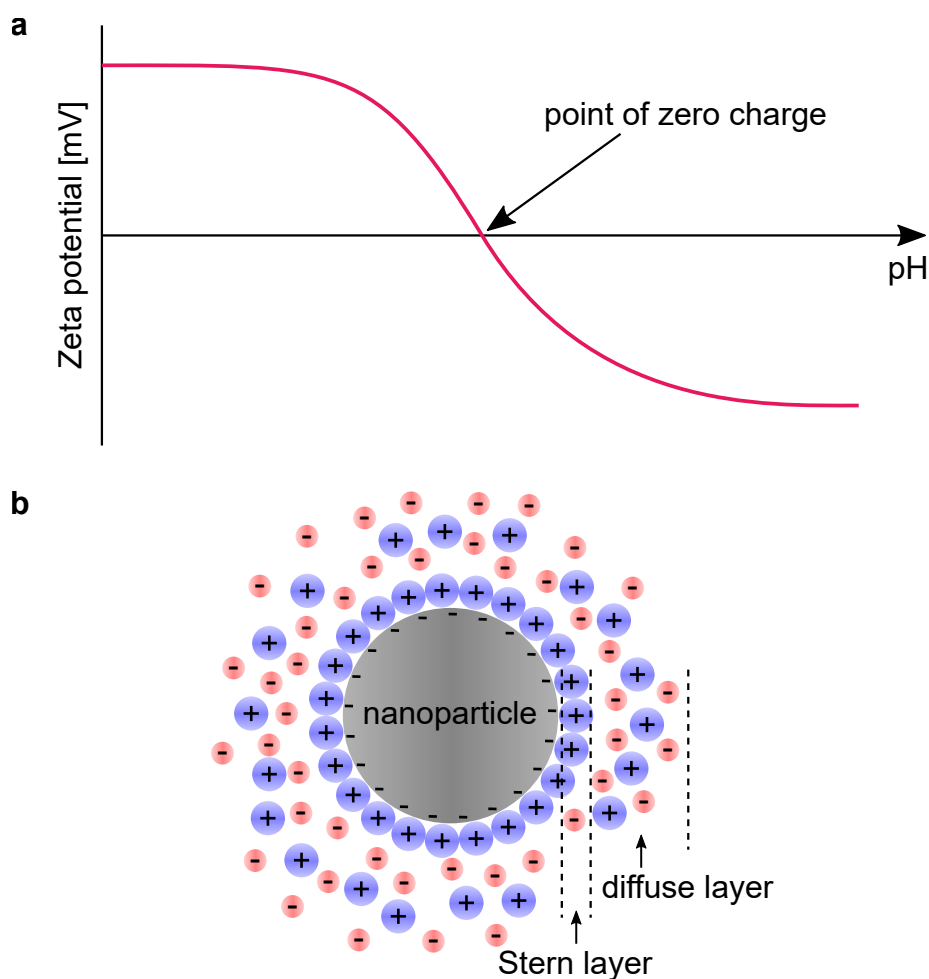


Figure 2.13: a) Schematic representation of the dependence of the zeta potential of a nanoparticle on the pH value. b) Schematic illustration of electrostatic nanoparticle stabilization.

Theoretical background

layer that extends more into the solvent (Figure 2.13b). Both of these layers comprise ions with opposite charges. Consequently, the collision of particles with the same surface charge gives rise to the repulsion of the particles and thereby accounts for colloidal stability^[70]. Charging of the nanoparticle surface, a process referred to as peptization, is usually realized by the addition of suitable ionic additives to the nanoparticle solution that adsorb onto the surface of the particles^[71,72].

The second stabilization mechanism, namely steric stabilization, relies on the coverage of the nanoparticle surface with molecules bearing long organic chains that extend into the periphery of the nanoparticle surface (Figure 2.14)^[73]. These molecules can either be in the form of polymers or monomers. Commonly applied polymers include, for example, polyvinylpyrrolidone^[74], polyacrylic acid^[75], and polyvinylalcohol^[76]. Depending on the intrinsic properties of the polymers, colloidal solutions may be prepared with both polar and non-polar solvents. With respect to the choice of suitable monomeric additives, molecules with a polar head group that anchors to the nanoparticle surface and a non-polar alkyl chain are commonly utilized. Here, oleic acid^[77] and oleylamine^[78] can be listed as popular candidates, especially for colloids in non-polar solvents. In either case, the desired repulsive forces may be based on the entropically unfavorable compression of the adsorbed molecules upon the collision of sterically stabilized nanoparticles. Further, the interpenetration of the organic chains between the nanoparticles is also thermodynamically unfavored^[79].

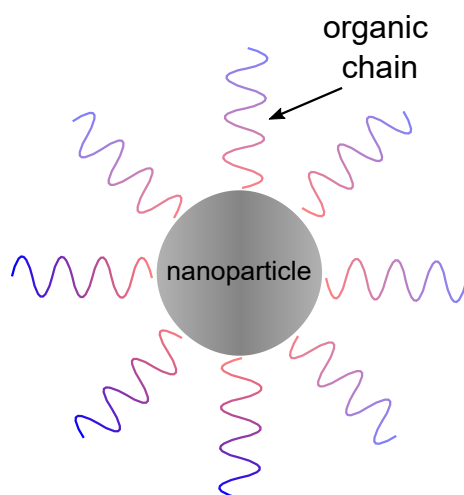


Figure 2.14: Schematic illustration of steric nanoparticle stabilization.

Regardless of the chosen stabilization mechanism, the overall resulting net force, as a function of the distance between nanoparticles, usually takes the form of the potential energy curve displayed in Figure 2.15.

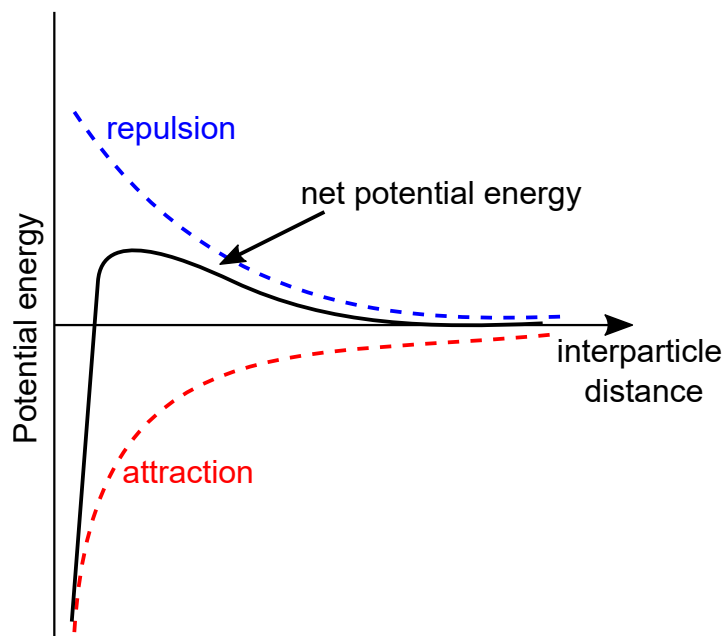


Figure 2.15: Schematic representation of the potential energy components of a nanoparticle as a function of the interparticle distance.

2.1.4 Nanoparticle thin films

Thin films consisting of functional nanoparticles present a highly investigated research field with a great range of potential applications. Among these are electrochromic devices^[80], solar cells^[81], optical coatings^[82], sensors^[83], energy storage systems^[84], and catalysts^[85]. Many of the applications make use of layers with a very high inner surface, i.e., nanoporous or mesoporous films of nanoparticles. Therefore, the preparation of such thin films is of great importance and can be achieved by a variety of methods. Some of the typical procedures are discussed below.

Drop casting: A very simple route to preparing nanoparticle thin films can be realized by drop-casting a solution containing the nanoparticles onto the desired substrate,

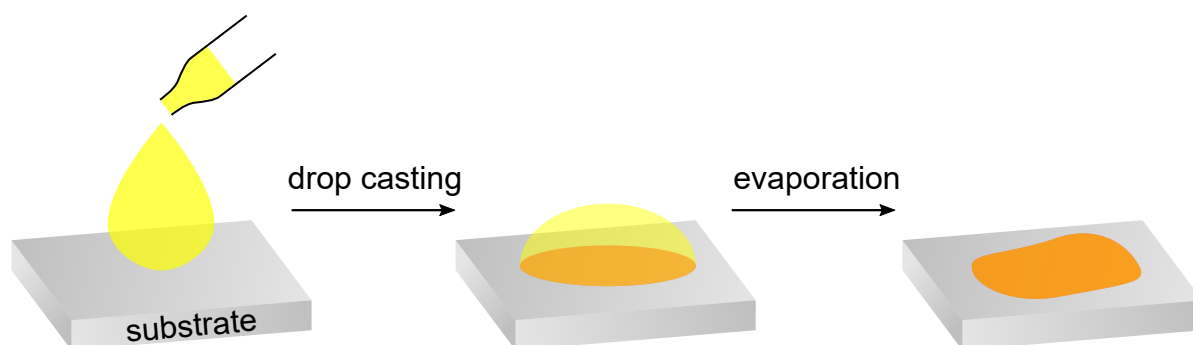


Figure 2.16: Schematic illustration of the drop casting process.

Theoretical background

followed by evaporation of the solvent (Figure 2.16)^[86]. However, films obtained by the drop-casting method usually suffer from inhomogeneity concerning the film thickness and morphology^[87], which makes the method only applicable to small areas.

Electrodeposition: Electrodeposition presents another capable method to obtain nanoparticle thin films. In this case, the substrate and a counter electrode are immersed in a solution of suitable precursors. These may be present in the form of preformed nanoparticles^[88] or molecular species^[89]. Film formation is then induced by the application of an electric field between the two electrodes with sufficient strength to cause the precursors to migrate to the surface of the substrate, where they are deposited (Figure 2.17). Electrodeposition also yields homogeneous films, whose thickness is readily adjustable by the period of time the electric field is applied.

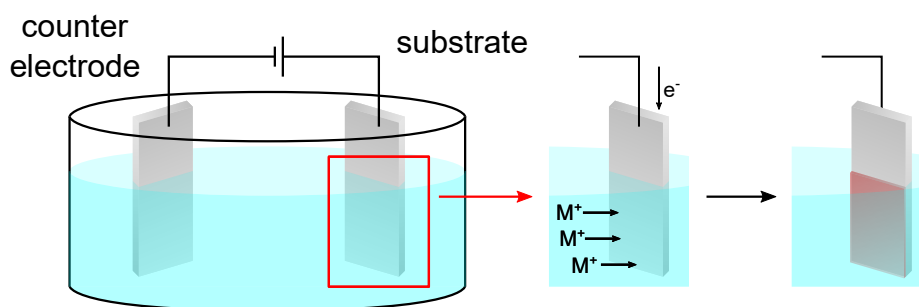


Figure 2.17: Schematic illustration of the electrodeposition process.

Layer-by-layer deposition: For the preparation of layers containing multiple types of nanoparticles that should be assembled in a controlled manner, a layer-by-layer approach can be applied (Figure 2.18) that is also commonly used with a variety of materials other than nanoparticles^[90]. Here, the thin film is grown by immersion of the substrate in a solution of the first type of nanoparticles to form a monolayer of these nanoparticles. After a washing step, the substrate is then immersed in a solution of the second type of nanoparticles, which should exhibit some form of attraction to the first type of nanoparticles. This can be achieved if the surfaces of the two types of nanoparticles are oppositely charged^[91]. While this method produces homogeneous films with controllable structures, the process is rather time-consuming since a large number of immersion cycles may be required to obtain thick layers.

Spray/vapor deposition: A class of preparation methods that produce thin films with very dense morphology is based on the transport of precursors through a gas phase to the substrate. Methods applying using this concept include chemical vapor deposition^[92], physical vapor deposition^[93], spray coating^[94], atomic layer deposition^[95],

Theoretical background

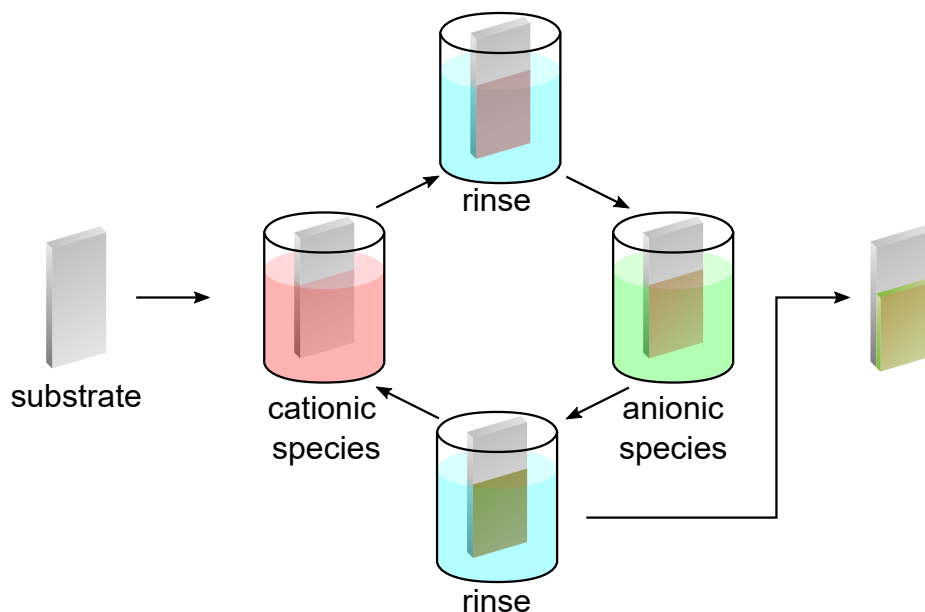


Figure 2.18: Schematic illustration of the layer-by-layer deposition process.

radio-frequency sputtering^[96], and spray pyrolysis^[97]. Especially the latter is commonly used for the preparation of transparent conductive oxides. The process is schematically depicted in Figure 2.19. Here, a precursor solution is transformed into an aerosol that is directed onto the heated target substrate. When the drops of the aerosol reach the surface of the substrate, the solvent evaporates and the precursors react to yield the desired material.

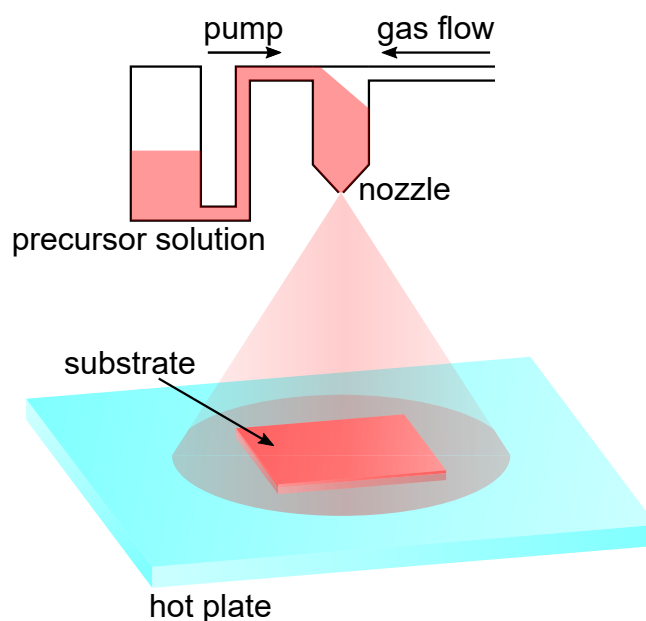


Figure 2.19: Schematic illustration of the spray pyrolysis process.

Theoretical background

Dip coating: Figure 2.20 displays the typical steps that are performed in the dip coating method. The process involves immersion of the substrate into the precursor/nanoparticle solution at a constant speed. Following a stationary period, the substrate is withdrawn from the solution, also at a constant rate. This process results in the formation of a film due to the evaporation of the solvent during the retraction of the substrate^[98]. After a drying step, the process can be repeated to achieve the desired layer thickness.

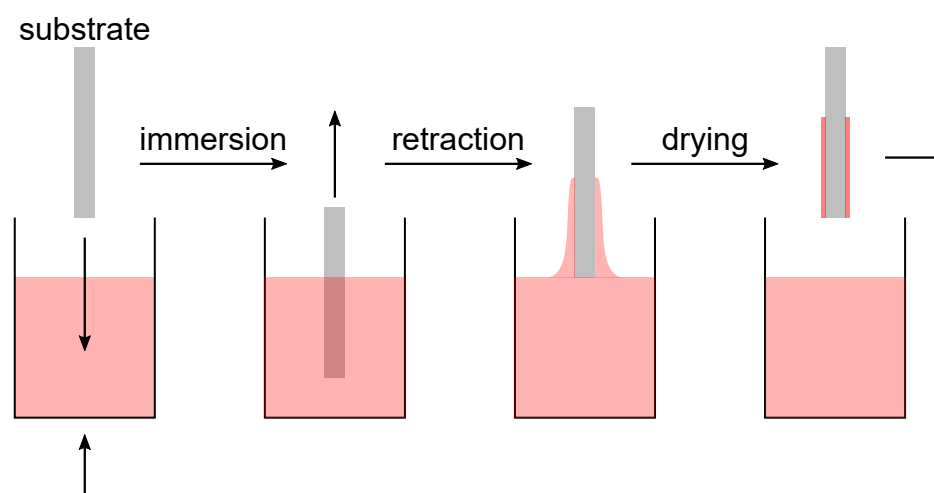


Figure 2.20: Schematic illustration of the dip coating process.

Spin coating: The typical preparation process of nanoparticle thin films via spin coating is presented in Figure 2.21. Initially, a solution containing preformed nanoparticles^[99] or molecular precursors^[100] is deposited on the target substrate, which is mounted on a rotatable plate. Thereafter, the substrate is rotated at a designated speed that results in a homogeneous coverage of the surface with the starting solution. Finally, the solvent is evaporated and the films may be further processed, e.g., through annealing steps^[101]. The film thickness is controlled by parameters such as the rotation speed, the concentrations, and the viscosity of the precursor solution. Repeating

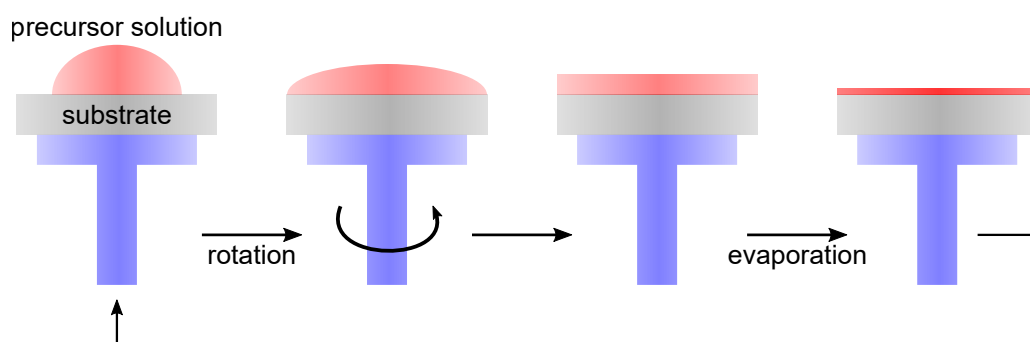


Figure 2.21: Schematic illustration of the spin coating process.

Theoretical background

the coating process is also typically mandatory to achieve thicker layers. Although the coatings are very homogeneous, the size of the substrate is limited. Additionally, a lot of material is wasted during the process since only a small fraction of the volume that is placed on the substrate eventually adheres to the surface^[102].

Screen printing: Screen printing is a useful method for the preparation of both continuous and structured thin films. The coating process is schematically displayed in Figure 2.22. Initially, the ink containing the nanoparticles is evenly spread on a mesh called a "screen". Upon bringing the mesh into contact with the substrate, the ink adheres to the surface of the substrate. When the mesh is retracted from the substrate, the ink will partially remain on the substrate^[103]. The properties of the deposited structures are influenced by the properties of the ink, such as viscosity and particle concentration, as well as the design of the mesh^[104].

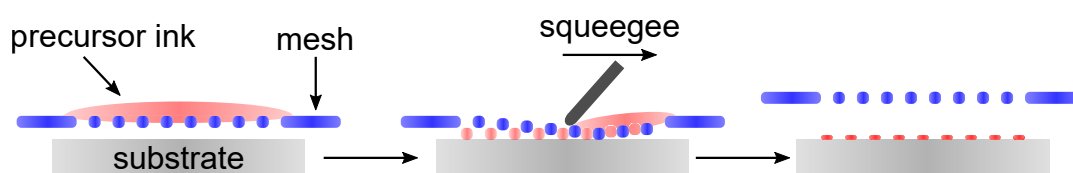


Figure 2.22: Schematic illustration of the screen printing process.

Doctor blading: Mesoporous nanoparticle thin films are frequently prepared with the doctor blade method^[105]. Here, a paste consisting of a solvent, the nanoparticles, and organic additives such as binders, plasticizers, or dispersants is evenly spread on the substrate by a blade (Figure 2.23)^[106]. The blade is operated at a distinct distance above the substrate, e.g., through a mask, and thus allows control over the final film thickness. After the blading step, the films are dried and then subjected to a calcination step to remove the organic residues to yield the porous structure and improve the stability of the nanoparticle network. The porosity can be tuned by varying the nanoparticle or binder concentrations.

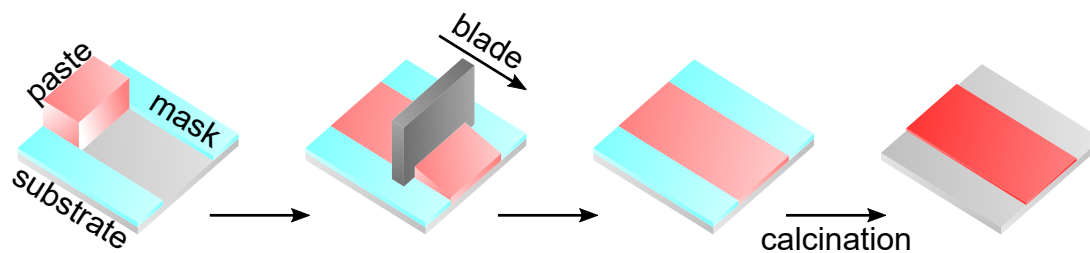


Figure 2.23: Schematic illustration of the doctor blading process.

2.2 Electrochromism

Some materials change their color when subjected to electric fields that induce redox reactions in the material by the injection or removal of electrons^[107]. This phenomenon is known as electrochromism. Based on the tunable modulation of the optical properties of electrochromic materials, they are exploited in optical applications such as smart windows^[108], displays^[109], mirrors^[110], and others. Typical electrochromic devices comprise several key components, as displayed in Figure 2.24. Each of these components will be briefly outlined below.

Conductive substrate and spacer: The outer frame of an electrochromic device consists of two substrates that are both coated with a conductive layer. The substrates and conductive layers that are used should exhibit high transparency in the desired spectral region. Since the conductive material is used for the connection to the external circuit, the resistance of this material is of crucial importance concerning the performance of the device. Glass plates with a thin layer of a transparent conductive oxide such as tin-doped indium oxide (ITO) or fluorine-doped tin oxide (FTO) are often utilized for this purpose^[111]. The growing interest in flexible devices consequently requires flexible substrates. For such cases, polyethylene terephthalate (PET) may be used as a supporting substrate and coated with conductive materials, e.g. ITO^[110] or graphene^[112]. Another typical component of an electrochromic device is a spacer material that accounts for a fixed distance between the two electrodes to prevent short

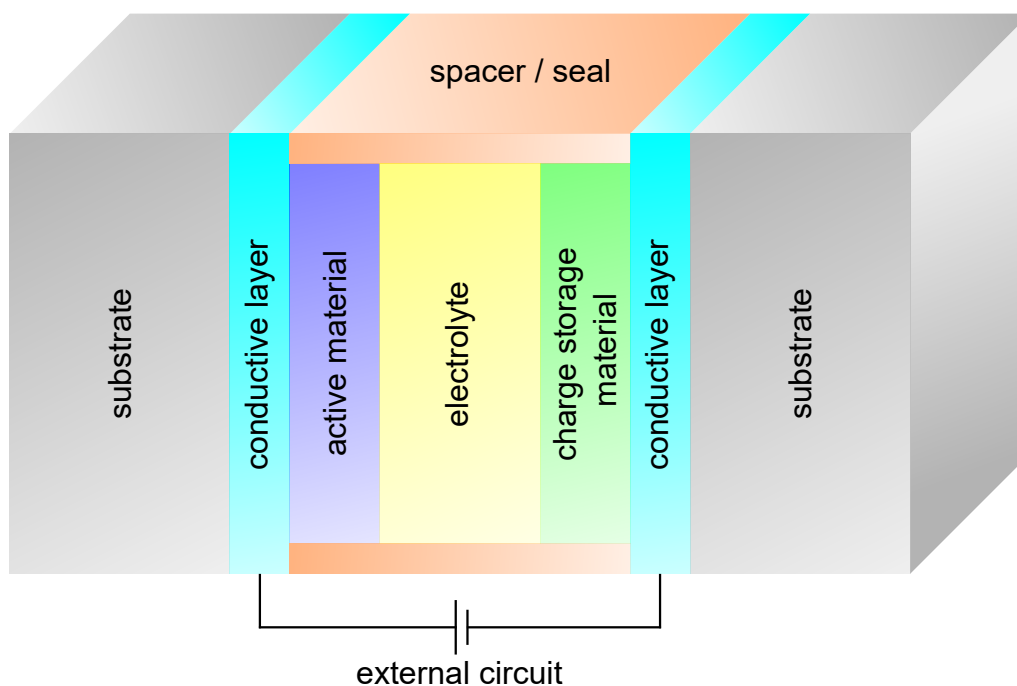


Figure 2.24: Schematic illustration of the typical setup of an electrochromic device.

Theoretical background

circuits and also acts as the seal to contain the electrolyte within the device, especially if the electrolyte is used in a liquid form.

Active material: The active material is the main component that is responsible for the change in the optical behavior of an electrochromic device. For instance, the material may change its color upon electrochemical reduction (cathodic coloration)^[113] or oxidation (anodic coloration)^[114]. A variety of materials are known to exhibit electrochromism and can be utilized in an electrochromic device, either in the form of thin films on the conductive substrate or as soluble species in the electrolyte. Nanoparticle films of transition metal oxides, e.g., tungsten oxide (WO_3), niobium oxide (Nb_2O_5), or titanium dioxide (TiO_2) are among the most studied electrochromic materials^[115]. These three oxides show cathodic coloration when electrons are injected into the nanocrystalline material accompanied by the intercalation of small cations, typically protons or lithium ions, to balance the charge. In the case of tungsten oxide, a typical electrochemical reaction leading to electrochromism can be expressed as follows:



Here M^+ represents the cations and e^- the electrons. When the electrons and cations are extracted by the application of a suitable potential, the nanoparticle film returns to its uncolored state. There are also a variety of organic compounds that display electrochromic behavior. In this regard, cathodically coloring viologens (substituted 4,4'-bipyridinium salts) are very popular since they have multiple redox states, as displayed in Figure 2.25^[116]. In their dicationic state, especially in monomeric form, viologens are typically highly transparent, while the radical cation typically has a large extinction coefficient that accounts for deep coloration. The neutral state is typically not as intensely

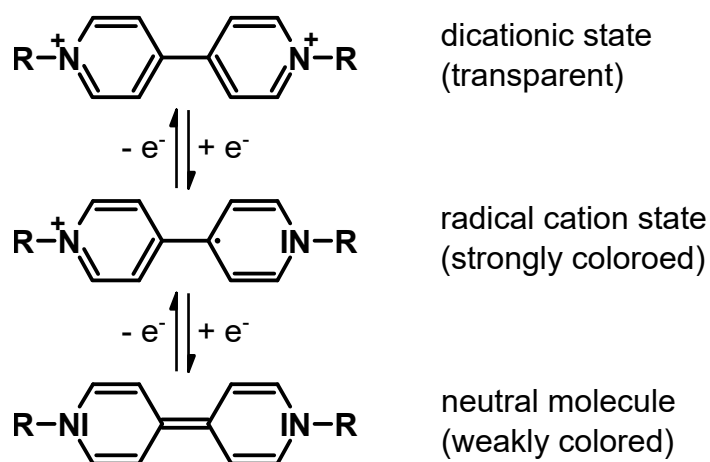


Figure 2.25: Schematic representation of the chemical structure of a viologen derivative undergoing multiple redox reactions.

Theoretical background

colored. Such organic compounds can be integrated into an electrochromic device in multiple ways. Monomeric species may be simply solubilized in the electrolyte, where they diffuse to the electrodes when electric fields are applied^[117]. Polymeric structures, on the other hand, are usually prepared as thin films on the substrate^[118].

Another approach is based on the chemical binding of monomeric species on the surface of the electrode. In this case, nanoparticle films are prepared on the substrate that provide a porous structure with a large inner surface area^[119]. Concerning the choice of nanoparticles, metal oxides, especially titanium dioxide, are typically used for this purpose^[120]. The organic molecules are equipped with an anchoring group that ensures stable binding of the molecules to the metal oxide surface. This situation is schematically shown in Figure 2.26 for a phosphonated viologen anchored to the surface of a nanoparticle layer. Anchoring molecules to a mesoporous scaffold may result in faster switching than solubilized species because electron transfer occurs at the metal oxide surface and thus diffusion processes are reduced. Additionally, the porous structure of the metal oxide films allows for the anchoring of a large number of molecules, which in return accounts for strong absorption in the colored state while the uncolored state remains highly transparent. This concept is utilized in the present thesis.

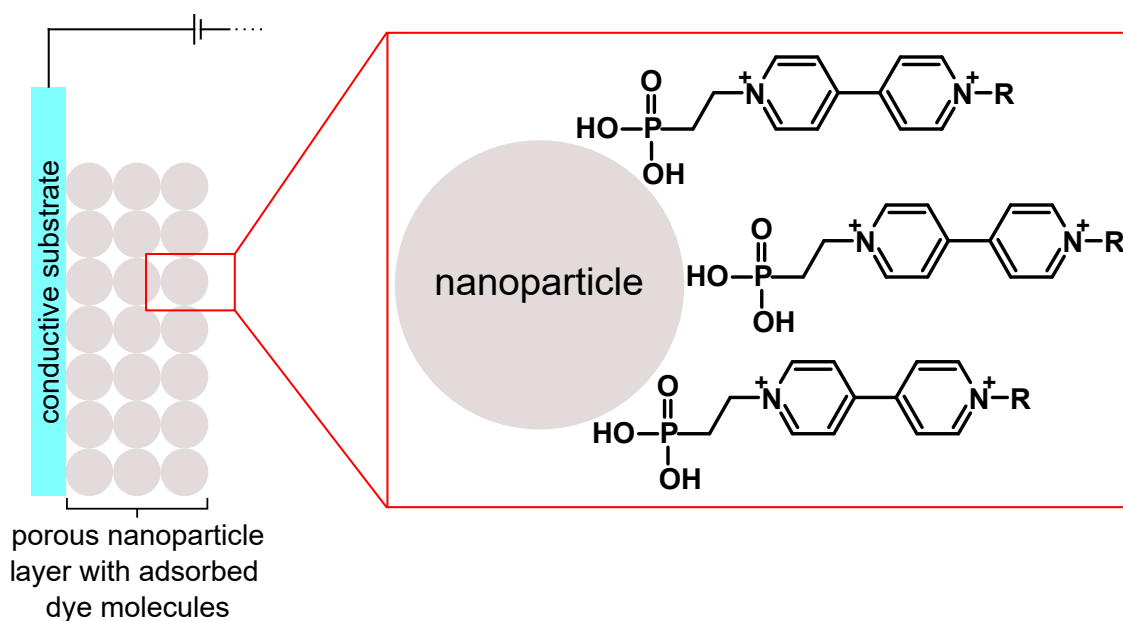
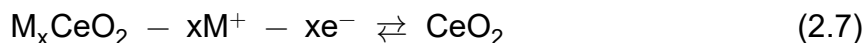


Figure 2.26: Schematic representation of a mesoporous nanoparticle layer on a conductive substrate with anchored viologen molecules on the surface of the nanoparticles.

Electrolyte: The flow of electrons between the two electrodes of an electrochromic device through the external circuit is accompanied by the movement of ions between the electrodes within the device. These ions, the electrolyte, are typically contained within a suitable medium that is filled into the electrochromic device and spatially located

between the electrodes. Especially in the case of active materials that rely on intercalation phenomena, the electrolyte is the source for the desired intercalating cations. Of course, the electrolyte should exhibit optically passive behavior. For research purposes, the electrolyte typically consists of a salt, e.g., lithium perchlorate (LiClO_4), which is solubilized in a high boiling point solvent such as propylene carbonate^[121]. In practical applications, however, the utilization of liquid electrolytes may be undesired due to safety concerns^[122]. Here, gel electrolytes^[119,123] or solid electrolytes^[124,125] are of greater interest. These electrolytes can also act as separators and seal the devices^[126].

Charge storage layer / counter electrode: The last component of an electrochromic device is a material that can undergo redox reactions that counteract the electron consumption/release of the active material. For instance, if the coloration is induced via the reduction of the active material, simultaneous oxidation on the other side of the device has to occur to provide the electrons that are required for the reduction process^[127]. This is crucial in order to achieve fast transitions between the colored and uncolored states of an electrochromic device. Several materials have been used for this purpose. For instance, mixed oxide thin films containing cerium oxide (CeO_2) are widely applied since the redox state of cerium can be switched between +3 and +4^[128]. The corresponding electrochemical reaction of CeO_2 , based on the (de)intercalation of suitable ions (M^+) and electron injection/exertion, can be written as:



CeO_2 offers optically passive behavior as it exhibits high transparency in the visible range in both the oxidized and reduced states. Another common inorganic material is nickel oxide (NiO) but in this case, oxidation of the material also results in coloration of the electrode^[129]. Of course, there are also a variety of organic compounds that can be used on the counter electrode^[130,131]. An example, which was actually used in this thesis, is a triphenylamine-based molecule that is anchored to porous films of antimony doped tin oxide (ATO) nanoparticles. In combination with a viologen as the active material, this molecule can be oxidized in a two-step process, as shown in Figure 2.27. The oxidized state of this molecule is also colored, while the reduced state is uncolored.

2.3 Aerogels

Aerogels are referred to as the products of a solvent exchange from a gel with a gaseous phase in which the initial solid network structure of the gel mostly remains intact^[132]. Due to their network-based structure, aerogels possess unique properties such as large

Theoretical background

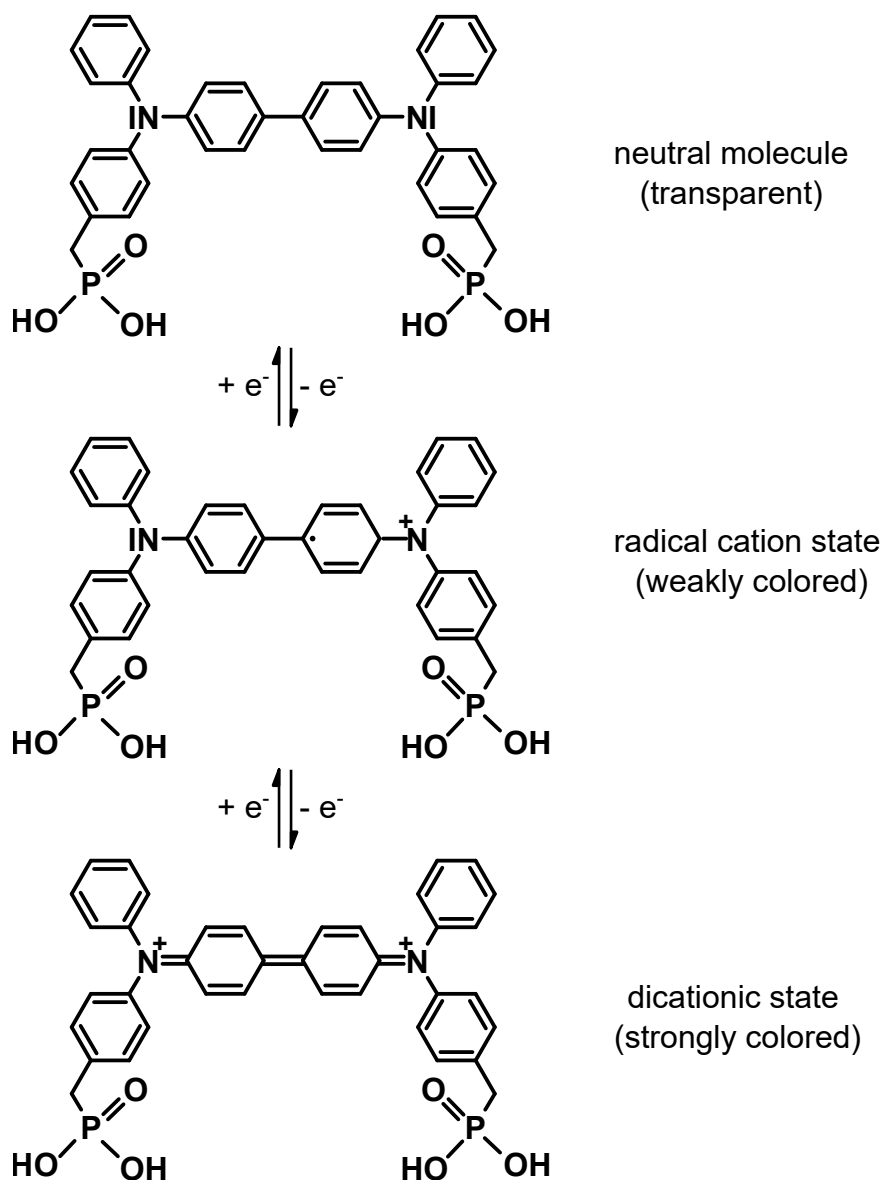


Figure 2.27: Schematic representation of the chemical structure of a triphenylamine-based derivate undergoing multiple redox reactions.

inner surface areas with multiple hundred square meters per gram as well as high porosities since the pores occupy the majority of the aerogel's macroscopic volume^[133]. Therefore, aerogels find application in a variety of fields such as photocatalysis^[134], thermal insulation^[135], energy storage^[136], or biomedical applications^[137]. In addition, the diversity of potential materials that can be assembled into aerogels spans a wide range of inorganic^[138], organic^[139], and hybrid materials^[140]. However, the preparation of aerogels typically follows a general scheme, of which the individual steps will be presented in the following sections.

2.3.1 Gelation

The first step in the preparation of aerogels involves the formation of a gel starting from a solution of suitable precursors of the desired material. Depending on the type of material, gelation may be initiated by a variety of mechanisms. For instance, polymer-based gels are accessible via the cross-linking reactions of molecular monomers^[141,142], or pre-formed polymers^[143,144]. One of the most researched types of organic gels prepared via cross-linking is based on resorcinol and formaldehyde, for which the schematic gelation through polycondensation is shown in Figure 2.28.

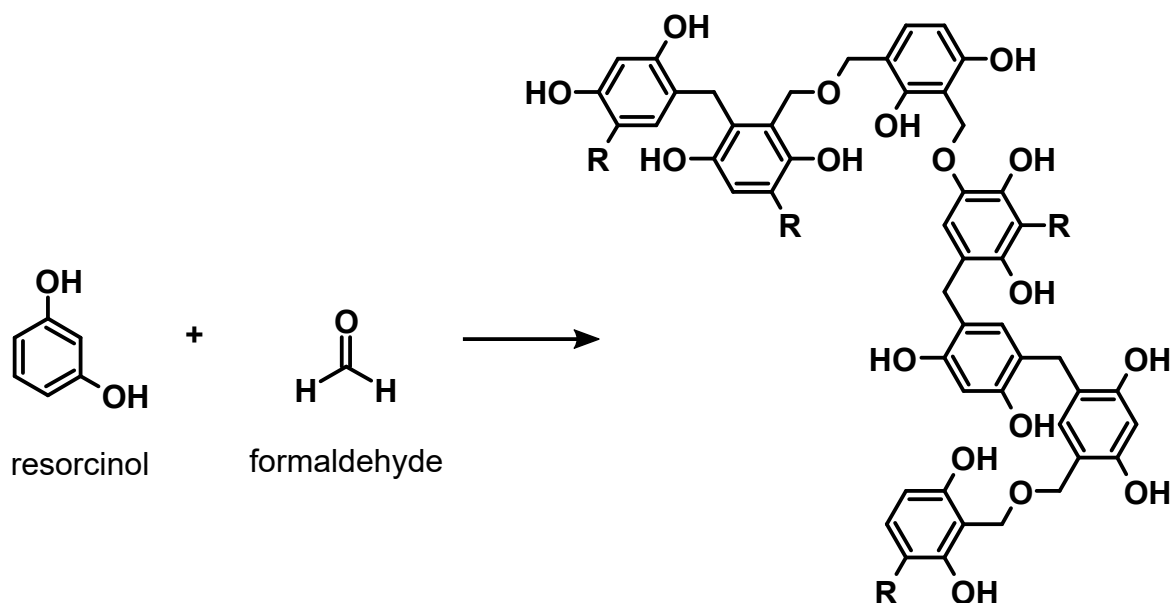


Figure 2.28: Schematic representation of the formation of a gel network through polycondensation reactions between resorcinol and formaldehyde.

In the case of inorganic aerogels, a sol-gel process is typically utilized to obtain the gels. Here, aerogels of silicon dioxide (SiO_2) are among the extensively studied compounds^[145]. A widely applied approach involves the hydrolysis and condensation of tetraalkoxysilanes. The individual steps of such a reaction are displayed in Figure 2.29. Initially, a solution of the tetraalkoxysilane in an alcohol is prepared. Following the addition of water and an acid or a base as a catalyst, the silane is partially hydrolyzed to yield reactive species that can undergo condensation reactions. These can occur between two hydrolyzed species under the elimination of water or between a hydrolyzed silane and an unreacted tetraalkoxysilane molecule that leads to the elimination of an alcohol. In either case, chains of oxygen-bridged silicon atoms are obtained that eventually interconnect to form the solid network as the reaction continues. Depending on the synthesis parameters, the structure of the obtained gels can be altered to achieve the desired properties, e.g., concerning the porosity^[146]. These parameters include the water-to-silane ratio, the catalyst, the pH value, and the reaction temperature^[147].

Theoretical background

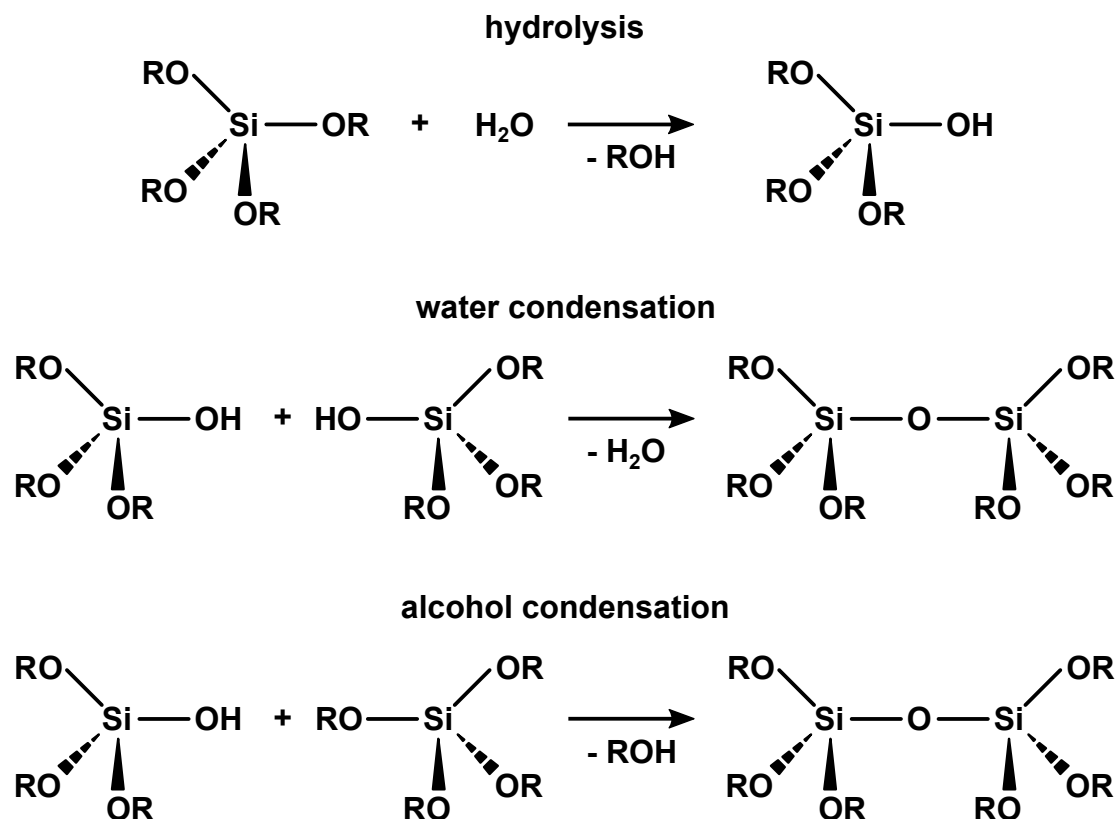


Figure 2.29: Schematic representation of the mechanism of hydrolysis and condensation of tetraalkoxysilanes.

Another approach that is very common in the preparation of aerogels based on metal oxides is the epoxide route^[148]. In this case, for example, a solution of a metal chloride is prepared in a polar solvent, to which an epoxide such as propylene oxide is added to initiate the gelation. The epoxide undergoes a ring-opening reaction, as shown in Figure 2.30 (other products are also obtained^[148]). This proton-consuming process results in an increase in pH value that leads to hydrolysis and condensation reactions of the metal species, which eventually yield the gel network^[149].

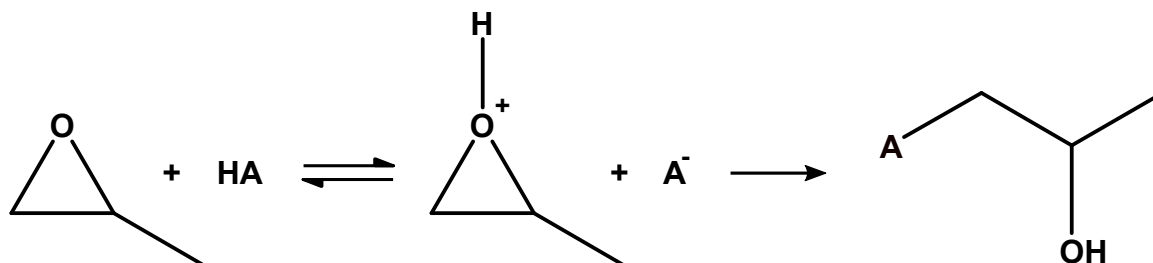


Figure 2.30: Schematic representation of the ring-opening reaction of propylene oxide.

Besides using molecular precursors to produce gels of inorganic nanoparticles, gelation may also be achieved starting from colloidal solutions of preformed nanoparticles^[150]. Here, initiation of the gelation depends on the nanoparticle stabilization mech-

anism, e.g., sterically or charge-driven. Typical procedures involve the removal of ligands through suitable additives for sterically stabilized colloids or a variation of the pH value in the case of charge-stabilized colloids^[151].

Regardless of the different gelation mechanisms, these procedures yield the desired gels that can be further processed to obtain the aerogels.

2.3.2 Aging and solvent exchange

Some types of gels benefit from an aging step prior to the solvent removal^[152]. In this step, the structure of the solid network is further strengthened by continuous reactions within the gel when kept in the starting solution. For instance, in the case of silica aerogel, dissolution and reprecipitation of monomers or additional hydrolysis and condensation steps onto the network account for an increase in the stability of the gels^[153]. Depending on the type of drying that is supposed to be used to obtain the aerogels, the solvent within the gels has to be exchanged^[154]. For example, supercritical drying usually requires the solvent in the gel to be miscible with the solvent that is used for drying, e.g., carbon dioxide (CO₂). Solvent exchange is usually performed by immersing the gel in the desired solvent. This can either be the pure new solvent or a mixture of the required solvent and the solvent that was used in the preparation process of the gel when the solvent exchange would otherwise lead to the destruction of the gel structure. To exchange all of the solvents within the gels, this process may require multiple days.

2.3.3 Drying

At last, the aerogels are obtained by removing all the solvent that is contained within the wet gels. Removing the solvent can be achieved by a variety of procedures, of which the three most common will be briefly discussed. The three-dimensional structure of the gels after solvent removal presents a highly desirable characteristic of aerogels, which can be preserved by supercritical drying^[155]. In this process, the solvent within the gels is initially exchanged for a suitable solvent that exhibits supercritical behavior under reasonable conditions. Typically, liquid CO₂ is used for this purpose. Then, the temperature and pressure are elevated above the critical point of CO₂ (Figure 2.31). At this stage, the pores are filled with the supercritical phase, which does not exert large capillary forces on the pore network when the supercritical phase is removed by lowering the pressure in the apparatus^[156]. With CO₂, reaching the supercritical phase is realized at comparably low temperatures (< 40 °C).

Solvent removal can also be achieved by means of freeze-drying. Here, in the first step, the solvent within the gels is frozen. Thereafter, the solidified liquid is removed by a sublimation step under reduced pressure to yield the solvent-free porous network^[157].

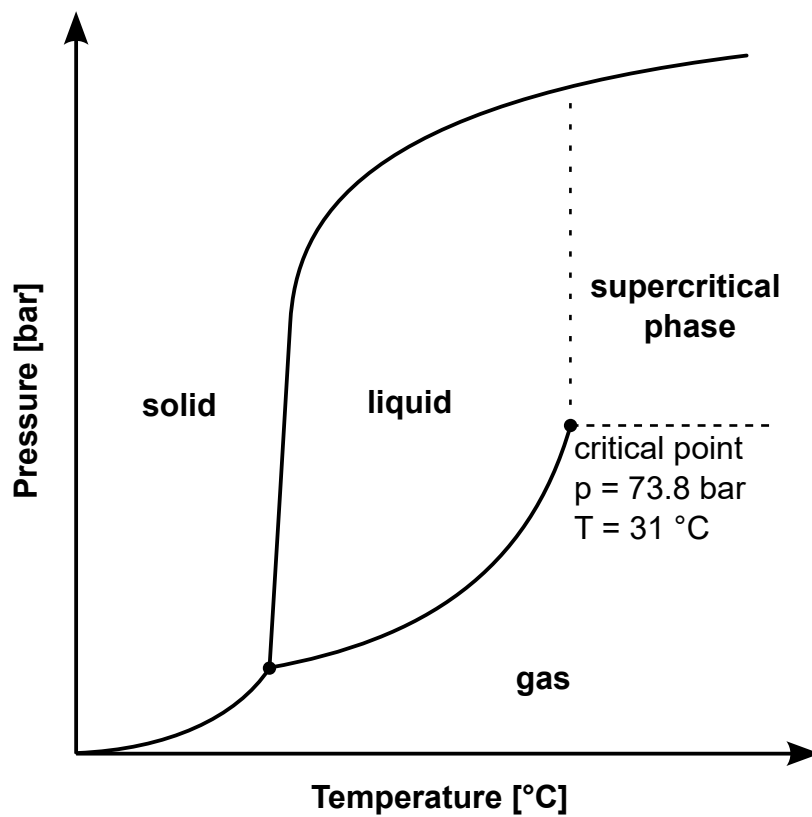


Figure 2.31: Schematic phase diagram of CO₂.

Especially with water as the solvent, freeze-drying is very common despite the increase in volume during freezing^[158]. This type of solid is referred to as cryogels^[159].

The simple evaporation of the solvent from a gel is termed ambient pressure drying. While this process is attractive in terms of safety and costs, the gels are prone to severe shrinkage and the formation of cracks due to high capillary forces^[160]. These obtained structures are called xerogels^[161].

3 Dispersible SnO₂:Sb and TiO₂ nanocrystals after calcination at high temperature

As previously discussed, antimony doped tin oxide (ATO) nanoparticles exhibit interesting properties. These are due to the integration of antimony ions, preferably in the +V oxidation state, into the tin(IV) dioxide lattice. Therefore, to balance the additional positive charge of the Sb⁵⁺ ions, an equal number of electrons must be present in the conduction band that changes the optical and electrical behavior of ATO compared to SnO₂. This makes ATO nanoparticles particularly interesting for electrochemical applications, as will be shown in the following chapters. First, however, a suitable synthesis procedure for ATO nanoparticles has to be established. Furthermore, it is desirable to be able to produce colloidal nanoparticle solutions, as these are convenient for further processing of the particles, in particular the fabrication of thin ATO layers. One problem that arises in the preparation of functional nanoparticles, as with ATO, is the fact that the desired properties are only accessible after treatment at high temperatures. However, this favors the formation of large, coalesced nanoparticle aggregates that cannot be re-dispersed into colloids. This chapter first covers the preparation of ATO nanoparticles and colloids of these. Further, a new methodology is presented that enables the re-dispersion of nanoparticles even after their calcination.

Parts of this chapter were published:

Jonas Klein, Michael Philippi, Fatih Alarслан, Tim Jähnichen, Dirk Enke, Martin Steinhart, and Markus Haase, "Dispersible SnO₂:Sb and TiO₂ Nanocrystals After Calcination at High Temperature", *Small* **2023**, 19, 2207674

3.1 Introduction

In the synthesis of many functional materials, high-temperature treatments can play a crucial role to improve the properties of a material after the initial preparation process. There are different aspects in which a high temperature can be beneficial or even required. For instance, the desired properties of a material may be unique to a specific crystallographic phase as it is the case with the α -phase of aluminum oxide ($\alpha\text{-Al}_2\text{O}_3$)^[162,163] or manganese sulfide (MnS)^[164]. Improving the crystallinity of a material and reducing defects is also of considerable importance to enhance properties such as photocatalytic activity. Common materials displaying such behavior include titanium dioxide (TiO_2)^[165], tin dioxide (SnO_2)^[166], or zinc oxide (ZnO)^[167,168]. Another class of interesting materials frequently requiring the use of high temperatures in the synthesis are doped crystals. Here, high-temperature treatments may facilitate the integration of dopant ions into the host lattice. In the case of luminescent materials, this is accompanied by a narrowing of the linewidth of emission peaks^[169,170].

Separated particles can be prepared via synthesis methods involving solvents as reaction medium and suitable additives that account for sterically or electrostatic repulsion between the particles^[171–173]. These procedures however are limited with respect to the reaction temperature by the boiling point of the solvent. Therefore, additional calcination steps at higher temperatures are usually required after the initial synthesis of the material to achieve their favored properties. An undesirable consequence of such calcination treatments involves the sintering of individual particles into fused aggregates^[174–176]. This usually negatively affects the redispersion of the particles. Especially in the case of nanoparticles, obtaining stable colloidal nanoparticle solutions can be greatly desirable for investigation of their properties or further processing, e.g., preparation of thin films. To solve this problem, the contact between nanoparticles during calcination has to be minimized to a degree, which prevents the formation of large aggregates. Common approaches presented in earlier works utilize a sacrificial material (e.g., SiO_2) that protects the particles during calcination, e.g., through a shell around the nanoparticles^[177–180]. After the calcination step, the SiO_2 is removed from the particles, for instance by chemical etching. These procedures finally allow for the preparation of colloidal solutions of the particles^[181,182].

However, in the work presented here, a completely different approach based on nanoparticle aerogels is used. Aerogels composed of nanoparticles have gained considerable interest in recent years, because their highly porous structure allows easy access to the surface of the particles, while the comparatively small number of interconnections between the nanoparticles only weakly affects their properties in many cases^[183,184]. Therefore, there are a large number of studies reporting on the optical^[185], magnetic^[186], energy storage^[129], and catalytic^[187] properties of nanoparticle

aerogels. Herein, the porous structure is also utilized, but in a very different way: It is shown that nanoparticles, in the form of an aerogel, can be treated at much higher temperatures than even high-boiling solvents allow in the synthesis of the particles and that the aerogels can still be converted back into stable colloidal solutions with only weak agglomeration of the particles. The aerogel route is demonstrated with antimony doped tin oxide (ATO) and TiO_2 nanoparticles. Especially the properties of ATO, namely the plasmon absorption in the IR region due to the doping with antimony, benefit from high-temperature treatment^[188]. This is also immediately apparent from the appearance (blue coloration) of the colloids from nanoparticles treated at different temperatures.

3.2 Experimental

Synthesis of Antimony Doped Tin Dioxide Nanoparticles (10% Sb):

First, 66 mmol of potassium hydroxide (3.703 g, Sigma Aldrich) and 2 mL of hydrogen peroxide (30 wt.%, Merck) were dissolved in 250 mL of water. Next, 6.6 mmol of potassium hexahydroxoantimonate (1.735 g, Merck) was added and the suspension was heated at 90 °C until a clear solution was obtained. After cooling to room temperature, 59.4 mmol of potassium hexahydroxostannate (17.758 g, Sigma Aldrich) was dissolved, yielding a clear solution. Precipitation was induced by adding 198 mmol of hydrobromic acid (22.23 mL of 48 wt.% HBr diluted to 100 mL). The resulting suspension was then heated to 95 °C. After 30 min at 95 °C, a 1 M solution of potassium hydroxide was added dropwise until a clear colloidal solution was obtained which was further heated for an additional 30 min. Thereafter, the solution was cooled to room temperature and the nanoparticles were again precipitated by the addition of hydrobromic acid, centrifuged, and washed several times with water until the supernatant remained slightly turbid. For the autoclave treatment, the nanoparticles were redispersed in 200 mL water containing 2 mL of 1,8-diazabicyclo[5.4.0]undec-7-en (in the following abbreviated as DBU, purchased from TCI). The transparent colloidal solution resulting after stirring for 30 min was purged with nitrogen for a further 20 min and then heated at 200 °C for 5 h in a Teflon-lined autoclave. Finally, the nanoparticles were precipitated again by the addition of hydrobromic acid and repeatedly washed with water.

Synthesis of Titanium Dioxide Nanoparticles:

For the synthesis of TiO_2 nanoparticles, 25 mmol of titanium isopropoxide (7.40 mL, Sigma Aldrich) was combined with 50 mmol of DBU (7.46 mL) and the mixture was stirred for 20 min. Subsequently, 10 mL of methanol and 150 mL of water were added under stirring. The nanoparticles were then precipitated via the addition of 50 mmol of hydrobromic acid (5.60 mL of 48 wt.% HBr diluted to 50 mL). After heating the resulting

Experimental

suspension at 95 °C for 1 h, the nanocrystalline precipitate was separated by centrifugation and washed three times with water.

Preparation of Aerogels:

At first, colloidal solutions were prepared by stirring 0.5 g nanoparticles in 10 mL of a 1:3 mixture of water and ethanol containing 0.1 mL of DBU. In the case of ATO, the nanoparticles were used that were heated in the autoclave. After the addition of 0.2 mL ethyl formate (Alfa Aesar), the solution was transferred into a cylindrical mold (plastic syringe) with a diameter of 19 mm. The solution in the mold was then placed in an oven (60 °C) until gelation occurred (approx. 20 min). Thereafter, the gel was removed from the mold and immersed in pure ethanol. Over 2 days, the solvent was frequently replaced to exchange the solvent within the gel against pure ethanol. At last, the ethanol-containing gel was converted into an aerogel by supercritical drying with CO₂ in a Leica EM CPD300 critical point dryer. Calcination of the aerogels was performed in an electric oven at 500 °C for 2 h.

Preparation of Colloidal Nanoparticle Solutions with Different Solvents:

1) Water: Aqueous colloids of ATO or TiO₂ nanoparticles were used as starting material to transfer the particles into other solvents. The aqueous colloids were prepared by stirring 0.1 g nanoparticles (ATO or TiO₂) with 10 µL DBU and 1 mL of water until all solid was dispersed. 2) Methanol: First, the nanoparticles were precipitated from the aqueous colloidal solution (0.1 g mL⁻¹) by adding the fivefold volume of acetone. After separating the precipitate by centrifugation, the nanoparticles were redispersed in methanol, again precipitated with acetone, and collected by centrifugation. The precipitate thus obtained could be redispersed in methanol to obtain colloidal solutions of the particles in this solvent. 3) Toluene/tetrachloroethylene: To transfer the particles into nonpolar solvents, the nanoparticles were precipitated from the methanolic colloid by adding a solution of 10 wt.% of dodecylamine (Sigma Aldrich) in methanol. After separating the precipitate by centrifugation, the precipitate was heated in pure dodecylamine at 95 °C for 1 h, resulting in a clear colloidal solution of the nanoparticles at this temperature. Finally, the particles were collected and purified by applying three cycles of precipitation with methanol, centrifugation, and redispersion in toluene. The dodecylamine-capped nanoparticles thus obtained can be redispersed in a variety of nonpolar solvents. In the present work, toluene and tetrachloroethylene (Sigma Aldrich) were used.

Characterization of the Materials:

A Zeiss Auriga scanning electron microscope (SEM), operated with an acceleration

voltage of 3 kV, was used to record SEM images. The solid samples were sputtered with platinum/iridium before the measurements. X-ray powder diffraction (XRD) data were measured with a Panalytical Empyrean diffractometer in Bragg–Brentano geometry using Cu K- α radiation. The diffractograms were recorded with a step size of 0.026° (for 2θ). X-ray fluorescence measurements were carried out with a Panalytical Axios instrument. Transmission electron microscopy (TEM) images were recorded with a JEOL JEM-2100 Plus microscope. The instrument was equipped with a LaB_6 cathode, an EM-24830FLASH camera (JEOL), and operated at 200 kV. Optical absorbance spectra were recorded on a Carry 6000i UV-VIS-NIR spectrometer and a Bruker Vertex 70 FT-IR spectrometer. Measurements were performed with a CaF_2 cuvette with a path length of 0.5 mm. The nanoparticles were dispersed in tetrachloroethylene with a concentration of 10 mg mL^{-1} . Nitrogen sorption measurements on nanoparticle aerogels and powders were performed with a Quantachrome Autosorb at 77 K. The total pore volume was calculated at $p/p_0 = 0.995$, while the specific surface area was calculated using the BET method in a relative pressure range of $p/p_0 = 0.05\text{--}0.30$. A Malvern Zetasizer Nano ZSP was used to obtain dynamic light scattering (DLS) measurements of colloidal nanoparticles dispersed in either water, methanol, or toluene.

3.3 Results and discussion

Figure 3.1 displays the individual steps to prepare colloidal solutions of calcined ATO nanoparticles. Initially, ATO nanoparticles were prepared via coprecipitation from an aqueous precursor solution containing hexahydroxostannate and hexahydroxoantimonate (Figure 3.2) by the addition of hydrobromic acid followed by heating at 95°C . An antimony-dopant concentration of 10% was chosen and experimentally confirmed by X-ray fluorescence measurements (10.4%). Powder X-ray diffraction (XRD) measurements (Figure 3.3a) of the nanocrystalline material obtained after heating at 95°C show no other phases than cassiterite, i.e., the tetragonal structure of rutile-type tin dioxide. The Scherrer equation yields a nanoparticle size of approx. 2 nm for the particles in accord with the very broad peaks. Since the XRD data do not show peaks corresponding to phases of antimony compounds, even after calcination at 500°C , it is reasonable to conclude that the antimony was successfully incorporated into the crystal lattice of tin dioxide during coprecipitation. The nanoparticles obtained after heating at 95°C form a colorless powder (Figure 3.1a). This is also apparent from absorbance measurements of the particles in the UV to IR range. For these measurements, colloidal solutions were prepared by redispersing the nanoparticles in tetrachloroethylene as solvent and dodecylamine as surface ligand. For the particles prepared at 95°C , almost no absorption is observed over the whole frequency region (Figure 3.3b). Notably, the distinct peaks

Results and discussion

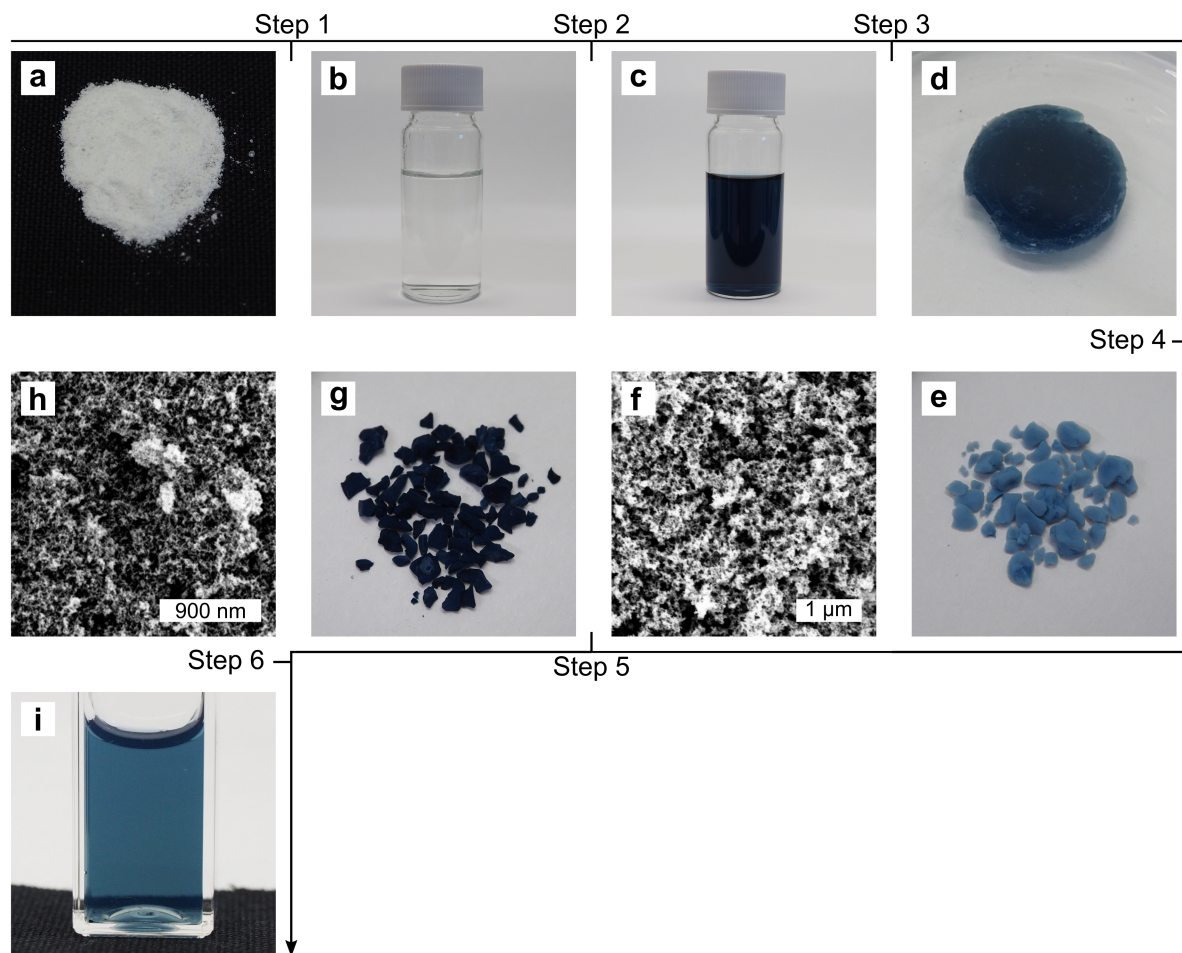


Figure 3.1: Photographs of: a) ATO nanoparticles synthesized at 95 °C; aqueous colloidal solution of ATO nanoparticles b) before and c) after autoclave treatment; d) nanoparticle gel; e) nanoparticle aerogel; f) SEM image of ATO aerogel; g) nanoparticle aerogel after calcination at 500 °C; h) SEM image of ATO aerogel after calcination; i) aqueous colloidal solution of calcined ATO nanoparticles.

between approx. 3700 and 2700 cm^{-1} , which are present in all samples, can be assigned to the ligand (dodecylamine) as well as residual methanol, resulting from the ligand exchange process to obtain colloidal solutions in tetrachloroethylene. Since the absorption spectrum lacks the characteristic plasmon absorption band of n-conductive oxides at this stage, the excess charge of the Sb^{5+} ions is not compensated by free electrons in the conduction band. Instead, charge compensation is most likely provided by additional O^{2-} or OH^- ions in the crystal lattice. The synthesis product of the coprecipitation may then be written as a mixed oxide $\text{Sn}_{1-y}\text{Sb}_y\text{O}_{2+0.5y}$ or mixed oxide/hydroxide $\text{Sn}_{1-y}\text{Sb}_y\text{O}_{2+0.5y-z}(\text{OH})_{2z}$ (sometimes written as a hydrated oxide $\text{Sn}_{1-y}\text{Sb}_y\text{O}_{2+0.5y}\cdot z\text{H}_2\text{O}$). Charge compensation would not be required if the crystal lattice contained an equal number of Sb^{3+} and Sb^{5+} ions. The presence of antimony ions in both valence states, however, results in a yellowish to brownish coloration of the nanoparticles, as verified by EXAFS/XANES and photoelectron spectroscopy^[189,190]. Since the synthesis starts

Results and discussion

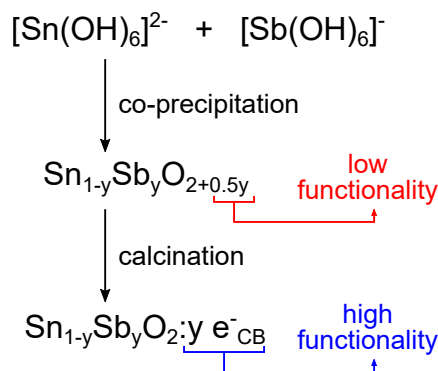


Figure 3.2: Chemical formulas representing the preparation of functional ATO nanoparticles by coprecipitation and subsequent calcination.

with an antimony(V) compound and a purely white powder is obtained, the number of Sb^{3+} ions in the SnO_2 lattice can only be small^[189]. In principle, charge compensation could also be provided by Sn vacancies. However, already in the starting compound hexahydroxostannate, the tin atoms are coordinated octahedrally by six oxygen atoms, as is the case in tin dioxide. For this reason, six tin-oxygen bonds would have to be broken to create a Sn vacancy, which seems not very likely given the low synthesis temperature. In fact, earlier work has shown that the plasmon absorption band already forms when the aqueous colloid is heated at 270 °C in a reducing atmosphere (autoclave, forming gas)^[191]. The observation that reducing conditions are favorable also suggests that oxygen species have to be removed from the nanoparticles to obtain n-conductive $\text{Sn}_{1-y}\text{Sb}_y\text{O}_2$ (Figure 3.2).

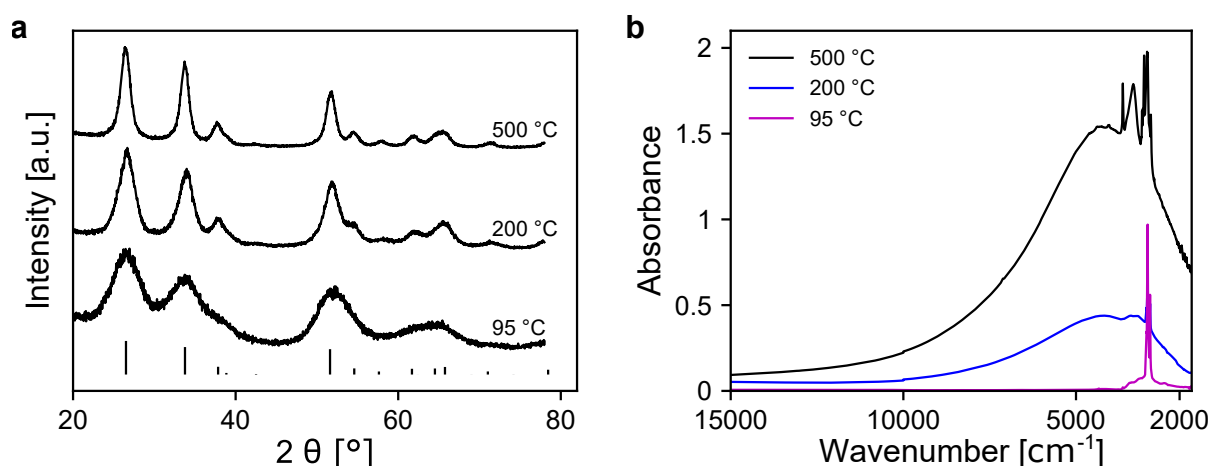


Figure 3.3: a) XRD patterns of ATO nanoparticles treated at 95, 200, and 500 °C along with a reference spectrum of tetragonal SnO_2 (ICSD: 39177). b) Absorbance spectra of colloidal solutions of ATO nanoparticles treated at 95, 200, and 500 °C with tetrachloroethylene as the solvent and a nanoparticle concentration of 10 mg mL^{-1} .

The first step in the preparation of the aerogels involves the redispersion of the nanoparticles into a clear colloidal solution in water (Figure 3.1b). This is achieved by

Results and discussion

the addition of a strong base (1,8-diazabicyclo[5.4.0]undec-7-en, DBU) that accounts for electrostatic repulsion between individual nanoparticles. After treatment of the solution in an autoclave at 200 °C, a blue colloid is obtained (Figure 3.1c). The XRD data of these particles (Figure 3.3a) exhibit narrower peaks as the temperature treatment increased the mean particle size to approx. 3 nm. The blue color of the colloidal solution is caused by a plasmon absorption band in the near IR region that extends into the visual spectrum (Figure 3.3b). The formation of the plasmon absorption band confirms the presence of free electrons in the conduction band of the ATO nanoparticles after the autoclave treatment. The next step in the preparation of the aerogels involves gelation of the colloidal nanoparticle solution. For this purpose, an ester (ethyl formate) is added to an alkaline colloidal solution containing 50 mg mL⁻¹ nanoparticles in an ethanol/water solvent mixture. By increasing the temperature to 60 °C, the ester is homogeneously hydrolyzed in the solution, causing a homogeneous decrease in pH. The decreasing pH weakens the electrostatic nanoparticle stabilization, finally resulting in the formation of a gel (Figure 3.1d). After a solvent exchange within the gels to pure ethanol, the aerogels are obtained via supercritical drying with CO₂ (Figure 3.1e). Characterization of the aerogels by scanning electron microscopy (SEM) confirms that the nanoparticles formed a highly porous network (Figure 3.1f). The aerogels were then placed in an electric oven and calcined at 500 °C. An SEM image of a calcined aerogel is presented in Figure 3.1h, which shows that the nanoparticle network remains intact during calcination and prevents the nanoparticles from forming large aggregates. Figure 3.3a shows that the calcination leads only to a slight narrowing of the XRD peaks indicating an increase of the particle size to approx. 5 nm. It is also apparent from Figure 3.1g that the high-temperature treatment resulted in an intensification of the blue coloration. After calcination of the aerogel, the fully functional ATO nanoparticles can again be redispersed in the form of clear colloidal solutions, as will be described in more detail below. With water as the solvent, this is achieved by the addition of a strong base (Figure 3.1i). The corresponding colloidal solution in tetrachloroethylene (Figure 3.3b) displays a plasmon absorption band that is increased in intensity by a factor of three compared with a solution of particles treated at 200 °C. Thus, the calcination at 500 °C further increases the number of free electrons in the conduction band and, hence, the conversion to n-doped SnO₂:Sb. Notably, for the preparation of aerogels, the autoclave treatment of the colloidal solutions at 200 °C is not strictly necessary but is nevertheless displayed here to highlight the difference in coloration of the aerogels before and after calcination at 500 °C. From the results presented so far, it is obvious that nanoparticles such as ATO require high-temperature treatments to gain their full functionality, in this case, high n-conductivity. In a control experiment, the ATO nanoparticles were simply calcined as a powder without first forming an aerogel. These particles cannot be re-

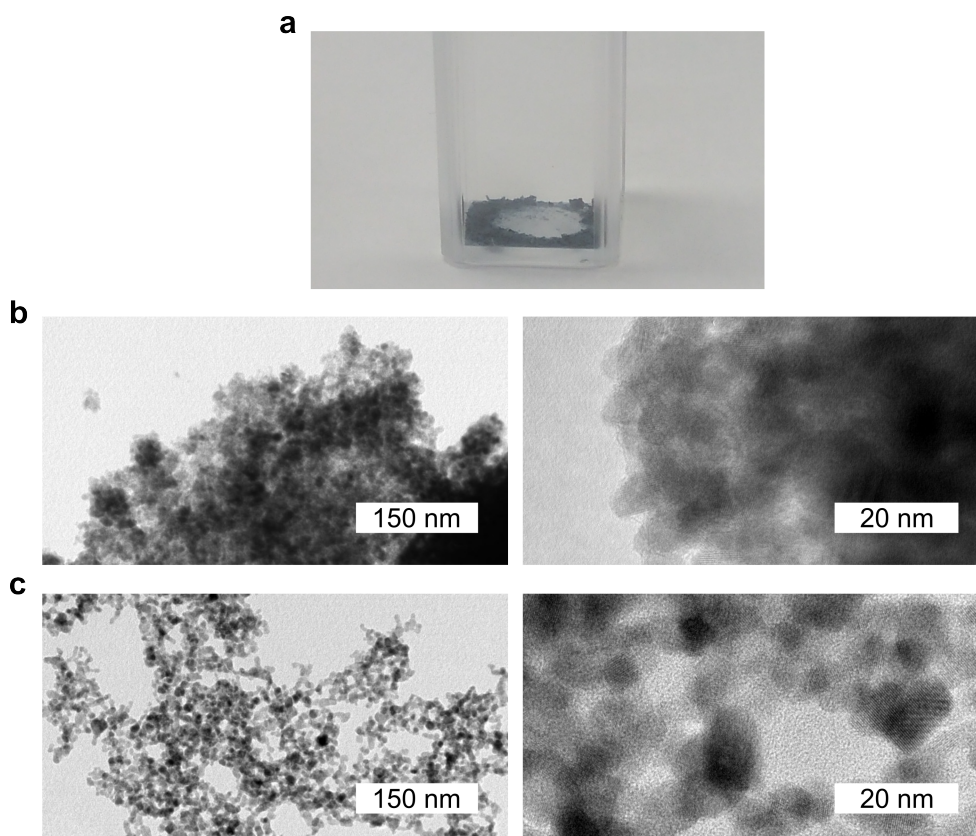


Figure 3.4: a) Photograph of a failed attempt to obtain an aqueous colloidal solution (using DBU as base) of calcined ATO nanoparticles without the formation of an aerogel. The particles were precipitated from the solution and the powder calcined at 500 °C. b) TEM images of ATO particles that were calcined as powder. c) TEM images of ATO particles that were calcined as aerogel.

dispersed in a water/DBU mixture, as shown in Figure 3.4a. Since rapid sedimentation occurs, dynamic light scattering (DLS) measurements, for example, are not possible. This is due to the formation of large aggregates during the calcination process, which can be seen in transmission electron microscopy (TEM) images (Figure 3.4b). On the other hand, TEM images of the particles calcined as aerogels display highly limited aggregation (Figure 3.4c) that allows redispersion of the particles into stable colloidal solutions. Further insight into this phenomenon was gained through nitrogen sorption experiments (Figure 3.5 and Table 3.1). These measurements show that the nanoparticle aerogels contain considerably larger pores compared with the nanoparticle powder. The high-temperature treatment of the aerogels results in a decrease in specific surface area and pore volume, which is a typical sign of the formation of fused aggregates. To study the degree of agglomeration in solution, colloidal solutions of ATO nanoparticles in different solvents and after different heat treatments were analyzed by DLS and TEM. As mentioned above, aqueous colloids can be prepared by the addition of a

Results and discussion

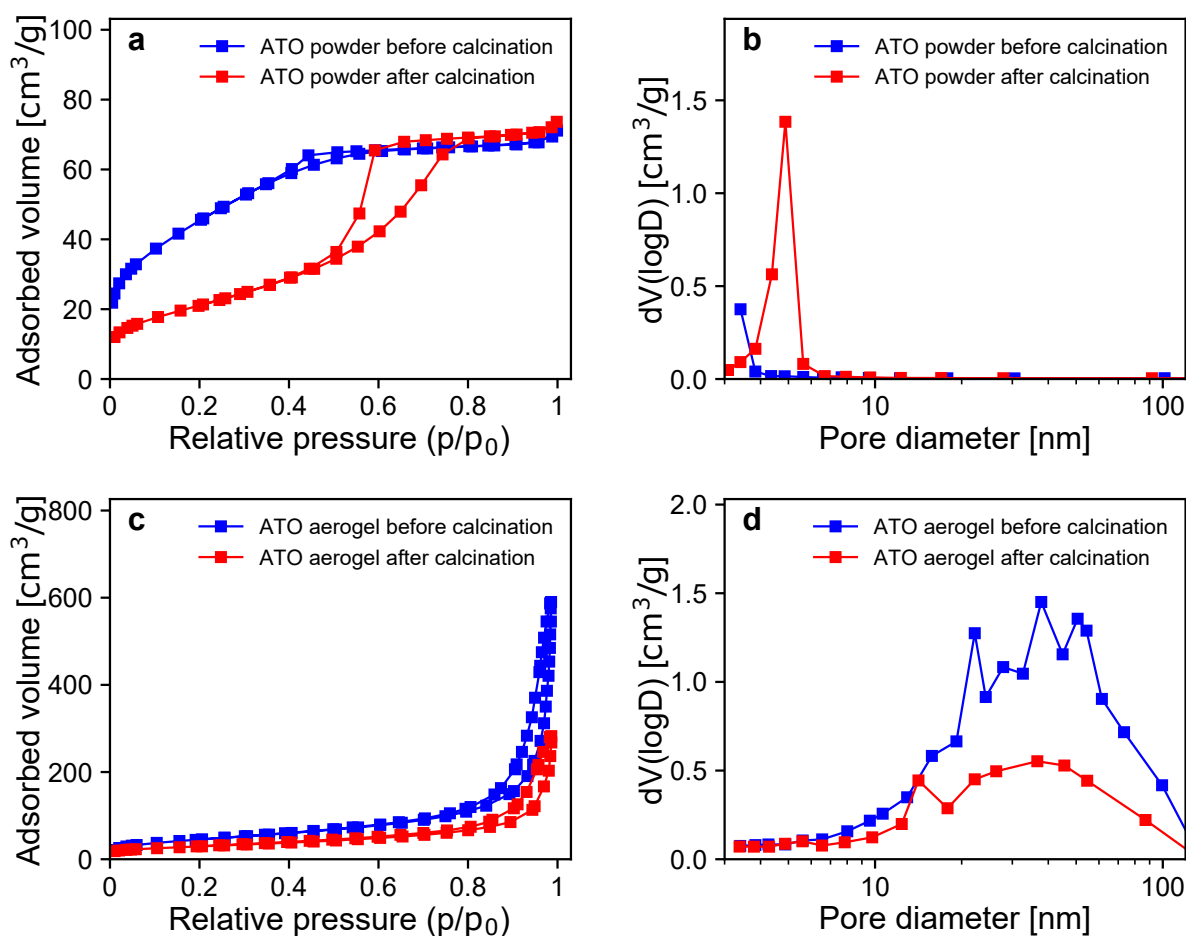


Figure 3.5: Nitrogen sorption isotherm of ATO particles in the form of a) a powder and c) assembled as aerogel before and after calcination. BJH pore volume $dV(\log D)$ against pore diameter of ATO particles in the form of b) a powder and d) assembled as aerogel before and after calcination. The measurements were performed by Tim Jähnichen in the group of Dirk Enke at Universität Leipzig.

Table 3.1: BET-surface area and total pore volume of ATO powders and aerogels before and after calcination, obtained from the nitrogen sorption measurements displayed in Figure 3.5.

Particles	BET-surface area [m ² g ⁻¹]	Total pore volume [cm ³ g ⁻¹]
ATO powder before calcination	155	0.11
ATO powder after calcination	77	0.11
ATO aerogel before calcination	167	0.30
ATO aerogel after calcination	105	0.19

a strong base to a slurry of nanoparticles in water. The corresponding DLS measurements are shown in Figure 3.6a displaying particles synthesized at 95 °C, particles that

Results and discussion

were heated in the autoclave at 200 °C, and particles that were calcined at 500 °C in the form of an aerogel. The DLS data show hydrodynamic diameters of approx. 4 and 7.5 nm after heating at 95 and 200 °C, respectively, and therefore only slight agglomeration when compared with the sizes obtained by XRD. From the TEM images displayed in Figure 3.6d/e, the average size of individual particles can be determined as 2.7 nm (95 °C) and 4 nm (200 °C). Furthermore, these particles display a rather uniform spherical shape. After calcining the aerogels at 500 °C, the mean hydrodynamic particle diameter increased to about 24 nm. This is not surprising since the nanoparticles were in contact with each other during the calcination process. Some degree of sintering between individual nanoparticles, therefore, is inevitable and in accord with the nitrogen sorption measurements mentioned above. This is also evident from TEM images of the calcined particles as shown in Figure 3.6f. In this case, it can be observed that individual particles are fused together to form aggregates with continuous lattice fringes as a result of the calcination procedure. However, it is remarkable that the size of the fused aggregates is below 30 nm and small enough to allow complete redisper-

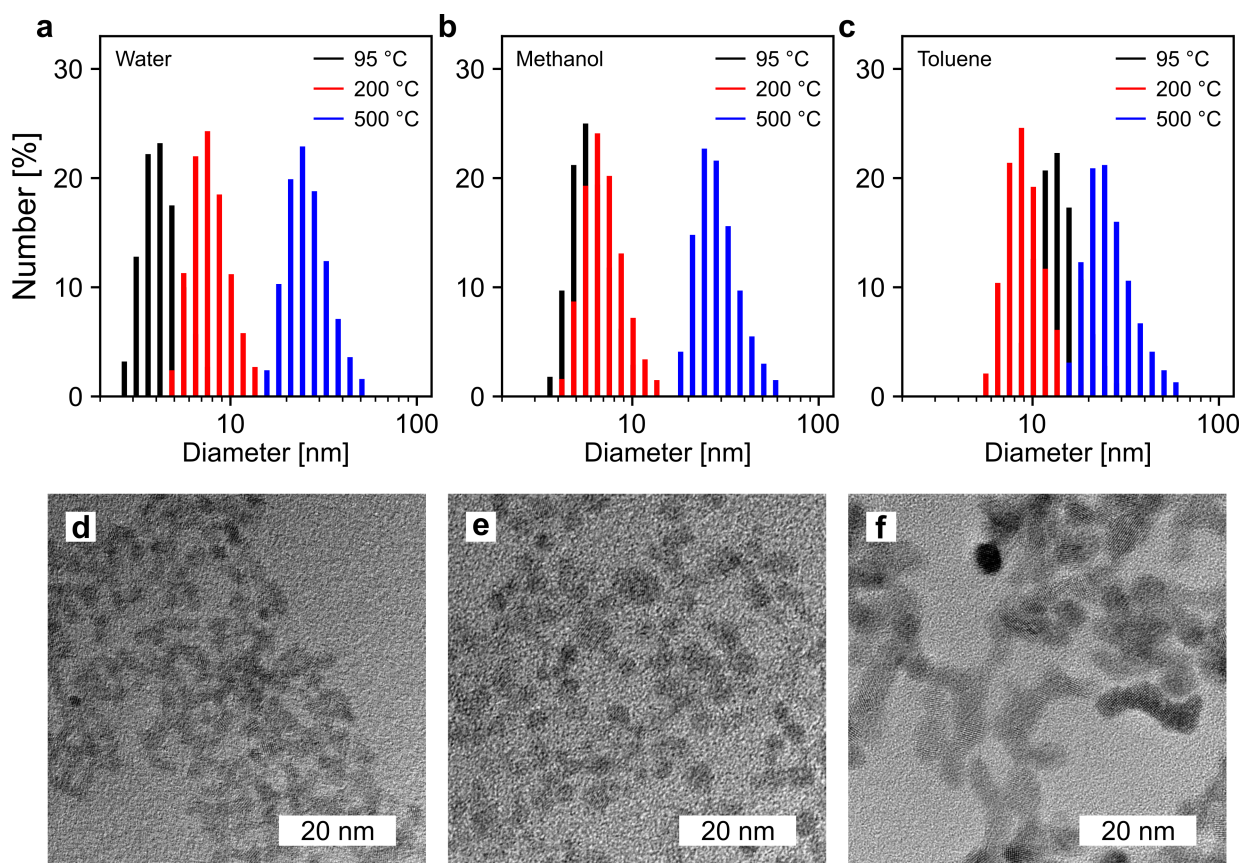


Figure 3.6: DLS measurements of colloidal solutions of ATO nanoparticles treated at temperatures of 95, 200, and 500 °C, using: a) water, b) methanol, and c) toluene as solvent, respectively. TEM images of ATO nanoparticles treated at a temperature of: d) 95 °C, e) 200 °C, and f) 500 °C.

Results and discussion

sion of the nanoparticles after calcination into clear colloidal solutions, especially since no sacrificial material is needed that separates the particles during calcination. As these particles are not uniform in shape, their size was not further evaluated as it was done for the particles treated at 95 and 200 °C. After precipitation from aqueous solution, the nanoparticles can also be redispersed in methanol as shown in Figure 3.6b. The figure shows that the overall trend of the DLS measurements is comparable to the aqueous colloids, as average diameters of 5.5 nm (95 °C), 6.5 nm (200 °C), and 26 nm (500 °C) are observed. Finally, the nanoparticles can be redispersed in nonpolar solvents. In this case, the nanoparticles are first precipitated from the methanolic colloidal solution by adding an apolar ligand such as dodecylamine and then redispersed in excess ligand as solvent. After precipitation with methanol, the particles can be redispersed in apolar solvents such as the aforementioned tetrachloroethylene, toluene, and others. DLS measurements of colloids with toluene as solvent are displayed in Figure 3.6c. The average diameters of the nanoparticles treated at 200 °C (8 nm) and 500 °C (24 nm) are

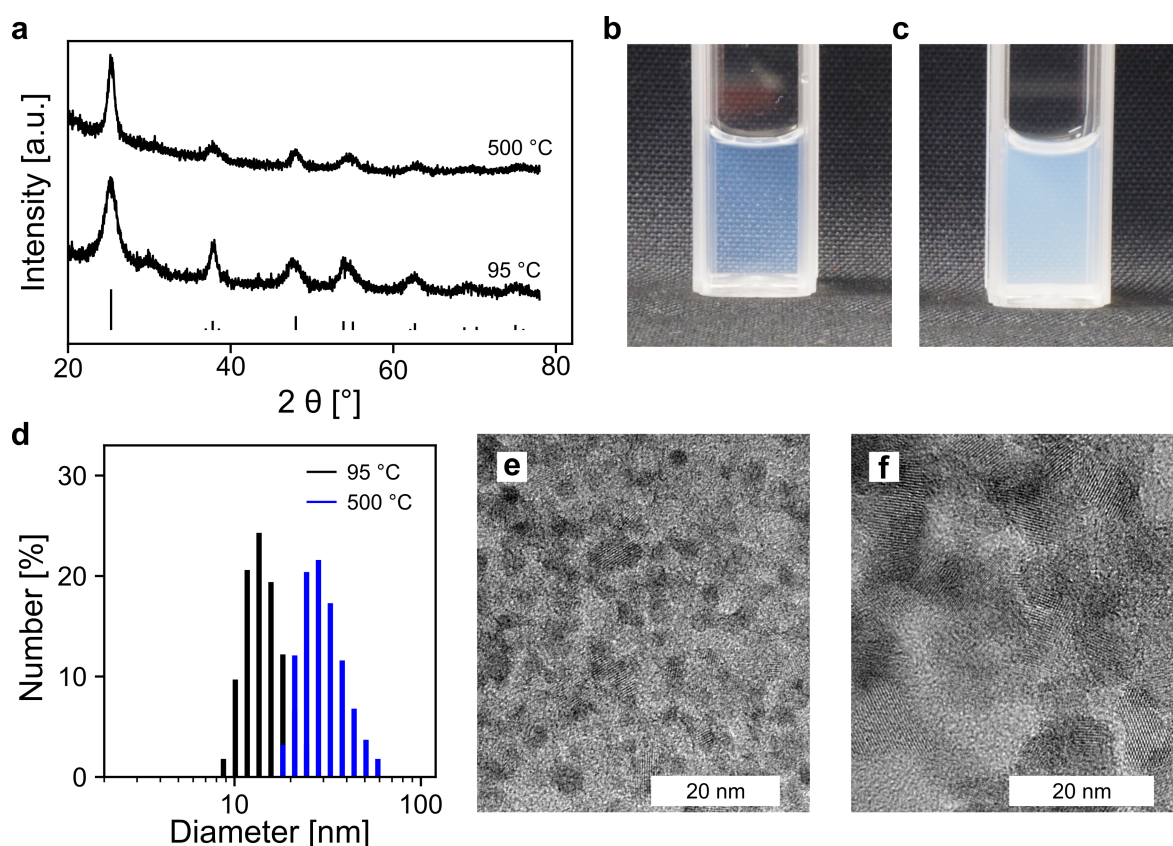


Figure 3.7: a) XRD data of TiO₂ nanoparticles treated at 95 and 500 °C along with the reference data of anatase TiO₂ (ICSD: 96946). Photographs of aqueous colloids containing TiO₂ nanoparticles at a concentration of 2 mg mL⁻¹. The particles were treated at: b) 95 °C and c) 500 °C. d) DLS measurements of the aqueous colloids of TiO₂ nanoparticles treated at 95 and 500 °C. e, f) TEM images of the TiO₂ nanoparticles treated at 95 and 500 °C, respectively.

Results and discussion

again comparable to the results obtained in water and methanol. For the nanoparticles prepared at 95 °C, diameters around 13 nm are obtained, indicating a higher degree of agglomeration. Another important aspect of colloids is their long-term stability. In this regard, the aqueous and methanolic colloids are stable for multiple weeks up to months without any signs of sedimentation. The colloids in the nonpolar solvents are less stable, which may be overcome by optimizing the ligand molecules.

In a first attempt to extend the method to nanomaterials other than ATO, the aerogel route was also applied to TiO₂ nanoparticles. Similar to ATO, DBU was used as strong base, starting from a precursor in an alkaline solution, precipitating the particles from the alkaline solution with hydrobromic acid, and heating the resulting nanoparticle suspension at 95 °C. After washing, the TiO₂ nanocrystals were redispersed in water/ethanol with the help of DBU, followed by gelation, supercritical drying, and calcination at 500 °C as described for the ATO nanoparticles. The particles consist of the anatase phase, as shown by the XRD data displayed in Figure 3.7a. Based on the Scherrer equation, a size of approx. 3 nm is obtained for the nanoparticles synthesized at 95 °C and approx. 6 nm after calcination of the aerogel at 500 °C. From TEM images of the particles prepared at 95 °C (Figure 3.7e), their average size can be estimated at 3.8 nm. When these particles are redispersed in water, DLS measurements indicate a mean particle size of 13 nm in the colloidal solution (Figure 3.7d). Therefore, the 3.8 nm TiO₂ particles are somewhat less well dispersed than the 2.7 nm ATO particles for which a DLS size of approx. 4 nm was determined in water (Figure 3.6a). In combination with the higher refractive index of TiO₂, this effect results in a more pronounced scattering of the colloidal solution (Figure 3.7b) compared with the corresponding ATO colloid (Figure 3.1i). However, after calcination of the TiO₂ aerogel at 500 °C, the DLS results are very similar to those observed for ATO: The TiO₂ nanoparticles can be redispersed in water (Figure 3.7c) as described for ATO and the DLS measurements show an aver-

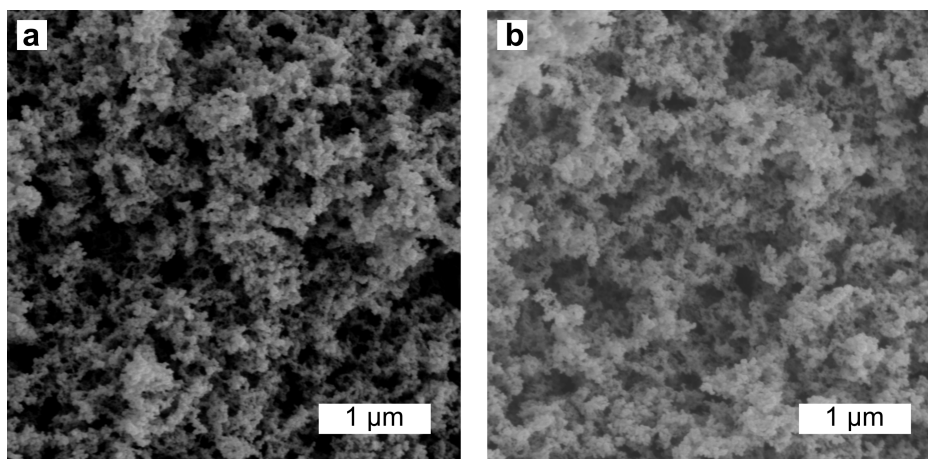


Figure 3.8: SEM images of TiO₂ aerogels a) before and b) after calcination.

Results and discussion

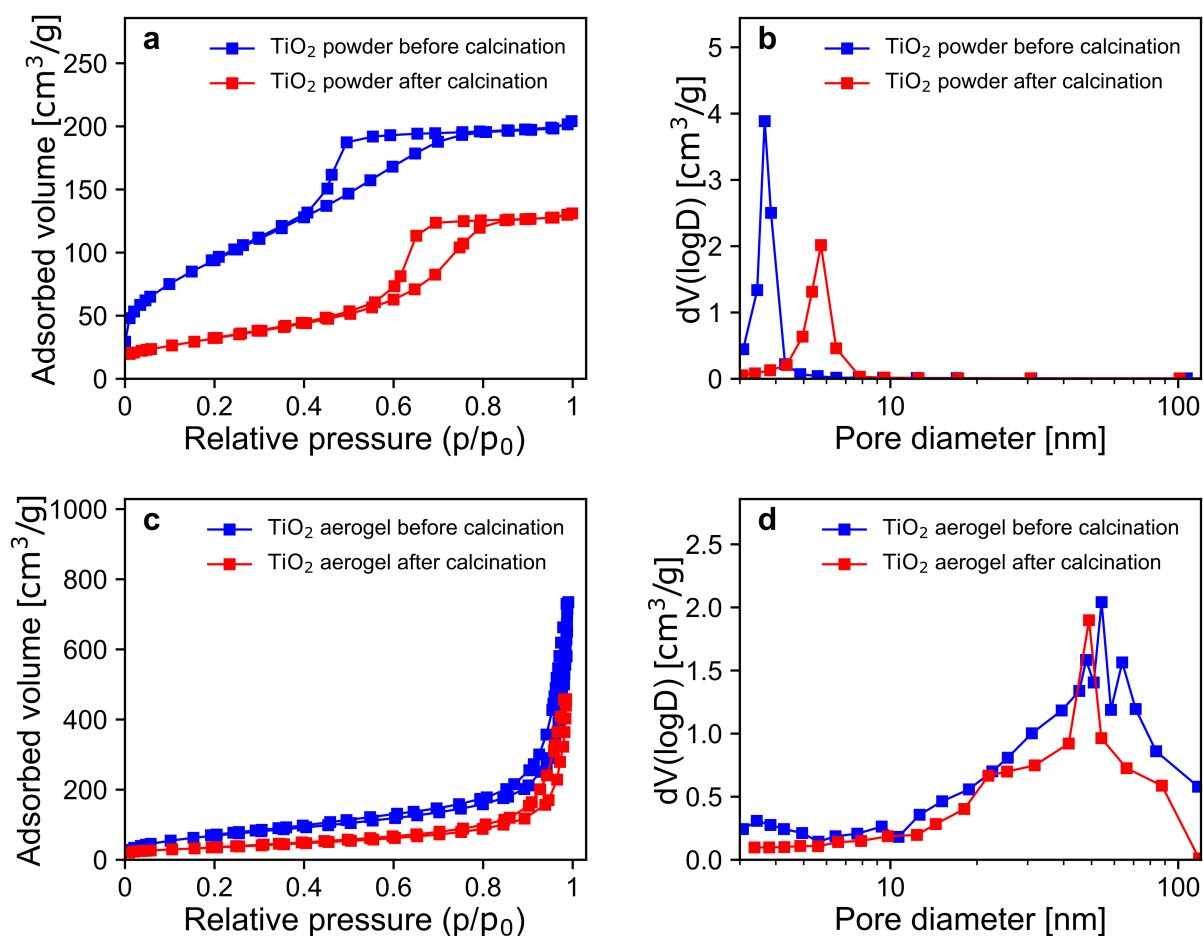


Figure 3.9: Nitrogen sorption isotherm of TiO₂ particles in the form of a) a powder and c) assembled as aerogel before and after calcination. BJH pore volume $dV(\log D)$ against pore diameter of TiO₂ particles in the form of b) a powder and d) assembled as aerogel before and after calcination. The measurements were performed by Tim Jähnichen in the group of Dirk Enke at Universität Leipzig.

Table 3.2: BET-surface area and total pore volume of TiO₂ powders and aerogels before and after calcination, obtained from the nitrogen sorption measurements displayed in Figure 3.9.

Particles	BET-surface area [m ² g ⁻¹]	Total pore volume [cm ³ g ⁻¹]
TiO ₂ powder before calcination	350	0.31
TiO ₂ powder after calcination	118	0.20
TiO ₂ aerogel before calcination	261	0.54
TiO ₂ aerogel after calcination	126	0.26

age size of approx. 28 nm (Figure 3.7d), very similar to the value of 24 nm observed for ATO. In fact, SEM images of the TiO₂ aerogels before and after calcination (Figure

Conclusion

3.8) confirm again a highly porous structure that is also supported by nitrogen sorption measurements of TiO_2 powders and aerogels (Figure 3.9 and Table 3.2). The TEM image of the calcined TiO_2 nanoparticles (Figure 3.7f) also shows some fusion as was observed for the calcined ATO nanoparticles. DLS measurements of colloidal TiO_2 solutions in toluene are shown in Figure 3.10. In this case, average diameters around 12 and 32 nm are obtained for the nanoparticles treated at 95 and 500 °C, respectively.

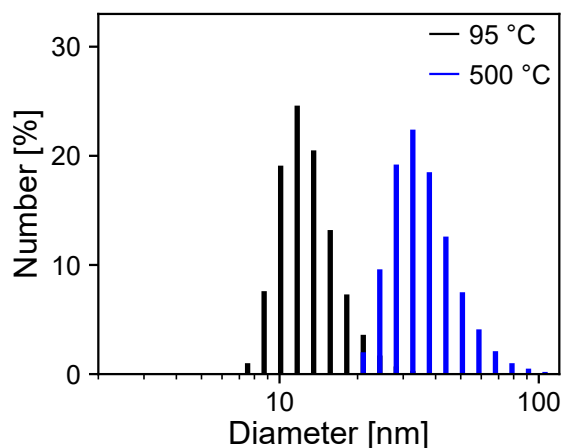


Figure 3.10: DLS measurements of TiO_2 nanoparticles redispersed in toluene after heat-treatment at 95 and 500 °C.

3.4 Conclusion

In summary, it is demonstrated that nanoparticles prepared via an aerogel route can be redispersed even after calcination. Here, ATO and TiO_2 nanoparticles were used as examples for this method. The aerogels are prepared by gelation of a colloidal nanoparticle solution followed by supercritical drying. After calcination of the aerogels at 500 °C, the nanoparticles can be redispersed to obtain stable colloidal solutions. The primary particle size is below 10 nm after calcination. It was observed that calcination only led to a slight degree of sintering resulting in particle aggregates with average hydrodynamic diameters below 30 nm according to DLS. Furthermore, colloidal solutions can be prepared with various solvents, which can be useful for potential postprocessing of the nanoparticles. The increase in material functionality due to calcination is shown for the case of ATO nanoparticles. Here, with increasing temperature treatments, an intensification of the coloration of the particles due to an increased intensity of the plasmon absorption band is observed.

4 Intercalation-free, fast switching of mesoporous antimony doped tin oxide with cathodically coloring electrochromic dyes

In the previous chapter, a synthesis route was successfully established that yields small and re-dispersible ATO nanoparticles. As highlighted, subjecting the nanoparticles to high temperatures is required to achieve full functionality, i.e., strong absorption in the IR region due to the presence of free electrons. Besides the optical properties, the presence of free electrons also has a strong influence on the electric properties of the nanoparticles since they cause much improved electrical conductivity. Therefore, the assembly of ATO nanoparticles into thin films, which provide a continuous particle network, makes them useful for electrochemical applications. Particularly mesoporous films are attractive since they offer large inner surfaces that can be decorated with other functional materials. For instance, in the field of electrochromism, these materials may be redox-active organic molecules that change their color when they are oxidized/reduced. Colloidal solutions of small, re-dispersed nanoparticles present an ideal starting point for the preparation of such mesoporous thin films. This chapter showcases that the ATO thin films display remarkable performance in electrochromic devices under conditions that cannot be realized with other materials.

Parts of this chapter were published:

Jonas Klein, Alexander Hein, Ellen Bold, Fatih Alarслан, Egbert Oesterschulze, and Markus Haase, "Intercalation-free, fast switching of mesoporous antimony doped tin oxide with cathodically coloring electrochromic dyes", *Nanoscale Advances* **2022**, 4, 2144

4.1 Introduction

Electrochromic (EC) materials allow for dynamic changes in their absorption behavior regulated by the application of electric fields^[192]. Due to this property such materials are widely investigated for displays^[193,194], smart windows^[195,196] or imaging^[197,198]. The variety of active materials include metal oxide films^[199,200], polymer films^[201–204], solubilized organic molecules^[205–207] or hybrid systems. The latter refers to a combination of an inorganic mesoporous scaffold functionalized with organic redox-active dyes. With respect to the inorganic scaffold, high transparency in the visible region (i.e., low absorption and low scattering of light), as well as good electrical conductivity in the potential range of the redox dye are required. Materials that satisfy these criteria are nanocrystalline transparent conductive oxides (TCOs), which are widely used as scaffold materials. The preparation of a mesoporous scaffold includes doctor blading of a nanoparticle paste of the desired TCO onto a conductive substrate and subsequent calcination. The TCO layer is then functionalized with an organic dye by anchoring the dye molecules to the large inner surface of the mesoporous layer. Standard anchoring groups of the dyes are carboxylate or phosphonate moieties^[208]. Concerning the performance of the dye, an uncolored state with high transparency and a colored state with a large extinction coefficient are desirable. By choosing appropriate materials, such inorganic-organic hybrid systems allow for high electrochromic contrasts as well as fast switching times due to fast electron transport throughout the mesoporous film^[209–211].

A class of materials that are widely employed as cathodically coloring dyes are substituted 4,4'-bipyridinium salts commonly known as viologens. Their popularity is based on their facile synthesis, tunable absorption properties, and high stability^[212]. Furthermore, the redox potential of viologens is only slightly negative, which is beneficial with respect to the power consumption of EC devices^[213]. In combination with viologens, titanium dioxide (TiO₂) is widely applied to form a mesoporous TCO scaffold^[214,215]. TiO₂ layers offer exceptional transparency in the visible region and TiO₂ is also readily available^[216]. However, the electrical conductivity of TiO₂ is restricted to negative potentials unless special electrolytes are chosen allowing the broadening of the potential range^[217]. An example are electrolytes containing small cations, e.g. lithium, which are known to shift the conductivity range of TiO₂ towards more positive potentials. On the downside, using electrolytes with lithium ions can cause lithium insertion in the inorganic scaffold material when the electrodes are sufficiently negatively polarized. Such insertion processes cause mechanical stress within the oxidic nanoparticles due to volume expansion and thereby can lead to performance degradation^[218].

Besides TiO₂, the combination of other TCOs with viologens has been reported^[219–221]. Among these materials, antimony doped tin oxide (ATO) is very appealing with respect

to its high electrical conductivity over a wide potential range. However, in the reports so far, ATO/viologen hybrid layers display inferior performance compared to other TCO/viologen systems^[221], especially when the nanoparticle size is decreased^[222]. The latter aspect, namely the morphology of the TCO layer, is known to have considerable influence on the performance of such electrochromic systems^[223]. Therefore, ATO layers are primarily employed as counter electrodes in EC devices in the form of ion storage layers^[224,225] or in combination with anodically coloring materials^[226–228]. To improve the performance of ATO/viologens layers, multiple factors have to be taken into account. With ATO being an n-conductive oxide, the charge of the free electrons in the conduction band is compensated for by Sb^{5+} dopant ions occupying Sn^{4+} sites in the crystal lattice^[229]. One potential drawback of ATO is its intrinsic absorbance in the infrared region which extends into the visible region. The strong NIR absorption is caused by the high concentration of free electrons in the conduction band^[230]. However, as this optical behavior depends on the antimony doping level, a low doping concentration could still offer acceptable transparency while the electrical characteristics are less dependent on the electrolyte composition. Moreover, due to the high mobility of the electrons, comparatively high conductivity of the particles may already be achieved with low antimony concentrations^[231]. A low doping concentration is also known to provide more homogeneous doping, especially when an Sb^{5+} rather than an Sb^{3+} source is used in the synthesis, while increased antimony contents lead to accumulation of antimony at the surface of the particles^[190]. Too high antimony concentrations, however, decrease the conductivity of ATO^[231,232]. This is crucial when small nanoparticles are used to form the mesoporous layers. While small particles offer better optical properties, mesoporous layers composed of small particles are particularly susceptible to increased contact resistance between the nanoparticles. For mesoporous layers, homogeneously doped particles with a low concentration of Sb^{5+} should therefore be beneficial to increase the performance of ATO/viologen systems.

In the present study, the behavior of a mesoporous ATO layer consisting of small nanoparticles (5 nm) in combination with a viologen is investigated. First, the spectroelectrochemical response of the bare metal oxide layer is investigated. Since the electrolyte may have a great impact on the performance, an electrolyte containing lithium and a lithium-free electrolyte are used to highlight the benefits when using the latter. In the next step, the spectroelectrochemical performance of particles with different antimony doping concentrations is investigated to choose the optimal Sb content. Comparing the performance of viologen modified ATO and TiO_2 layers with a non-intercalating electrolyte highlights the superiority of ATO in such a system. Finally, the viologen functionalized ATO layer is implemented in a sealed two-electrode device. The counter electrode of this device also consists of a mesoporous ATO layer but with an anodi-

cally coloring organic dye. The selection of the dyes for the two electrodes is based on preliminary works^[198,209] and enables the devices to achieve high contrasts. Also in the device, the non-intercalating electrolyte is utilized. In particular, it is shown that the switching times of the ATO electrodes are remarkably fast, despite the use of electrolytes with large cations and the use of ATO nanocrystals of small size.

4.2 Experimental

ATO nanoparticle synthesis:

ATO particles with an antimony doping concentration of 2% were synthesized as follows: 2 mmol potassium hexahydroxoantimonate (0.53 g, Merck) and 2 mL hydrogen peroxide solution (30%, Merck) were added to a solution of 100 mmol potassium hydroxide (5.61 g, Merck) in 400 mL water and subsequently heated at 60 °C until a clear solution was obtained. At room temperature, 98 mmol potassium hexahydroxostannate (29.3 g, Sigma Aldrich) and 250 mmol hydrochloric acid (21 mL (37%) diluted to a total of 100 mL, Fluka) were subsequently added. After heating the solution to 95 °C for 30 min, a 1 M potassium hydroxide solution was added dropwise until the solution became clear followed by further heating for 30 min. The pH of the cooled solution was adjusted to 4 by the addition of hydrochloric acid. The precipitate was centrifuged and repeatedly washed with water until the supernatant remained turbid after centrifugation. A colloidal solution in 200 mL water was obtained after the addition of 2 mL 1,8-diazabicyclo[5.4.0]undec-7-en (DBU, purchased from TCI) to the precipitate. The colloid was then loaded into a Teflon-lined autoclave (400 mL capacity) and heated to 200 °C for 5 h after purging the solution with nitrogen for 20 min. In the next step, the volume of the colloid was reduced to 50 mL on a rotary evaporator followed by dialysis (MWCO 6000–8000) for 2 days against water. Finally, all solvent was removed on a rotary evaporator yielding the ATO nanoparticle powder. In the same manner, undoped SnO₂, as well as ATO nanoparticles with antimony concentrations of 5% and 15% were synthesized.

Electrode preparation:

Mesoporous ATO nanoparticle layers were prepared on fluorine-doped tin oxide coated glass ($\sim 7 \Omega \text{ sq}^{-1}$, Sigma Aldrich) by the doctor blade method. Prior to doctor blading, the substrates were cleaned by repeated ultrasonication in water and acetone followed by plasma cleaning (Diener Femto). A paste was prepared by mixing 2 g of the synthesized ATO nanoparticles and 0.5 g of hydroxypropylcellulose (Alfa Aesar) in 10 mL of a 1/1 water/ethanol mixture. After doctor blading, the electrodes were heated to 450 °C with a ramp of 5 °C min⁻¹ and a dwelling time of 1 h at 450 °C. The resulting films had

Experimental

a thickness of approx. 3.5 μm . In a similar way, mesoporous TiO_2 electrodes (approx. 3.2 μm) were prepared from a commercial TiO_2 paste (Ti-Nanoxide T/SP, Solaronix). For the modification of the electrodes with a redox-active dye, the mesoporous layers were immersed into a 4 mM solution of 1-(4-cyanophenyl)-1'-(2-phosphonoethyl)-4,4'-bipyridin-1-ium (Vio) in ethanol for 16 h.

Spectroelectrochemical characterization:

Bare and dye-modified electrodes were characterized in a three-electrode setup with a platinum wire counter electrode and an Ag/AgCl reference electrode. As electrolytes, we used either lithium perchlorate (Sigma Aldrich) or tetrabutylammonium perchlorate (Sigma Aldrich) in propylene carbonate (Sigma Aldrich) with 1 M concentration. A Gamry Interface 1000 potentiostat was used to perform electrochemical experiments. Optical measurements were recorded using an Avantes AvaLight-DHc light source and an Avantes AvaSpec-3648 spectrometer. The measurements were performed in an electrochemical cell with an attached cuvette, into which the electrodes were immersed. A blank FTO glass and the electrolyte filled cuvette were set as optical reference.

Physical characterization:

The nanoparticles were characterized by X-ray powder diffraction (XRD) using a Panalytical Empyrean diffractometer with Bragg–Brentano geometry, Cu K- radiation, and a step size of 0.026° for 2θ . Transmission electron microscopy (TEM) images were recorded on a JEOL JEM-2100Plus with an EM-24830FLASH camera (JEOL). The cathode material was LaB_6 operated at 200 kV. Dynamic light scattering (DLS) measurements of aqueous colloidal solutions of ATO nanoparticles after autoclave treatment were performed on a Malvern Zetasizer Nano ZSP. Scanning electron microscopy (SEM) images were obtained with a Zeiss Auriga scanning electron microscope using an in-lens detector. The acceleration voltage was 3 kV and the samples were sputtered with platinum/iridium.

Device fabrication:

In the device, indium tin oxide coated glass was used as the substrate. The device consisted of a mesoporous 3 μm thick ATO working electrode modified with Vio and a similar (3 μm) ATO counter electrode modified with [4-(diphenylamino) benzyl]-phosphonic acid (TAA). The modification of the ATO electrode with TAA was performed by the immersion of the electrode into a 4 mM solution of TAA in ethanol for 16 h. As the electrolyte, a 1 M solution of tetrabutylammonium perchlorate in propylene carbonate was used. The details of the device fabrication are reported elsewhere^[233].

4.3 Results and discussion

Whether a material is suited for application in an electrochromic device depends on the material's optical and electrochemical properties. Herein the electrochromic system is based on two electrodes each consisting of a mesoporous ATO nanoparticle layer modified with an electrochromic dye. As outlined in the Introduction, a homogeneous distribution of the dopant ions in ATO nanoparticles is achieved with Sb^{5+} ions and low doping concentrations. Thus, a stable Sb^{5+} precursor is required for the synthesis. The widely utilized SbCl_5 for instance is susceptible to degradation to SbCl_3 . Therefore, we used hexahydroxostannate and hexahydroxoantimonate as precursors and initially added hydrogen peroxide to the hexahydroxoantimonate solution to oxidize all possible present Sb^{3+} ions. Previous reports in which these precursors were used also confirmed high $\text{Sb}^{5+}/\text{Sb}^{3+}$ ratios^[234]. Here, the nanoparticles were obtained by precipitation through the addition of an acid followed by autoclaving of the nanopar-

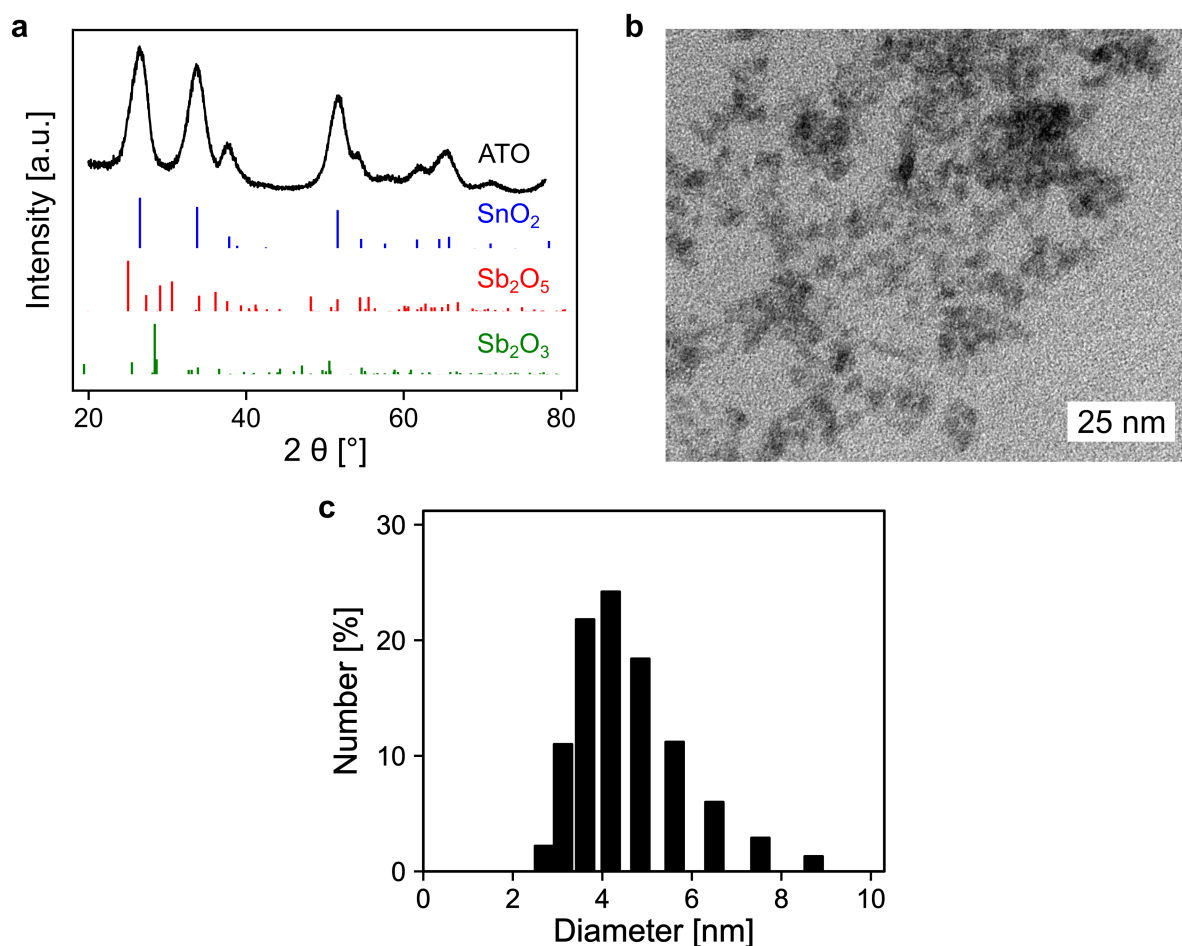


Figure 4.1: a) XRD of ATO nanoparticles (2% Sb) along with the reference spectra of SnO_2 (ICSD: 39177, blue), Sb_2O_5 (ICSD: 8050, red) and Sb_2O_3 (ICSD: 2033, green). b) TEM image of ATO nanoparticles after autoclave treatment. c) DLS measurement of colloidal ATO nanoparticles after synthesis and autoclave treatment measured in water.

Results and discussion

ticle colloid as described in the Experimental section. The characterization of the ATO nanoparticles with an antimony doping concentration of 2% was carried out by X-ray powder diffraction (XRD). As shown in Figure 4.1a, the particles crystallized in a tetragonal cassiterite structure. There are no peaks corresponding to antimony oxide species such as Sb_2O_5 or Sb_2O_3 . Therefore, successful integration of the dopant ions into the SnO_2 lattice can be anticipated. According to the Scherrer equation, the particles have a size of around 3.7 nm. The particles were also characterized by transmission electron microscopy (TEM) which also confirms the small size of the nanoparticles (Figure 4.1b). However, due to aggregation during drying on the TEM grid, a detailed analysis of sizes from the TEM image is difficult. Dynamic light scattering (DLS) measurements of the colloidal nanoparticles also show average sizes of around 4 nm (Figure 4.1c). With these nanoparticles, a paste was prepared which was then used to fabricate the electrodes by the doctor blade method on fluorine-doped tin oxide coated glass (FTO). After calcination at 450 °C, the ATO layers have a thickness of approx. 3.5 μm as can be estimated from the scanning electron microscopy (SEM) image displayed in Figure 4.2a. Calcination also leads to an increase of the particle size to around 5 nm. From the magnified SEM image (Figure 4.2b), the mesoporous nature of the layers can be confirmed. Consistent with the small particle size, the ATO layers are very densely packed with small pores. As mentioned in the Introduction, the morphology of mesoporous layers can influence the electrochemical performance and is reported to benefit from larger particles^[222,223]. Especially the contact resistance between the ATO particles has to be considered since their size is very small.

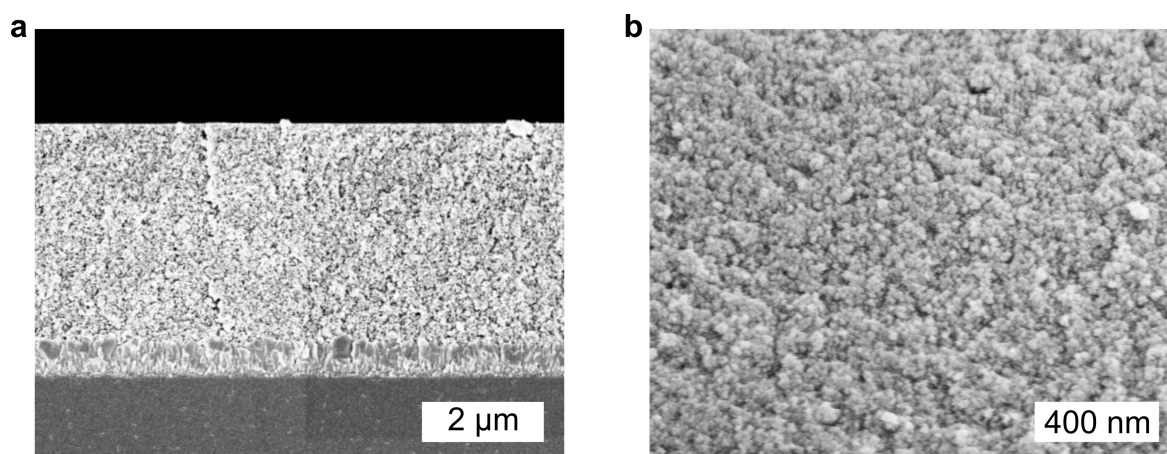


Figure 4.2: a) Cross-sectional SEM of ATO layers on FTO. b) Magnified cross-sectional view displaying the mesoporous structure of the nanoparticle layers.

Therefore, the electrochemical behavior of the pure ATO layers was initially investigated in a three-electrode setup. Since the performance of the electrodes also depends on the electrolyte composition, the experiments were performed with both 1 M

Results and discussion

lithium perchlorate (LiClO_4) and 1 M tetrabutylammonium perchlorate (TBAP) in propylene carbonate (PC) as electrolytes. The corresponding cyclic voltammograms (CV's) are displayed in Figure 4.3a. With TBAP/PC as the electrolyte, ATO shows a capacitive current over the whole chosen potential region indicating electron injection into the nanoparticle layer and the formation of an electrochemical double layer^[230]. The current decreases towards positive potentials due to the depletion of electron density at the nanoparticle surface^[235]. With LiClO_4 /PC as the electrolyte, the general characteristics are comparable to that observed with TBAP/PC but with some distinct differences. ATO again shows a capacitive current over the complete potential region. Compared to TBAP, however, the current is significantly higher. This can be explained by the difference in the size of the cations present in the electrolyte and the fact that a tetrabutylammonium ion occupies more space in the capacitive double layer than a lithium

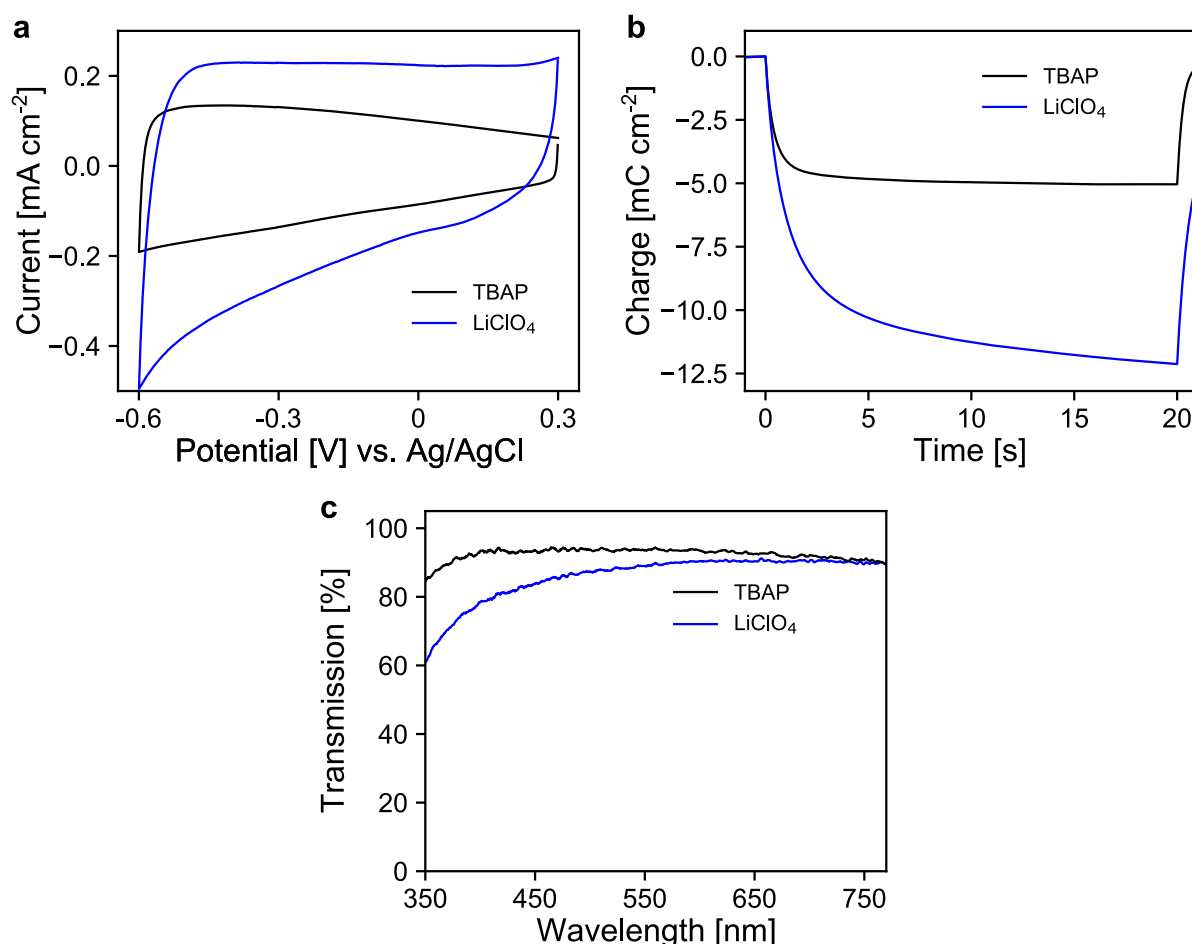


Figure 4.3: a) CV's of ATO (2% Sb) mesoporous electrode layers measured in TBAP/PC and LiClO_4 /PC with a scan rate of 20 mV s^{-1} . b) Coulometric measurement for a potential step between +0.3 V and -0.6 V vs. Ag/AgCl in both electrolytes. c) UV/VIS transmission spectra of ATO electrodes (after negative polarization) without an applied potential for both electrolytes; optical reference: an electrolyte-filled cell with blank FTO glass.

ion. Therefore, fewer cations can be incorporated into the double layer when TBAP is used, thereby reducing the number of electrons that can be injected into the ATO layer. The noticeable increase of current at negative potentials as well as the observation that the current towards positive potentials does not drop as sharply as it occurred with TBAP can be assigned to lithium intercalation into the nanoparticle layer. With respect to the long-term performance of such metal oxide layers, lithium intercalation is unfavorable due to the mechanical stress exerted on the nanoparticles due to volume expansion. Especially ATO layers are known to degrade upon lithium insertion^[218]. With TBAP/PC on the other hand, no intercalation phenomena are observed. As already mentioned, the charge consumed by the pure ATO films due to the formation of electrochemical double layers differs significantly based on the electrolyte composition and is further emphasized in a coulometric potential step measurement (Figure 4.3b). In the case of the lithium-containing electrolyte, not only is the charge increased by a factor of 2.4 compared to TBAP, but the response time is also slower with LiClO_4 . Along with the electrochemical properties of the pure metal oxide layers, their optical properties were also investigated by means of ultraviolet-visible spectroscopy (UV/VIS). The corresponding transmission spectra of the ATO layers without an applied potential in both electrolytes are displayed in Figure 4.3c. Notably, the spectra were recorded after the layers were subjected to polarization at negative potentials. In the case of the TBAP/PC electrolyte, the ATO layer displays high transparency over the complete visible region. In fact, the average transmission of the electrode between 350 and 750 nm reaches 92.6%. With LiClO_4 /PC, the ATO layer suffers from reduced transparency at lower wavelengths after negative polarization, which gives the electrode a permanent yellow coloration. This observation is again a result of lithium intercalation into the nanoparticle layer, which irreversibly degrades the electrode. Therefore, in this case, the average transmission reaches only 86%. From the results presented so far, it can be concluded that the mesoporous ATO layers display better performance with a non-intercalating electrolyte. This is due to the absence of undesirable side effects based on intercalation processes. Furthermore, with respect to the application in electrochromic devices, the charge consumed by the electrode has to be considered since this charge has to be compensated for by the counter electrode in the device. Therefore, utilizing TBAP/PC is again favorable since less charge is consumed. Thus, this electrolyte composition was used in the following experiments.

After the selection of a suitable electrolyte, the spectroelectrochemical behavior of mesoporous layers of ATO nanoparticles with varying antimony doping concentrations were investigated. These were namely undoped SnO_2 (ATO 0), 2% Sb (ATO 2), 5% Sb (ATO 5) and 15% Sb (ATO 15) and experimentally determined by X-ray fluorescence measurements (Table A1, Appendix). The XRD data of the nanoparticles are shown

Results and discussion

in Figure 4.4a and confirm that only the pure SnO_2 phase was obtained. The mean size of the particles slightly increases from approximately 3 to 4.5 nm with decreasing antimony concentration based on the Scherrer equation. The CV measurements of the electrodes are displayed in Figure 4.4b. The response of all electrodes follows the same general scheme. Particularly, in all cases again a capacitive current can be observed, which decreases towards positive potentials as discussed earlier. The layers with undoped nanoparticles however carry considerably less current at positive potentials, which indicates a limitation with respect to the conductivity of the nanoparticle layer in the respective potential region. All of the doped nanoparticles on the other hand show better conductivity at positive potentials due to the n-doped nature of the nanoparticles. A second observation concerns the differences in the capacitive current

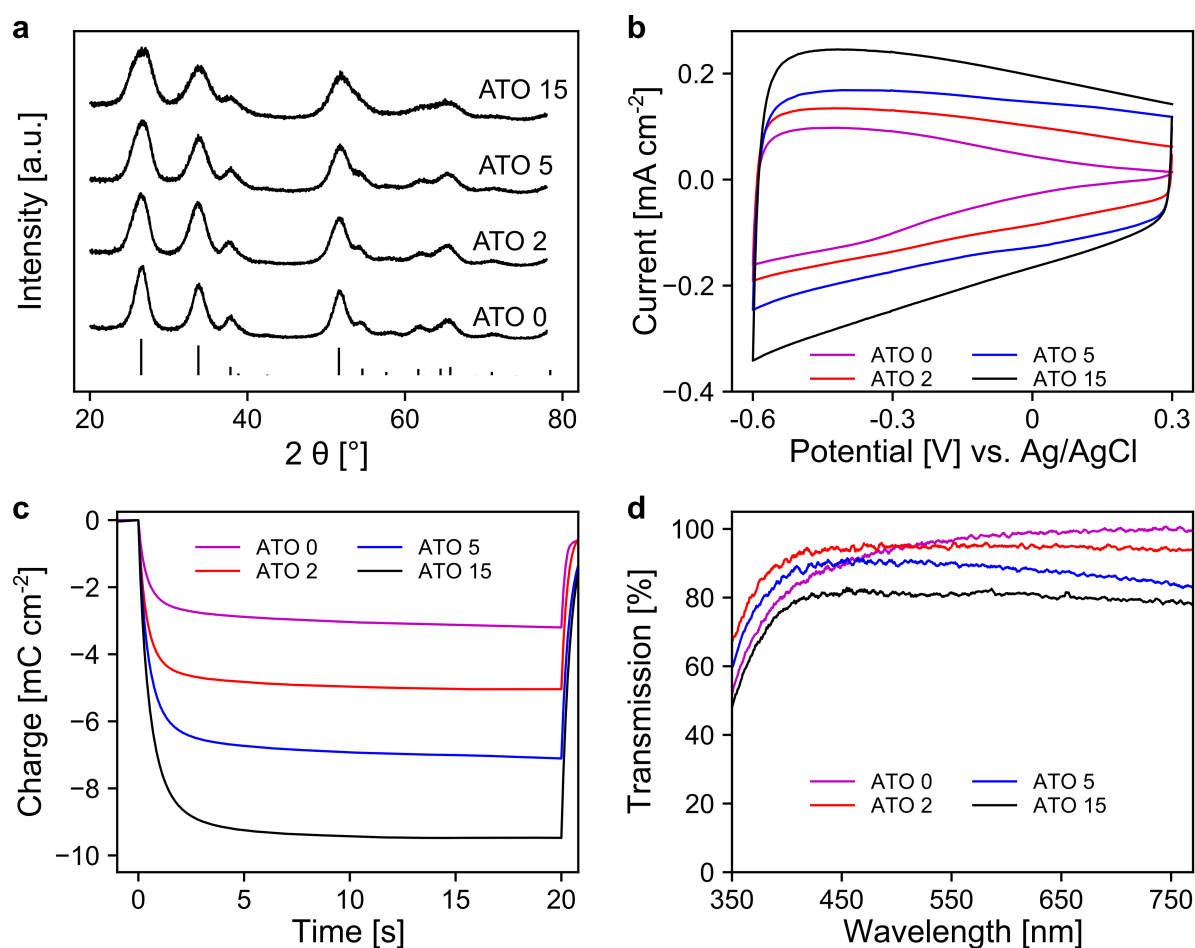


Figure 4.4: a) XRD of ATO particles after autoclave treatment with antimony contents of 0%, 2%, 5% and 15% along with a reference spectrum of SnO_2 (ICSD: 39177). b). CV's of ATO mesoporous electrode layers with different antimony doping levels measured in TBAP/PC with a scan rate of 20 mV s^{-1} . c) Coulometric measurement for a potential step between $+0.3 \text{ V}$ and -0.6 V vs. Ag/AgCl. d) UV/VIS transmission spectra of ATO electrodes at $+0.3 \text{ V}$ vs. Ag/AgCl; optical reference: an electrolyte-filled cell with blank FTO glass.

Results and discussion

of the electrodes. Here, with increasing antimony content the capacitive current also increases as the antimony content influences the number of electrons that can be injected into the nanoparticle layers. This is again also reflected in the charge stored by the bare nanoparticle layers as shown in Figure 4.4c. The corresponding values range from around 3 mC cm^{-2} for the undoped SnO_2 to around 11 mC cm^{-2} for the particles doped with 15% antimony. Again, this has to be considered with respect to charge compensation by the counter electrode in an electrochromic device. The UV/VIS spectra of the electrodes are presented in Figure 4.4d. The undoped nanoparticles show the highest transparency at higher wavelengths. However, towards the UV region, these electrodes suffer from a similar problem to the ATO electrode measured with a lithium-containing electrolyte. This indicates that after negative polarization, charge carriers are irreversibly trapped within the SnO_2 particle layer, which absorb in the blue spectral region and therefore the electrodes appear yellowish colored. Already with an antimony content of 2%, this effect does not appear anymore, which can be attributed to the better conductivity of the doped nanoparticles, which allows the extraction of all injected electrons after negative polarization. However, compared to undoped SnO_2 , the ATO 2 electrodes are slightly less transparent at higher wavelengths due to the presence of free electrons, which compensate for the introduced Sb^{5+} ions. With increasing doping concentration, this effect becomes even more pronounced, and the overall transparency drops. In fact, while the ATO 2 electrodes display an average transmission of 94.5%, this value is reduced to 79% in the case of the ATO 15 nanoparticle layers. From these experiments, it therefore can be concluded that a low antimony doping concentration of 2% ensures sufficient conductivity in the desired potential range but still offers high transparency over the visible spectral region.

In the next step, a redox-active dye, namely 1-(4-cyanophenyl)-1'-(2-phosphonoethyl)-4,4'-bipyridin-1-ium (viologen), was anchored to the mesoporous nanoparticle layers via chemisorption. For the coloration of the dye, electrons are transported through the metal oxide scaffold to the organic molecules and vice versa for decoloration. The antimony doping concentration of the ATO nanoparticles was 2% and TBAP/PC was utilized as the electrolyte. A CV of a modified electrode is shown in Figure 4.5a, which displays a set of reversible peaks associated with the reduction/oxidation of the viologen dye. Thus, the intrinsic conductivity of ATO still allows unrestricted switching of the dye despite the absence of lithium within the electrolyte. Since the reduction of the dye results in its coloration, the corresponding UV/VIS spectra were recorded as shown in Figure 4.5b. In the colored state ($-0.6 \text{ V vs. Ag/AgCl}$), the transparency of the electrode is reduced to 25%. At $+0.3 \text{ V}$ (transparent state), the modified electrode reaches an average transmission of around 91%. For comparison, mesoporous electrodes of TiO_2 , which is the standard scaffold in combination with viologens as outlined in the In-

Results and discussion

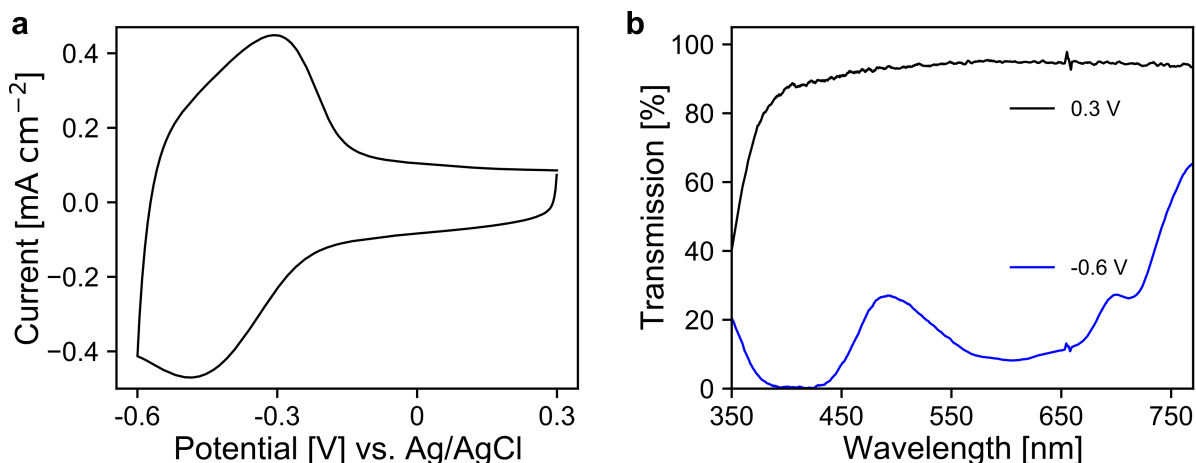


Figure 4.5: a) CV of a viologen modified ATO mesoporous electrode measured with TBAP/PC as the electrolyte with a scan rate of 20 mV s^{-1} . b) UV/VIS transmission spectra of the viologen modified ATO electrode in the colored and bleached state. Optical reference: an electrolyte-filled cell with blank FTO glass.

roduction, were investigated. For this purpose, a commercial nanoparticle paste was used. The layers had a thickness of approx. $3.2 \mu\text{m}$, comparable to the ATO layers, and also displayed a mesoporous structure as shown in Figure 4.6a/b. After modification with the viologen, CV measurements of these electrodes were performed also with TBAP/PC as the electrolyte. As shown in Figure 4.6c, the behavior of the viologen/ TiO_2 electrode displays distinct differences when compared to the viologen/ATO electrodes. While the reduction of the dye remains possible, the corresponding peak in the CV is shifted towards more negative potentials. Moreover, only a small oxidation peak is observed, which indicates electron trapping within the mesoporous layer. This behavior is related to the flat band potential of TiO_2 , which is known to be shifted towards negative potentials in the absence of cations like lithium^[214]. From the CV of a bare TiO_2 electrode displayed as inset in Figure 4.6c, it is evident that the TiO_2 layer only shows considerable electrochemical activity at negative potentials, whereas the doped ATO electrodes provide conductivity even at positive potentials as discussed above. The restricted oxidation of the viologen with TiO_2 as the scaffold is also evident from the UV/VIS spectra shown in Figure 4.6d. Before the measurement, the electrode displayed an average transmission of 91.2%, which is reduced to 39.4% when a potential of -0.8 V vs. Ag/AgCl is applied. While decoloration remains possible to some degree, the process takes a considerably longer time compared to the viologen/ATO system. After one minute of polarization at $+0.3 \text{ V}$, the transmission of the viologen/ TiO_2 electrode reaches only 75.8%. Therefore, these results demonstrate that mesoporous ATO electrodes in combination with viologens are more suitable compared to TiO_2 when non-intercalating electrolytes such as TBAP are used.

Finally, the performance of the dye-anchored electrodes was further investigated in a

Results and discussion

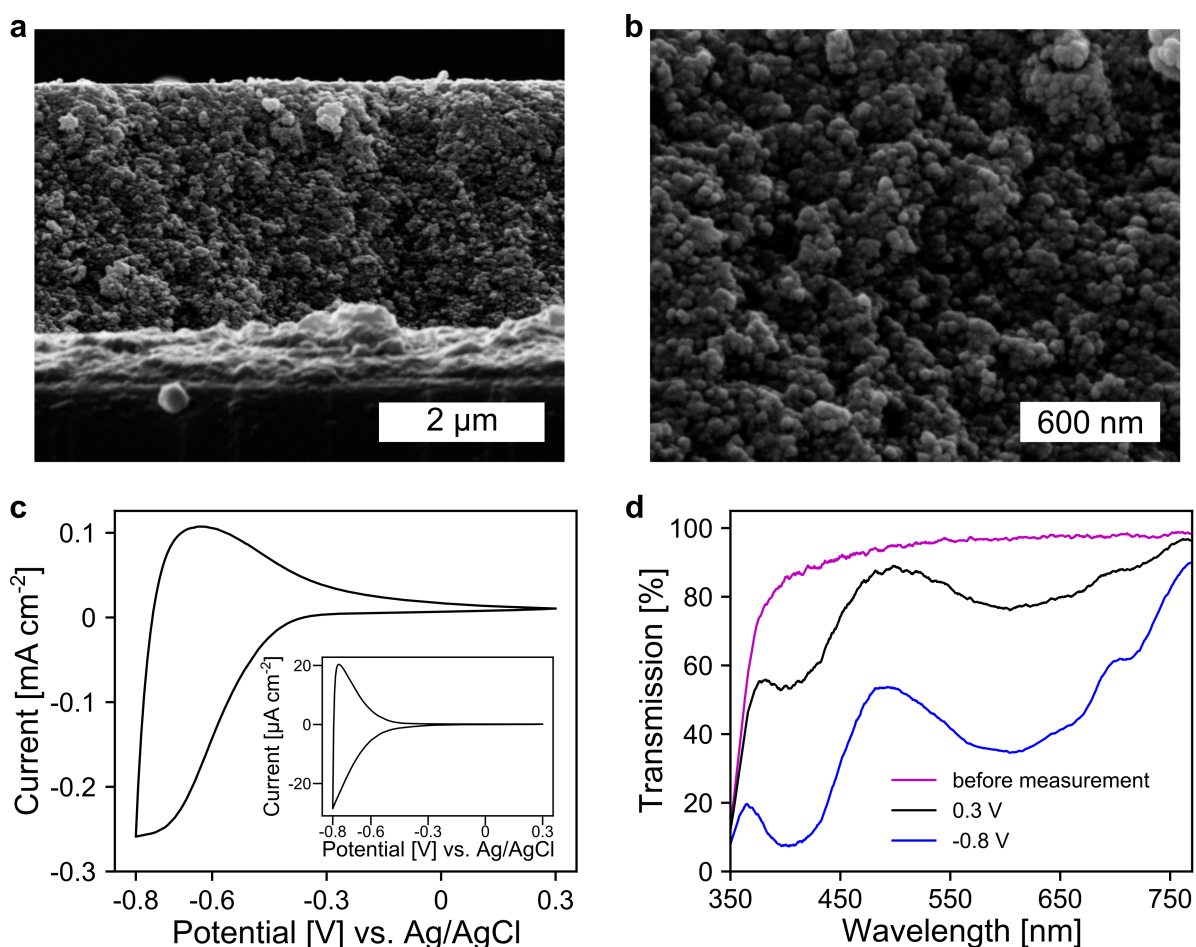


Figure 4.6: a) Cross section SEM of TiO₂ layers on FTO. b) Magnified cross section view displaying the mesoporous structure of the nanoparticle layers. c) CV of a viologen modified and a bare (inset) TiO₂ mesoporous electrode measured with TBAP/PC as the electrolyte with a scan rate of 20 mV s⁻¹. d) UV/VIS transmission spectra of the viologen modified TiO₂ electrode in the colored and bleached state. Optical reference: an electrolyte-filled cell with blank FTO glass.

sealed two-electrode device. For both electrodes, 3 μm mesoporous ATO nanoparticle layers, both doped with 2% Sb, were used as scaffolds. The working electrode was again modified with the aforementioned viologen. In the case of the counter electrode, a triarylamine based electrochromic dye, namely [4-(diphenylamino)benzyl]phosphonic acid (TAA), was used. TAA is an anodically coloring dye that undergoes oxidation on the counter electrode while the viologen is reduced on the working electrode, which allows fast switching of the device. Furthermore, the oxidation of TAA is also associated with a coloration that contributes to the overall contrast of the device. Detailed information about the ATO/TAA combination has been previously reported^[226]. A scheme of the device setup as well as the structures of the dye molecules is shown in Figure 4.7a. The electrolyte was again a 1 M solution of TBAP in PC. The transmission spectra of the device are displayed in Figure 4.7b. In the colored state (-1.7 V), the transmission

Results and discussion

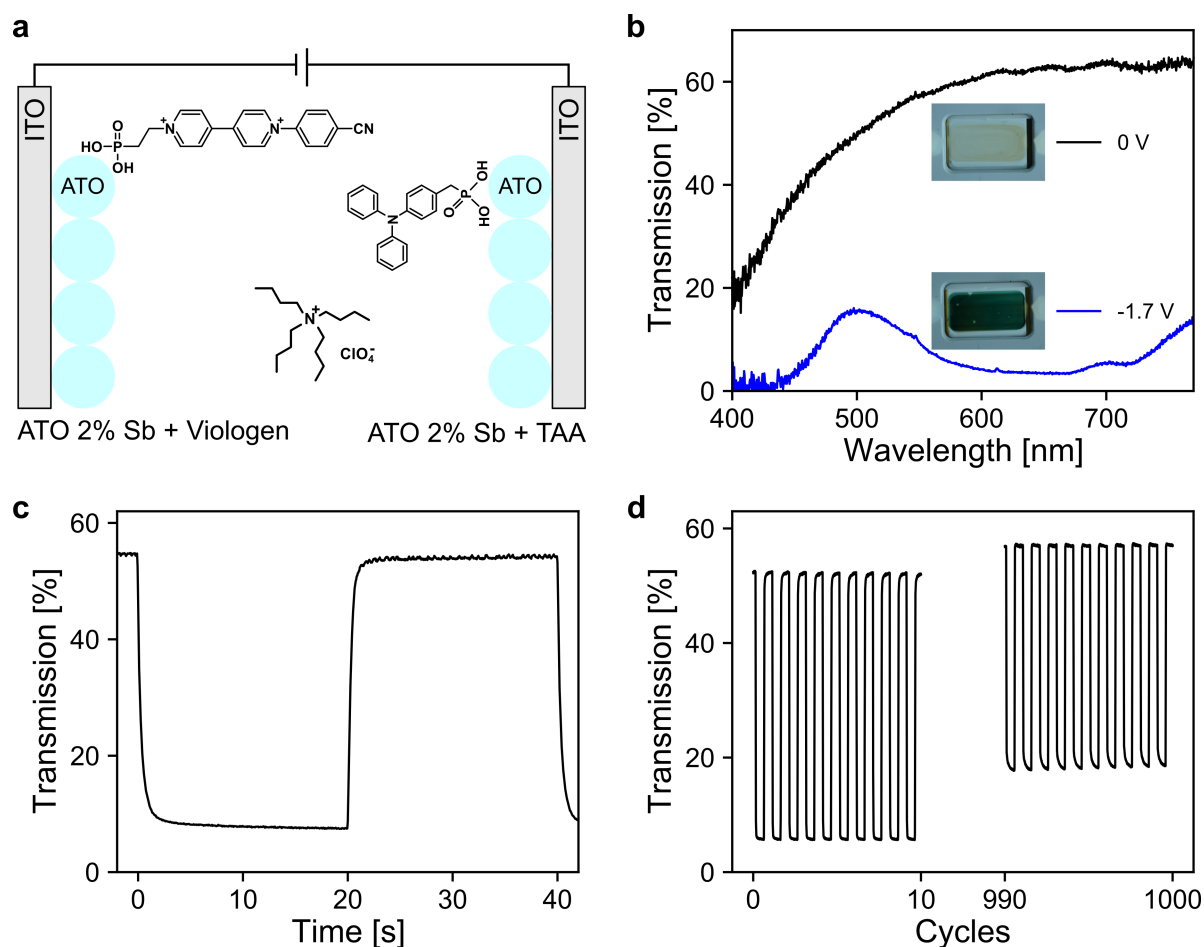


Figure 4.7: a) Schematic setup of the electrochromic device. b) Transmission spectra of the device at 0 V and -1.7 V along with images of the device in both states. c) Time depended transmission change for one switching cycle. d) Transmission change over 1000 (de)coloration cycles. The measurements were performed by Dr. Alexander Hein in the group of Egbert Oesterschulze at Technische Universität Kaiserslautern.

is reduced to 7% (average transmission over the visible range) due to the combined absorption of both dyes. The transmission value in the bleached state (0 V) reaches 62.4% (at 650 nm). The corresponding images of the device in both the uncolored and the colored state are also presented in Figure 4.7b. Another important characteristic of an electrochromic device is the switching time. Thus, time-series measurements for one reversible potential step were recorded (Figure 4.7c). The $1/e$ switching times for coloration and decoloration are 0.3 s and 0.4 s, respectively. Considering the dense morphology of the ATO layers in combination with the large cation of the electrolyte, achieving such fast switching times is remarkable. Finally, the long-term performance of the device was investigated. For this purpose, the device was subjected to 1000 switching cycles, while monitoring the transmission as displayed in Figure 4.7d. The device exhibits satisfactory stability over prolonged cycling since the electrochromic contrast only drops to 84% of its initial value after 1000 switching cycles.

4.4 Conclusion

In summary, mesoporous ATO electrodes with a low antimony concentration and small particle size are presented as a promising material for combination with cathodically coloring dyes in electrochromic devices. Comparing the spectroelectrochemical response between LiClO_4/PC and TBAP/PC as electrolytes showed that the utilization of the latter is beneficial with ATO. In this case, conductivity over the desired potential range is retained without impairment of the transparency, which occurs with the lithium-containing electrolyte due to intercalation after negative polarization. Furthermore, an antimony doping concentration of 2% was chosen as optimum as it enables the best compromise between electrical conductivity and optical transparency compared to undoped particles as well as higher antimony concentrations. The viologen modified ATO electrode, in combination with TBAP as the electrolyte, exhibited fully reversible (de)coloration of the dye compared to a similar electrode based on TiO_2 , which displayed restricted decoloration. Finally, the viologen/ATO electrode was applied as the working electrode in a two-electrode device with a triphenylamine/ATO based counter electrode. The device allowed fast switching (below 0.5 s) and displayed good long-term stability over 1000 cycles as it retained 84% of its initial contrast.

5 Cerium-modified mesoporous antimony doped tin oxide as intercalation-free charge storage layers for electrochromic devices

Mesoporous thin films of ATO nanoparticles offer electrical conductivity over a wide potential range. As discussed in the preceding chapter, making use of this property, an electrochromic device was fabricated that displayed fast switching times even with an electrolyte containing a large non-intercalating cation. The device was constructed with an ATO layer to which a viologen derivative was anchored as the main coloring electrode. To balance the charges and increase the electrochromic contrast, the second electrode (counter electrode) also consisted of an ATO layer that was also modified with an organic dye. Thus, both dyes contribute to the transmission profile of the device. This, however, may be undesirable when the transmission profile of the first dye alone provides the desired optical properties of the device. An idealized example would be a dye that transitions from a completely transparent state over intermediate gray-colored states to a black-colored state. Such cases require that the counter electrode exhibits optically passive behavior while still being able to provide the amount of charge that is consumed on the coloring electrode. Based on the previous chapter, the charge storage mechanism should also work with non-intercalating electrolytes to be compatible with the ATO/viologen system. This section, therefore, explores the applicability of mesoporous ATO electrodes that are decorated with redox-active cerium species as capable charge storage layers.

Parts of this chapter were published:

Jonas Klein, Fatih Alarслан, Martin Steinhart, and Markus Haase, "Cerium-Modified Mesoporous Antimony Doped Tin Oxide as Intercalation-Free Charge Storage Layers for Electrochromic Devices", *Advanced Functional Materials* **2022**, 4, 2210167

5.1 Introduction

The change in the optical properties of a material caused by reversible redox reactions is known as electrochromism, and materials showing this effect are used in a wide range of optoelectronic fields^[198,236–238]. Typical electrochromic devices comprise multiple components that have to meet several requirements to allow fast and efficient switching between the colored and decolored state. As for the materials that cause the change in optical absorption, the spectrum of suitable compounds spans a wide range of inorganic^[113,239,240], organic^[194,241,242], or hybrid materials^[243,244]. Since the coloration and decoloration of these materials are electrochemically induced, the charge required to oxidize or reduce the active compounds in the working electrode of the device must be compensated by storing a corresponding amount of charge in the counter electrode. Usually, the charge-storing material forms a layer on this electrode and is therefore referred to as a charge storage layer. Some key properties of electrochromic devices that should be met by both the active material and the charge balancing material are high transmission in the bleached state and fast electron transfer to achieve fast switching times^[245]. In particular with respect to the latter aspect, the capacity of the charge storage layer has to be sufficiently high.

Similar to the optically active compounds, the type of materials that can be used as charge storage layers is diverse. For example, organic molecules or polymers can be used, which not only provide the balancing charges but also contribute to the electrochromic contrast of the device^[209,246–248]. The inorganic Prussian blue^[249,250] or nickel oxide (NiO)^[251,252] also exhibit similar properties. Another widely used class of materials is based on compounds that provide the required charges through ion intercalation. These mainly include oxides such as tin dioxide (SnO₂)^[253,254], antimony doped tin oxide (SnO₂:Sb, ATO)^[224,255], or cerium dioxide (CeO₂)^[256,257]. Especially the latter is very interesting as it allows reversible switching of the Ce³⁺/Ce⁴⁺ redox couple while displaying no considerable absorption in the visible spectrum^[258]. Typically, the performance of charge storage layers of cerium dioxide can be improved by mixing with other oxide materials, e.g. TiO₂-CeO₂^[259], SnO₂-CeO₂^[260], ZrO₂-CeO₂^[261], or others^[262].

In the previous chapter it was demonstrated that the performance of mesoporous ATO electrodes, modified with a cathodically coloring viologen dye as the electrochromic compound, benefits from the use of electrolytes containing non-intercalating cations^[263]. Such systems, of course, also require a charge storage layer in which the charge storage mechanism does not depend on the intercalation of ions. For this purpose, the above-mentioned charge storage layers based on cerium oxide nanoparticle layers are not suitable since non-intercalating electrolytes only allow reactions at the outermost surface of the particles while the ions in the volume of the particles are not accessible. Thus, the thickness of the electrodes would have to be substantially increased to pro-

vide the required charge storage capacity. Another possibility is the use of organic redox active molecules. In the previous chapter, a triarylamine-based dye that was anchored to a mesoporous ATO layer was employed as a counter electrode for the ATO/viologen working electrode^[263]. While this combination can be operated with a non-intercalating electrolyte, it has also some drawbacks: 1) the electrode displays some weak absorption in the state supposed to be the "uncolored" state of the device^[226], and 2) the optical response of the device results from a combination of the dyes on both electrodes, which may be undesirable if the transmission profile of the main coloring compound should be undisturbed. A possible solution is the use of the optically passive CeO₂ as a charge storage material. However, to be compatible with the ATO/viologen system, the redox switching of the Ce³⁺/Ce⁴⁺ couple must occur in the presence of a non-intercalating electrolyte. Without intercalation, however, this switching can only be realized by a redox process taking place on the surface of the storage layer. Therefore, it is necessary to fabricate electrodes that provide a structure with a large surface area that can be decorated with a redox-active cerium compound. For this purpose, mesoporous layers of n-doped ATO nanoparticles are attractive as scaffolds since they exhibit high electrical conductivity over a wide potential range^[226,235]. The latter should help to induce the redox reactions of the cerium compound on the surface considering the high positive redox potential of the Ce³⁺/Ce⁴⁺ couple^[264,265]. Especially when small nanoparticles are used to form the scaffold, the resulting mesoporous layers provide a large internal surface area that can be modified and are still able to achieve fast switching times, regardless of the size of the non-intercalating cations in the electrolyte^[263].

Herein, the fabrication of mesoporous ATO electrodes and the deposition of a redox-active cerium compound on their surface by a simple immersion method is presented. Employing an electrolyte containing a non-intercalating cation, the spectroelectrochemical properties of these electrodes are evaluated. The number of cerium ions on the inner surface of the electrodes was varied by applying several surface modification cycles. In addition, the influence of the antimony doping concentration in the ATO nanoparticles on the charge storage capacity of the cerium-modified electrodes is investigated. Finally, a complete electrochromic device is constructed using the cerium-modified ATO electrode as a counter electrode, also in combination with the non-intercalating electrolyte. The performance of the device suggests that the cerium-modified electrodes are capable charge storage layers despite the absence of intercalation phenomena.

5.2 Experimental

Nanoparticle synthesis:

ATO nanoparticles were prepared by the procedure reported in section 4.2^[263]. In short, nanoparticles were synthesized in aqueous solution by adding hydrochloric acid to an alkaline precursor solution of potassium hexahydroxostannate and potassium hexahydroxoantimonate, resulting in precipitation. After centrifugation and washing steps, the nanoparticles were peptized by the addition of a base followed by an autoclave treatment and dialysis of the colloid. Finally, the particles were obtained as powder by removal of the solvent. Nanoparticles with antimony contents of 15%, 5%, 2%, and 0% were prepared by this procedure.

Preparation of mesoporous ATO layers:

Fluorine doped tin oxide coated glass (FTO, $\sim 7 \Omega \text{ sq}^{-1}$, Sigma Aldrich) was used as the substrate for the preparation of the electrodes and treated in a plasma cleaner (Diener Femto) prior to use. A nanoparticle paste was prepared by mixing 1 g of the nanoparticles with 8.5 g of water/methanol (1/1 by volume) resulting in a clear colloid. The viscosity of this colloidal solution was then strongly increased by dissolving 0.5 g hydroxypropylcellulose (Alfa Aesar). Nanoparticle/hydroxypropylcellulose layers were then prepared by doctor blading of the obtained paste. To obtain the mesoporous electrodes, the layers were heated to 450 °C at 5 °C min⁻¹ and held at 450 °C for one hour followed by natural cooling.

Decoration of ATO layers with Ce:

For modification of the mesoporous ATO layers with cerium species, the electrodes were immersed in an aqueous solution of 20 mM Ce(NO₃)₃ · 6H₂O (Fluka) and 60 mM 2-phosphonobutane-1,2,4-tricarboxylic acid (Bayer) at 80 °C for 20 min. The electrodes were then washed with water followed by calcination at 450 °C for 10 min. This surface modification procedure was conducted up to four times.

Spectroelectrochemical characterization:

Electrochemical experiments were carried out with a Gamry Interface 1000 potentiostat in a three-electrode setup with a platinum wire as the counter electrode and an Ag/AgCl reference electrode. A 1 M solution of tetrabutylammonium perchlorate (TBAP, Sigma Aldrich) in propylene carbonate (PC, Sigma Aldrich) served as electrolyte. Potential-dependent UV/VIS measurements were performed with an Avantes AvaSpec-3648 spectrometer and an Avantes AvaLight-DHc light source in an electrochemical cell with a cuvette attached.

Physical characterization:

The mesoporous ATO layers were characterized by scanning electron microscopy (SEM) with a Zeiss Auriga instrument using an acceleration voltage of 3 kV and an in-lens detector. An X-Max 80 mm² silicon drift detector (Oxford Instruments) was used to acquire energy dispersive X-ray (EDX) spectroscopy data. All samples were sputtered with iridium/platinum before use. For characterization of the crystallographic phases of the ceria-modified nanoparticles via X-ray powder diffraction (XRD), a Panalytical Empyrean diffractometer with Bragg-Brentano geometry, Cu K- α radiation, and a step size of 0.0016° was used.

Device Fabrication:

The device consisted of two mesoporous ATO layers, each deposited on FTO glass. In the case of the working electrode, the nanoparticles were doped with 2% Sb and the layers were modified with an electrochromic dye. This was achieved by immersing the electrodes into a 4 mM solution of 1-(4-cyanophenyl)-1'-(2-phosphonoethyl)-4,4'-bipyridin-1-ium in ethanol for 16 hours. For the counter electrode, the antimony doping level was 15% and the electrode was treated three times with the cerium solution as explained above. A 50 μ m gasket was used as a spacer and the device was filled with a 1 M solution of TBAP in PC as electrolyte.

5.3 Results and discussion

The ATO nanoparticles were synthesized from alkaline aqueous solutions of suitable tin and antimony precursors. The details of the synthesis as well as the physical characterization of the resulting ATO particles have already been described in section 4.2^[263]. For the initial experiments, an antimony doping concentration of 15% was used. These particles, with a size of approx. 3 nm, were re-dispersed into a water/methanol mixture to obtain a clear colloidal solution. After the addition of a polymer to increase the viscosity, the resulting paste was used to prepare the nanoparticle layers on fluorine-doped tin oxide (FTO) coated glass. Morphological characterization of the layers after calcination was carried out by scanning electron microscopy (SEM). The layers have a thickness of approx. 4.3 μ m (Figure 5.1a) and display a mesoporous structure as intended (Figure 5.1b). In the next step, the inner surface of the nanoparticle layers was modified with cerium. Figure 5.1c schematically displays the modification process. First, the mesoporous ATO electrodes were immersed in an aqueous solution containing cerium(III) nitrate and 2-phosphonobutane-1,2,4-tricarboxylic acid. The latter acts as a complexing agent for cerium ions and further contain a phosphonate group that is known to adsorb onto metal oxides^[266]. Thus, this process should account for a homo-

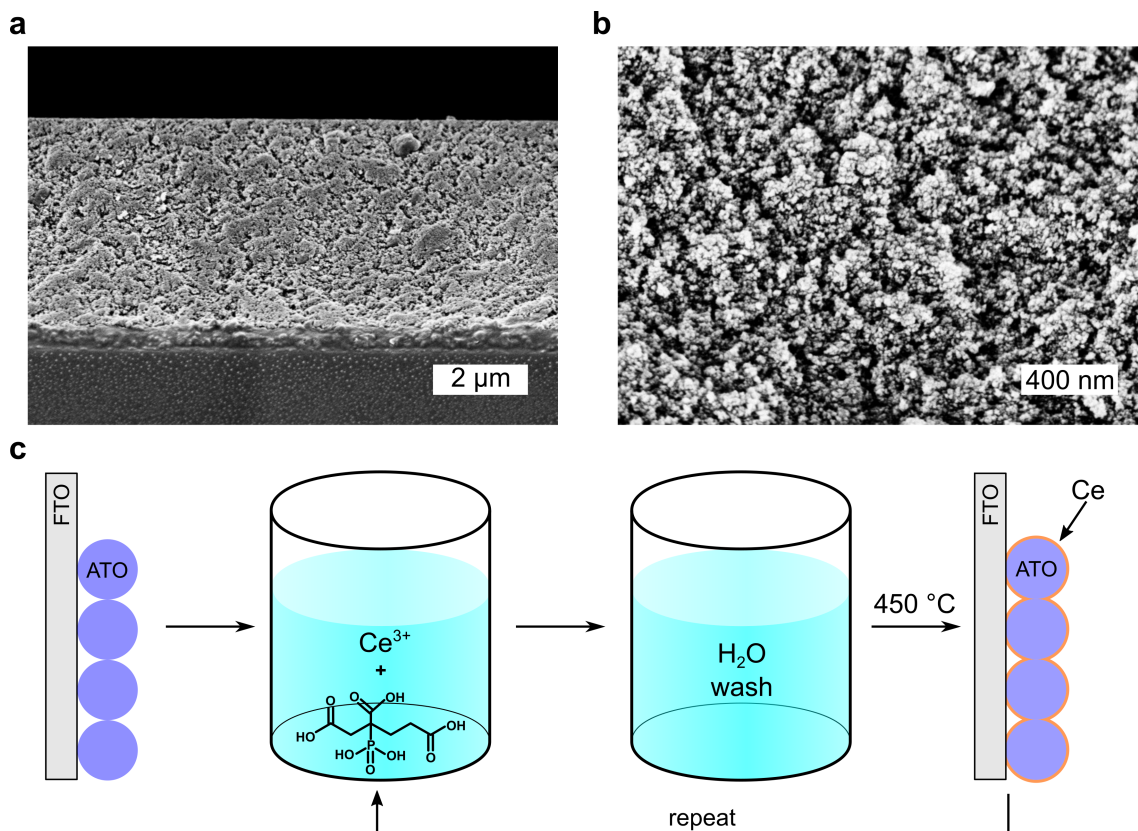


Figure 5.1: a) Cross-section SEM image of a mesoporous ATO layer on FTO glass. b) Magnified view of the SEM image displayed in a). c) Schematic representation of the process for the preparation of the Ce decorated mesoporous ATO layers.

geneous coating of the entire inner surface of the mesoporous nanoparticle structure. After a washing step, the electrodes were again shortly heated to 450 °C to remove the organic residue and ensure adhesion of the cerium species formed in this calcination step to the nanoparticle surface. Thus, an electrically conductive nanoparticle scaffold, the surface of which contains redox-active Ce^{3+/4+} species, is obtained. The whole process can be repeated to increase the number of cerium species within the mesoporous layers.

A major requirement of counter electrodes in electrochromic systems is their ability to store sufficient electric charge. Therefore, the electrochemical properties of the electrodes were evaluated. In all electrochemical measurements, the electrolyte consisted of 1 M tetrabutylammonium perchlorate (TBAP) dissolved in propylene carbonate (PC). A salt with a large cation was chosen to avoid intercalation processes, as repeated intercalation of ions is known to degrade the crystalline structure of ATO nanoparticles^[218]. Cyclic voltammograms (CV) of a bare ATO electrode and an electrode that went through one Ce modification cycle are shown in Figure 5.2a. The unmodified ATO electrode exhibits capacitive behavior that can be ascribed to electron injection into the nanoparticle conduction band at negative potentials and depletion of free electrons un-

Results and discussion

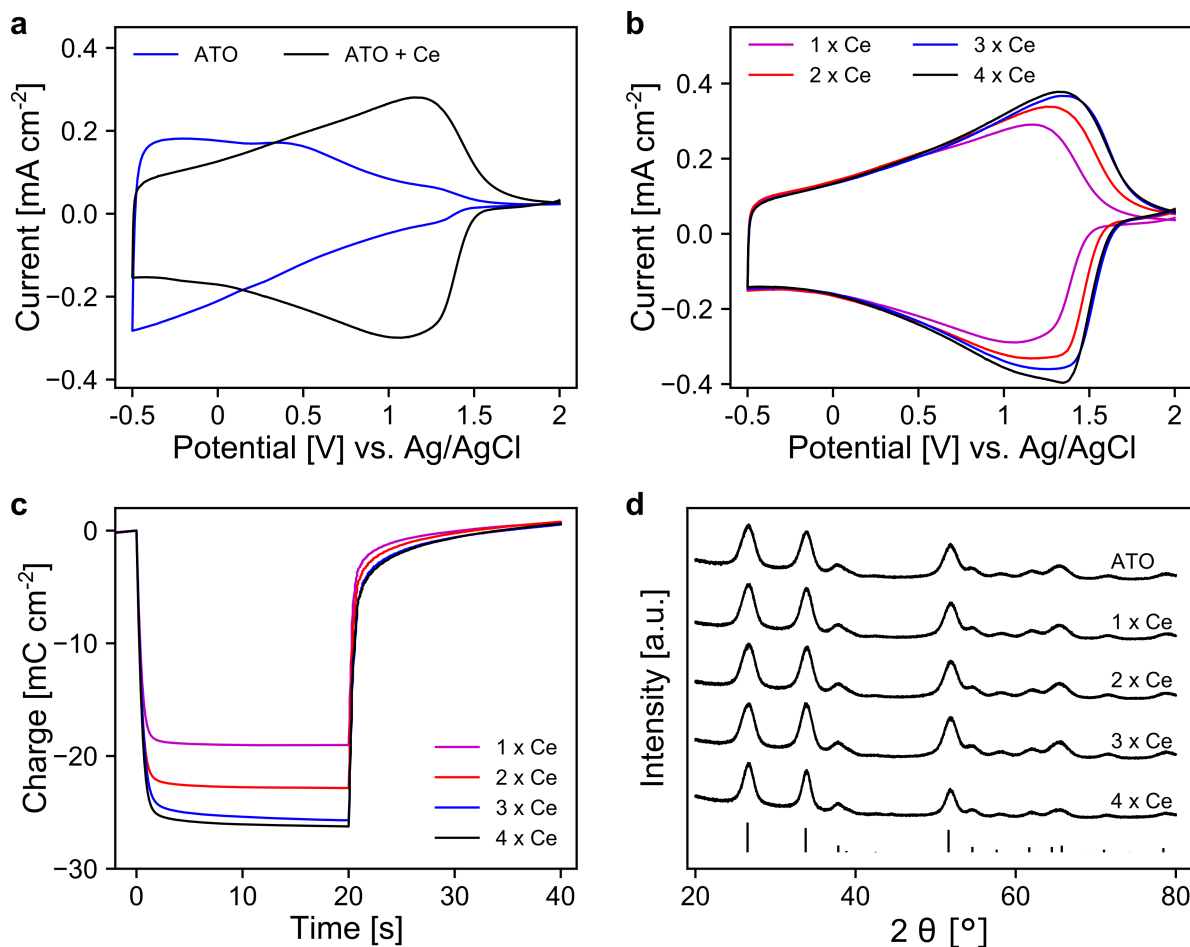


Figure 5.2: a) CV's of a bare mesoporous ATO electrode and an electrode modified once with Ce, measured at 20 mV s^{-1} . b) CV's of ATO electrodes modified from one up to four times with Ce, measured at 20 mV s^{-1} . c) Coulometry measurement for a potential step between 2 V and -0.5 V vs. Ag/AgCl from the ATO electrodes with different Ce modification cycles. d) XRD data of the ATO nanoparticles with and without Ce modification along with reference reflexes of SnO₂ (ICSD: 39177).

der positive polarization. Since the latter decreases the conductivity of the layer, the current increases from positive to negative potentials and vice versa. When a bare ATO electrode is immersed in a solution containing only the complexing agent but no cerium, the electrochemical response after calcination is almost identical to that of the bare ATO electrode (Figure 5.3). After surface modification with the complexing agent and cerium, however, the electrodes display a drastically different behavior: A potential sweep direction from negative to positive potentials now results in a steady increase rather than a decrease of current. The increase culminates in an almost peak-shaped feature in the CV after which the current drops drastically. Reversing the potential sweep direction yields the opposite effect, i.e., a steady decrease in current resulting in a final value that is lower than for the unmodified electrode. Obviously, the modification of the nanoparticle surface with cerium slightly reduces the number of electrons that can be injected

Results and discussion

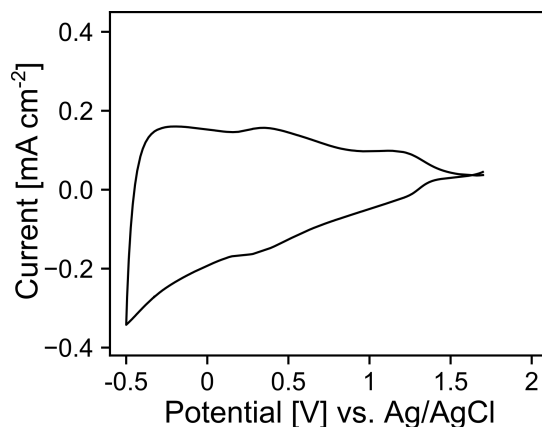


Figure 5.3: CV of a mesoporous ATO electrode that was immersed in a solution containing only the complexing agent, washed, and calcined at 450 °C. The measurement was performed with a scan rate of 20 mV s⁻¹.

into the ATO particles at negative potentials. The strong current flowing in the positive potential range, on the other hand, indicates successful and reversible oxidation and reduction of cerium ions contained in or on the surface layer of the ATO nanoparticles. Although it is not possible to directly verify the changes in the oxidation state of cerium by suitable in-situ measurements, it is clear that cerium must be the active component, since only in the presence of cerium (see also below) the above-mentioned changes in the electrochemical behavior are observed, but not for the unmodified electrodes or for electrodes treated only with the complexing agent. In total, the presence of cerium increases the charge storage capacity by a factor of 1.7 (from 11.4 to 19.4 mC cm⁻²) compared to the bare ATO electrode. Reaching a high value of 19.4 mC cm⁻² is impressive considering the use of a non-intercalating electrolyte. The high charge storage capacity is therefore solely based on the double layer capacity of the ATO scaffold at negative potentials and the redox switching of the cerium compound at positive potentials. Note that the charge storage capacity may, of course, be further varied by tuning the porosity of the layer or by changing its thickness. Herein, however, the focus lies on the effect of cerium on capacity. To potentially further increase the amount of charge stored in the layer, the ATO electrodes were subjected to multiple modification cycles to increase the cerium concentration on the surface. Corresponding CV measurements of electrodes with up to four modification cycles are presented in Figure 5.2b. The figure displays in fact a steady increase in current and a slight shift of the position of the maximum current for up to three modification cycles, while the characteristic overall response of the electrodes remains similar. It is further evident that four or more modification cycles do not significantly further increase the current. Therefore, it may be assumed that too high cerium concentrations result in the formation of small clusters on the surface and that the cerium ions in the core of these clusters are not accessi-

Results and discussion

ble for redox reactions anymore due to the non-intercalating cation in combination with the decreased conductivity of the nanoparticle scaffold at positive potentials. From the coulometric measurements displayed in Figure 5.2c, it is apparent that the maximum charge stored in the layer increases from 19.4 to 26.7 mC cm⁻² for one to three modification cycles. The fourth modification cycle increases the value only marginally to 27.6 mC cm⁻². Another noticeable feature is the shape of the coulometric response curve that implies fast charging and discharging of the layers, even in the three-electrode setup, as it is highly desired for their application in an electrochromic device.

The porous layers were further analyzed by energy dispersive X-ray spectroscopy (EDX). The results confirm that the modified ATO layers not only contain Sn and Sb but also Ce and P (Table 5.1). Furthermore, the amount of Ce and P increases with the number of modification cycles. In fact, the complexing agent chosen to bind cerium ions to the ATO surface contains a phosphonate group that cannot be removed by calcination in the air. The phosphorus content of the modified layers is therefore likely to be caused by phosphate groups formed by calcination of the cerium phosphonate complexes on the ATO surface. The cyclic voltammograms show that oxidation/reduction of cerium takes place over a large potential region indicating that different cerium species are present on the surface. Most likely, these species consist of different cerium phosphates with very small particle sizes. The latter can be deduced from X-ray powder diffraction (XRD) measurements of nanoparticle powders obtained by scratching the mesoporous layers from the substrate. Figure 5.2d shows that the XRD peaks of the samples can be assigned to the rutile phase of tin dioxide while no additional peaks of cerium compounds are present. This indicates that even after four modification cycles only very small clusters of cerium compounds are formed that are not detectable by XRD. Nevertheless, the amount of cerium on the surface is quite large: The EDX measurements yield molar fractions of cerium (cerium content with respect to the sum of the contents of Sn, Sb, and Ce) between 3.6% (one cycle) and 6% (four cycles). These high values suggest a more or less homogeneous coverage of the whole surface of the

Table 5.1: Elemental composition (in at.%) of Ce-modified ATO electrodes, determined by EDX analysis.

Sample	O	Sn	Sb	Ce	P
0 x Ce	56.5	37.2	6.3	-	-
1 x Ce	55.8	35.5	5.5	1.5	1.7
2 x Ce	56.9	34.8	4.3	1.9	2.2
3 x Ce	55.0	34.9	5.9	2.0	2.8
4 x Ce	56.0	33.9	4.7	2.5	2.9

ATO scaffold.

In addition to the increase in charge storage capacity, the cerium modification also influences the optical behavior of the mesoporous ATO layers, as shown by UV/VIS spectroscopy. Figure 5.4a displays the effect of calcination on the transmission spectra of ATO electrodes that were treated with the cerium precursor solution. Prior to calcination, the layer displays maximum transparency at approx. 450 nm. Toward higher wavelengths, the transparency decreases slightly due to the presence of free electrons within the ATO nanoparticles resulting in a strong plasmon absorption band in the NIR region^[230]. The short-wavelength tail of this band extends into the visible region resulting in a slight blue coloration of the layers. In the UV region, again also a decrease in transparency can be observed that is related to the bandgap of ATO. After calcination of the electrode, the transmission spectrum displays distinct differences. First,

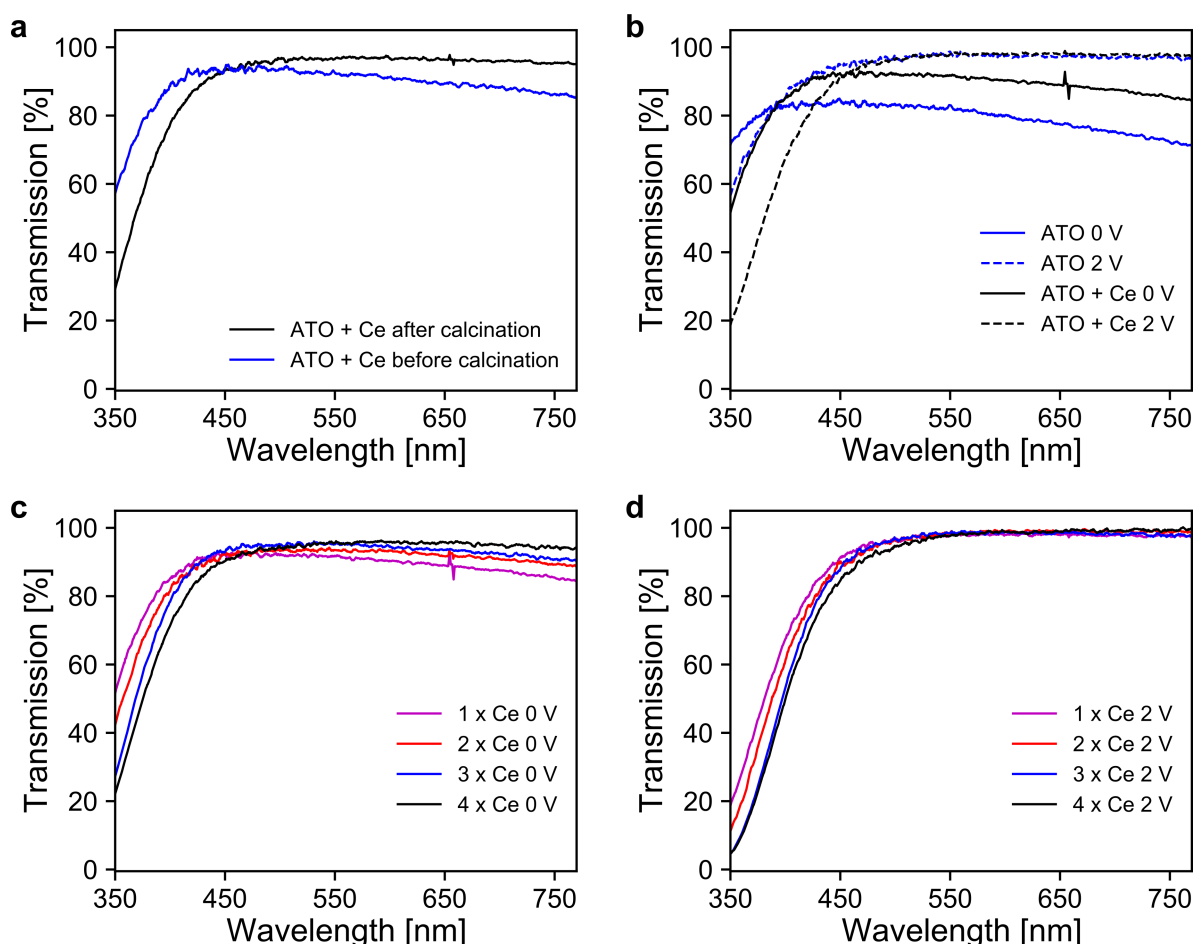


Figure 5.4: a) UV/VIS spectra of an ATO electrode modified once with Ce before and after calcination. b) UV/VIS spectra of an unmodified ATO electrode and electrode modified once with Ce under application of 0 V or 2 V vs. Ag/AgCl. c/d) UV/VIS spectra of ATO electrodes with different Ce modification cycles polarized at 0 V and 2 V, respectively. In all measurements, the electrolyte-filled electrochemical cell and a blank FTO glass were used as the optical reference.

Results and discussion

starting from approx. 500 nm, the transmission exhibits a stable plateau toward higher wavelengths. This indicates a depletion of free electrons within the ATO nanoparticles after the cerium complex was decomposed by the high-temperature treatment and the cerium ions of the resulting cerium compound are in direct contact with the particle surface. In fact, cerium is known to scavenge electrons at elevated temperatures and this property has been utilized in sensing applications^[267,268]. Similar behavior is also observed for bare ATO electrodes when the electrons are electrochemically removed from the nanoparticle layer by applying a positive potential^[230]. Second, the absorption onset in the UV region is shifted toward higher wavelengths. This shift gives the layers a typical slight yellow appearance. This additional absorption indicates the formation of Ce^{4+} by oxidation of Ce^{3+} during calcination in air since Ce^{4+} is known for its oxygen-to-cerium charge transfer transition in this region, causing, for instance, the pale yellow color of CeO_2 . Similar optical changes are observed when the layers are electrochemically oxidized or reduced. To show this, the transmission spectra of a bare ATO electrode and an electrode that ran through one cerium modification cycle (with calcination) were recorded under the application of two different potentials, 0 V and +2 V, as shown in Figure 5.4b. When a potential of 0 V is applied, the absorption at longer wavelengths is increased in both cases, as expected when additional electrons are injected into the layers. The increase of the absorption is less pronounced for the cerium-containing electrode, which is in accord with the CV result from above indicating that fewer electrons can be injected into the ATO layer when its surface is decorated with the cerium compound(s). In the absence of cerium, and, hence, the Ce^{4+} absorption band, the injection of additional electrons furthermore leads to the expected increased Burstein-Moss shift of the bandgap absorption. Figure 5.4b also shows that these effects are reversed by electrochemical oxidation of the layers: Polarization at +2 V results in an increase of transparency for both electrodes due to the depletion of the free electrons within the ATO nanoparticles. In the case of the Ce-modified electrode, the absorption in the UV and blue region increases as additional Ce^{3+} is oxidized to Ce^{4+} at this potential as it was already evident from the CV measurements discussed earlier. The average transmissions of the bare and Ce-modified ATO electrodes, between 380 and 780 nm, are 79.4% and 89%, respectively. As it will be shown later, this increase in transparency is unchanged during prolonged potential switching. This suggests a permanent change in the properties of the ATO nanoparticles after modification with Ce. Since multiple modification cycles lead to an increase in charge storage capacity, its influence on the optical properties was also investigated. The transmission spectra of Ce-modified ATO electrodes with one to four modification cycles being polarized at 0 V are displayed in Figure 5.4c. Here, increasing the number of modification cycles on the one hand leads to a slight increase in transparency at higher wavelengths. This

Results and discussion

can be again ascribed to the smaller number of electrons that can be injected into the nanoparticles. On the other hand, the absorption in the UV and blue region increases with the number of modification cycles. This is also expected as the amount of electrochemically inaccessible Ce^{4+} should increase proportionally to the amount of cerium in the layer. When polarized at 2 V, the electrodes become more intensively yellowish colored as oxidation of Ce^{3+} ions increases the number of Ce^{4+} ions (Figure 5.4d). Figure 5.4d also shows that a fourth modification cycle does not significantly alter the properties of the electrodes anymore, in accord with the CV measurements discussed earlier. The electrochemical and optical characterization of the cerium-modified ATO electrodes presented so far already indicates that these electrodes should be very attractive for electrochromic applications since they combine high transparency with high charge storage capacities even when non-intercalating electrolytes are used.

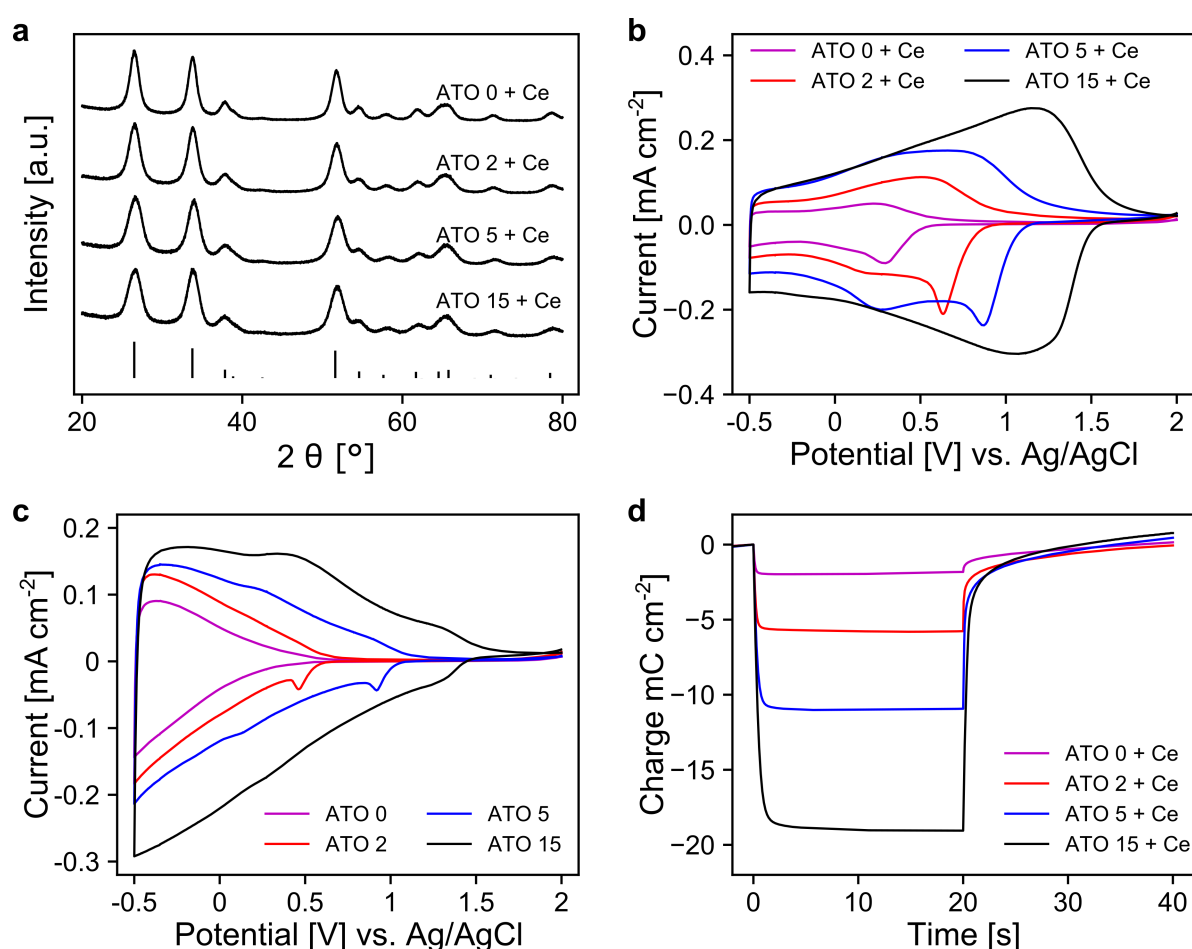


Figure 5.5: a) XRD data of ATO electrodes with different antimony contents after one Ce modification cycle along with reference reflexes of SnO₂ (ICSD: 39177). CV's of ATO electrodes with different antimony contents b) with and c) without Ce modification, measured at 20 mV s⁻¹. d) Coulometry measurements for a potential step between 2 V and -0.5 V vs. Ag/AgCl.

Results and discussion

In the experiments so far, an antimony doping concentration of 15% was used. It is well known that the antimony content has a great influence on the properties of ATO nanoparticles. Therefore, the electrochemical performance of Ce-modified electrodes of ATO nanoparticles with different antimony contents was investigated. In particular, Sb doping concentrations of 15% (ATO 15), 5% (ATO 5), 2% (ATO 2) and 0% (ATO 0) were used. With all of these nanoparticles, mesoporous layers were prepared and subjected to one cerium modification cycle. As shown in Figure 5.5a, the XRD data of all samples again only display the SnO₂ phase without any reflexes that can be assigned to a specific cerium compound. The electrochemical behavior of the cerium-modified electrodes was then evaluated by CV measurements (Figure 5.5b). As expected, the presence of cerium increases the current toward more positive potentials in all cases. However, the potential up to which a considerable current is flowing shifts systematically to lower values with decreasing antimony doping levels. The reason for this phenomenon can be deduced from Figure 5.5c, displaying CV measurements of the corresponding unmodified electrodes. Here also, the electrochemical response depends systematically on the antimony content: First, a higher antimony concentration increases the current at a given potential showing that more electrons are injected into the conduction band of the nanoparticles. Second, layers with higher antimony contents also carry more current toward positive potentials. This behavior has been related to the number of free electrons within the nanoparticles and the formation of a depletion zone at the particle surface when electrons are removed^[235]. The latter negatively impacts the conductivity of the layer but to a lesser extent when the Sb content is high. Therefore, the amount of cerium that can be oxidized seems to be limited by the intrinsic conductivity of the ATO nanoparticles at positive potentials. The figure also shows that Ce³⁺ ions in the layers can be oxidized over a wide range of potentials. This indicates that the redox potentials of the cerium ions are spread over a wide range and probably explains why the XRD data does not allow the identification of a well-defined cerium compound after calcination. A consequence of the reduced conductivity of the ATO nanoparticles at positive potentials is that less charge can be stored within such layers at low antimony doping concentrations. This is evident from the coulometric measurements displayed in Figure 5.5d. The values increase from 2.5 mC cm⁻² (0% Sb) over 5.5 mC cm⁻² (2% Sb), and 11 mC cm⁻² (5% Sb) to 19.4 mC cm⁻² (15% Sb) for one Ce modification cycle. Higher doping levels than 15% antimony, however, did not result in higher capacities anymore. From these experiments, it can be concluded that high antimony doping levels of up to 15% are beneficial for the preparation of electrodes with increased charge storage capacity. A remarkable advantage of the system presented here is the reduced standard disadvantage for such high doping levels, namely, reduced transparency of the electrodes. Despite the high doping level of 15%, the layers display high trans-

Results and discussion

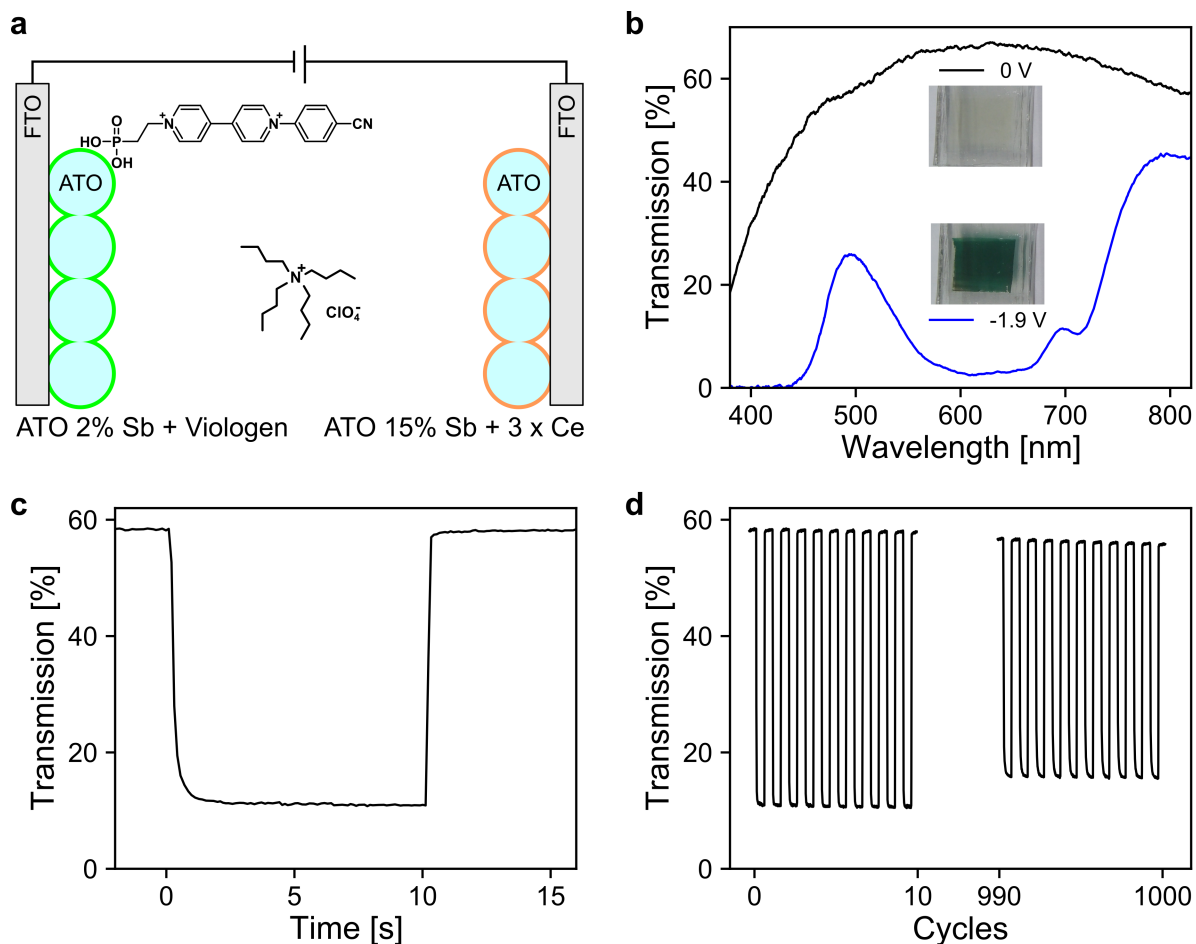


Figure 5.6: a) Schematic setup of the constructed electrochromic device. b) Transmission spectra in the colored (-1.9 V) and bleached state (0 V) along with corresponding images of the device. c) Time-resolved transmission change for one switching cycle. d) Transmission change of the device for 1000 switching cycles.

parency as shown in Figure 5.4. For applications requiring less charge to be stored, ATO nanoparticles with lower Sb contents may yield electrodes with even higher transmission. Alternatively, this could also be achieved with a high doping concentration but a reduced thickness of the mesoporous layer.

Finally, the Ce-modified ATO layers were implemented as counter electrodes in an actual electrochromic device. The schematic setup of the device is displayed in Figure 5.6a. As displayed in Figure 5.4, the cerium-modified electrodes provide high charge storing capability without significant modulation of their optical properties upon varying the potential. Considering the above results, nanoparticles with an antimony content of 15% were used for the Ce-modified counter electrode and applied three cycles of surface modification with cerium to provide a sufficiently high charge storage capacity. The 1 M solution of tetrabutylammonium perchlorate in propylene carbonate was also used as the electrolyte for the device. The second electrode, responsible for electrochromic coloration, also consisted of a mesoporous ATO scaffold. However, in this case, an

Results and discussion

antimony doping concentration of 2% was chosen since it accounts for a good compromise between electrical conductivity and optical transparency^[263]. This electrode was further modified with the redox-active electrochromic dye 1-(4-cyanophenyl)-1'-(2-phosphonoethyl)-4,4'-bipyridin-1-ium which was deposited via chemisorption. This dye colors upon electrochemical reduction while being transparent in the oxidized state. The performance of this dye in combination with a mesoporous ATO electrode with low antimony content and a non-intercalating electrolyte was already described in the previous chapter^[263]. Images of the device as well as the corresponding transmission spectra are shown in Figure 5.6b. In the transparent state, at 0 V, the device displays an average transmission of 58% between 380 and 780 nm. Application of a potential of -1.9 V induces reduction of the electrochromic dye that results in a change of the absorption behavior in form of coloration of the device. Thus, in the colored state, the average transmission of the device is reduced to approx. 11%, which accounts for an electrochromic contrast of 47%. Another important feature of an electrochromic device is its switching time. The time-resolved transmission change for one switching cycle is shown in Figure 5.6c. Reaching 90% of the electrochromic contrast takes 0.4 s to color the device and 0.3 s to reach the transparent state. These values confirm that the Ce-modified ATO films are very capable in terms of their charge storage capacity and fast electron transfer, even with electrolytes containing large cations. The long-term stability of such electrochromic devices is also of great importance. Therefore, the device was switched between 0 V and -1.9 V for 1000 cycles. For the first and last ten switching cycles, the corresponding transmission changes are displayed in Figure 5.6d. The results suggest that the device exhibits acceptable long-term performance as the device retains 85% of its initial electrochromic contrast. Further, the increased transparency of the Ce-modified ATO electrode seems to be a stable characteristic of these layers. Of course, further improving the long-term stability would be highly desirable when comparing the results to electrochromic systems with superior stability that have been reported in recent years^[269–271]. Note, however, that no efforts were made to optimize the sealing of the device or to keep the device in an inert atmosphere during the experiments. This could have a substantial influence on the performance of the device since contamination of the electrolyte with oxygen could lead to undesirable side reactions. Another degradation mechanism remaining may be the desorption of the electrochromic viologen dye. However, optimizing the device with respect to these aspects is beyond the scope of this work.

5.4 Conclusion

The inner surface of mesoporous ATO electrodes can be homogeneously decorated with redox-active cerium ions by immersing the layers in a solution of a suitable cerium complex that binds strongly to the ATO surface. After decomposition of the complex by a calcination step in air, these electrodes provide a higher charge storage capacity compared to unmodified ATO layers. Since a non-intercalating electrolyte was used, the overall charge storage capability is likely due to surface reactions that allow for fast electrochemical reaction times. The modified electrodes also exhibit improved optical properties due to increased transparency over the entire range of applied potentials. In addition, repeating the modification cycle up to three times results in an increase in capacity of up to 27 mC cm^{-2} . With respect to the antimony content of the nanoparticle scaffold, the capacity of the electrodes increases with increasing antimony doping concentration. The highest capacity is observed for ATO particles with 15% Sb. A complete electrochromic device consisting of a viologen-modified ATO electrode as the active layer and the cerium-modified ATO layer as the counter electrode exhibits a fast switching time of 0.4 s and acceptable long-term stability over 1000 switching cycles, resulting in only a 15% loss of electrochromic contrast.

6 Photo-electrochemical device enabling luminescence switching of LaPO₄:Ce,Tb nanoparticle layers

Cerium is an interesting element for electrochemical applications since it allows for reversible oxidation and reduction of the +3 and +4 states. In the previous chapter, the redox activity of cerium was utilized to store electric charges in an electrochromic device by decoration of mesoporous ATO layers with cerium species. However, there are also other materials containing Ce^{3+/4+} that may exhibit intriguing effects when the redox state of the cerium atoms is changed. With regard to this, LaPO₄ nanoparticles that are co-doped with Ce³⁺ and Tb³⁺ are of considerable interest. These nanoparticles are luminescent and emit green light when illuminated with UV light. A variety of groups have previously shown that chemically oxidizing Ce³⁺ atoms at the surface of the nanoparticles to Ce⁴⁺ quenches the luminescence. By chemically reducing the oxidized Ce⁴⁺, the luminescence is restored. If the nanoparticles are assembled into thin films, treating these layers in separate solutions of suitable oxidizing and reducing agents allows for a reversible on/off switching of the luminescence. In order to further explore this effect, achieving this through an electrochemical approach is highly intriguing. However, in contrast to ATO, thin films of LaPO₄:Ce,Tb nanoparticles are not electrically conducting. Therefore, electrons cannot be simply transferred through the nanoparticle network to induce redox reactions. Overcoming this limitation is the subject of the current chapter.

Parts of this chapter were published:

Jonas Klein, Seyyed Mohsen Beladi-Mousavi, Marco Schleutker, Dereje Hailu Taffa, Markus Haase, and Lorenz Walder, "Photo-Electrochemical Device Enabling Luminescence Switching of LaPO₄:Ce,Tb Nanoparticle Layers", *Advanced Optical Materials* **2021**, 9, 2001891

6.1 Introduction

Microcrystalline $\text{LaPO}_4:\text{Ce},\text{Tb}$ powder has been widely used as green emitting phosphor in fluorescent lamps due to its high luminescence quantum yield and chemical stability^[272–276]. The luminescence is based on the UV excitation of Ce^{3+} followed by $\text{Ce}^{3+} \rightarrow \text{Tb}^{3+}$ energy transfer and finally Tb^{3+} emission^[277]. Further, generation of Ce^{4+} within these particles is known to efficiently quench the luminescence due to fast energy transfer via adjacent Ce^{3+} ions, followed by quenching at the Ce^{4+} ions^[278]. Thus, the luminescence can be switched on and off by partially changing the oxidation state of cerium species at the particle surface making them an attractive material for sensing applications^[279–282]. In the chemical version of this switching, potassium permanganate is commonly used to oxidize Ce^{3+} and quench its luminescence while ascorbic acid is used to restore the luminescence of Ce^{3+} by reducing the Ce^{4+} ^[60,283–286]. In the work presented here, an electrochemical approach towards repetitive luminescence on/off switching of thin $\text{LaPO}_4:\text{Ce},\text{Tb}$ films is investigated. Microcrystalline $\text{LaPO}_4:\text{Ce},\text{Tb}$ powder has a luminescence quantum yield in the visible range of 86%. The quantum yield of the $\text{LaPO}_4:\text{Ce},\text{Tb}$ nanoparticles used here is 43%^[274]. Adding an undoped LaPO_4 shell to the $\text{LaPO}_4:\text{Ce},\text{Tb}$ nanoparticles would increase the luminescence quantum yield to 70% but would inhibit switching of their luminescence. Since the nanoparticles are electronically insulating a conductive additive such as carbon black would be needed, but such strongly absorbing species would negatively affect the luminescence of the electrode. To avoid this problem, small organic molecules are utilized as redox shuttles to mediate electron transfer between the $\text{LaPO}_4:\text{Ce},\text{Tb}$ nanoparticles and the current collector. Redox shuttles are commonly used as enhancing additives in fields such as biotechnology^[287,288], photocatalysis^[289–291], or batteries^[292–295]. The redox shuttles are added to the electrolyte and diffuse throughout the nanoporous nanoparticle film enabling repetitive luminescence on/off switching based on the applied potential.

6.2 Experimental

Nanoparticle Synthesis:

For the synthesis of $\text{La}_{0.4}\text{PO}_4:\text{Ce}_{0.45},\text{Tb}_{0.15}$ nanoparticles, $\text{LaCl}_3 \cdot 7\text{H}_2\text{O}$ (1.49 g, 4 mmol), $\text{CeCl}_3 \cdot 7\text{H}_2\text{O}$ (1.68 g, 4.5 mmol), and $\text{TbCl}_3 \cdot 6\text{H}_2\text{O}$ (0.56 g, 1.5 mmol) were dissolved in 10 mL methanol. To the clear solution, diethylethylphosphonate (5.35 mL, 33 mmol) and diphenylether (30 mL) were added before the methanol was removed on a rotary evaporator. After heating the solution to 105 °C under vacuum, tributylamine (9.54 mL, 40 mmol) and a solution of phosphoric acid in dihexylether (2 m, 6.4 mL) was added at room temperature under nitrogen and then the mixture was heated to 200 °C for 16 h under nitrogen. The precipitate was centrifuged, washed with chloroform and dispersed

Experimental

in 300 mL methanol. After purification by diafiltration (5 kD membrane, 3 × 300 mL methanol), the nanoparticles were obtained as colloid in approx. 30 mL methanol. The nanoparticles were characterized by powder XRD on a Panalytical Empyrean diffractometer using Bragg-Brentano geometry, Cu K- α radiation and a step size of 0.039° 2 θ . Malvern Zetasizer Nano ZSP Dynamic light scattering (DLS) measurements were carried out on a Malvern Zetasizer Nano ZSP. LaPO₄:Eu nanoparticles were similarly synthesized starting with LaCl₃ · 7H₂O (3.342 g, 9 mmol) and EuCl₃ · 6H₂O (0.366 g, 1 mmol).

Film Preparation:

Nanoparticle films were prepared on ITO coated glass, which was cleaned by subsequent ultrasonication in mucasol, water and acetone. Pluronic F127 (12 600 g mol⁻¹, molar nanoparticle/polymer ratio 1/0.005) was added to 1 mL of the methanolic nanoparticle solution (0.16 M). 15 μ L of this mixture was drop casted onto the ITO substrate (1 cm² coated area) followed by heating the electrodes to 200 °C for 30 min. TGA of the composite and its individual components were performed on a NETZSCH STA 449 system with helium atmosphere.

Electrochemistry:

Electrochemical measurements were performed in a three electrode system with an Ag/AgCl reference electrode and a platinum wire counter electrode. A 0.1 M solution of LiClO₄ in acetonitrile served as electrolyte. Redox shuttles (structures shown in Figure A2, Appendix) were added to the electrolyte to a concentration of 1 mM (separate solutions). To perform electrochemical reduction of Ce⁴⁺ species, the nanoparticle films were chemically oxidized by immersion of the electrodes into an aqueous solution of KMnO₄ (1 mM) prior to electrochemical measurements. Cyclic voltammograms of the nanoparticle films in the electrolytes containing different redox shuttles were recorded with an Autolab PGSTAT 20 potentiostat. After the measurements, the electrodes were removed from the electrochemical cell and the success of the electrochemical luminescence switching was qualitatively checked under a UV light (254 nm).

Device Fabrication:

On a 2.5 × 3 cm ITO glass, a nanoparticle film (1 × 1 cm) was prepared based on the above described method with a fourfold diluted solution. A 2.5 × 3 cm carbon plate with a 0.5 × 0.5 cm cavity (overlapping with the nanoparticle film) was used as counter electrode and separated from the ITO glass by a 50 μ m gasket. A 2.5 × 2.5 cm quartz glass was placed on top of the carbon plate to close the device and allow entrance of UV light into the cell. Via vacuum backfilling, the device was filled with a 0.15 M solution of

Results and discussion

LiClO_4 in acetonitrile containing the redox shuttles 1,4-di-*t*-butyl-2,5-dimethoxybenzene (2 mM) and 7,8-dihydro-6H-dipyrido[1,2-*a*:2',1'-*c*]-[1,4]diazepinium (0.25 mM). The device was switched between 2 V and -1 V in 1 s intervals. A second device was built identically but the nanoparticle layer was prepared from a combined solution consisting of 95% of a methanolic solution (0.16 M) of 4 nm $\text{LaPO}_4\text{:Eu}$ particles and 5% of a methanolic solution (0.16 M) of 4 nm $\text{LaPO}_4\text{:Ce,Tb}$ particles. Pluronic F127 was added as described above. 30 μL of this undiluted mixture were drop casted onto the ITO (1 cm^2 coated area). Here too, potentials of -1 V and +2 V were applied but not in 1 s intervals.

6.3 Results and discussion

To realize the electrochemical luminescence switching, an electrochemical device was constructed, consisting of an electrode layer of $\text{LaPO}_4\text{:Ce,Tb}$ nanocrystals, an elec-

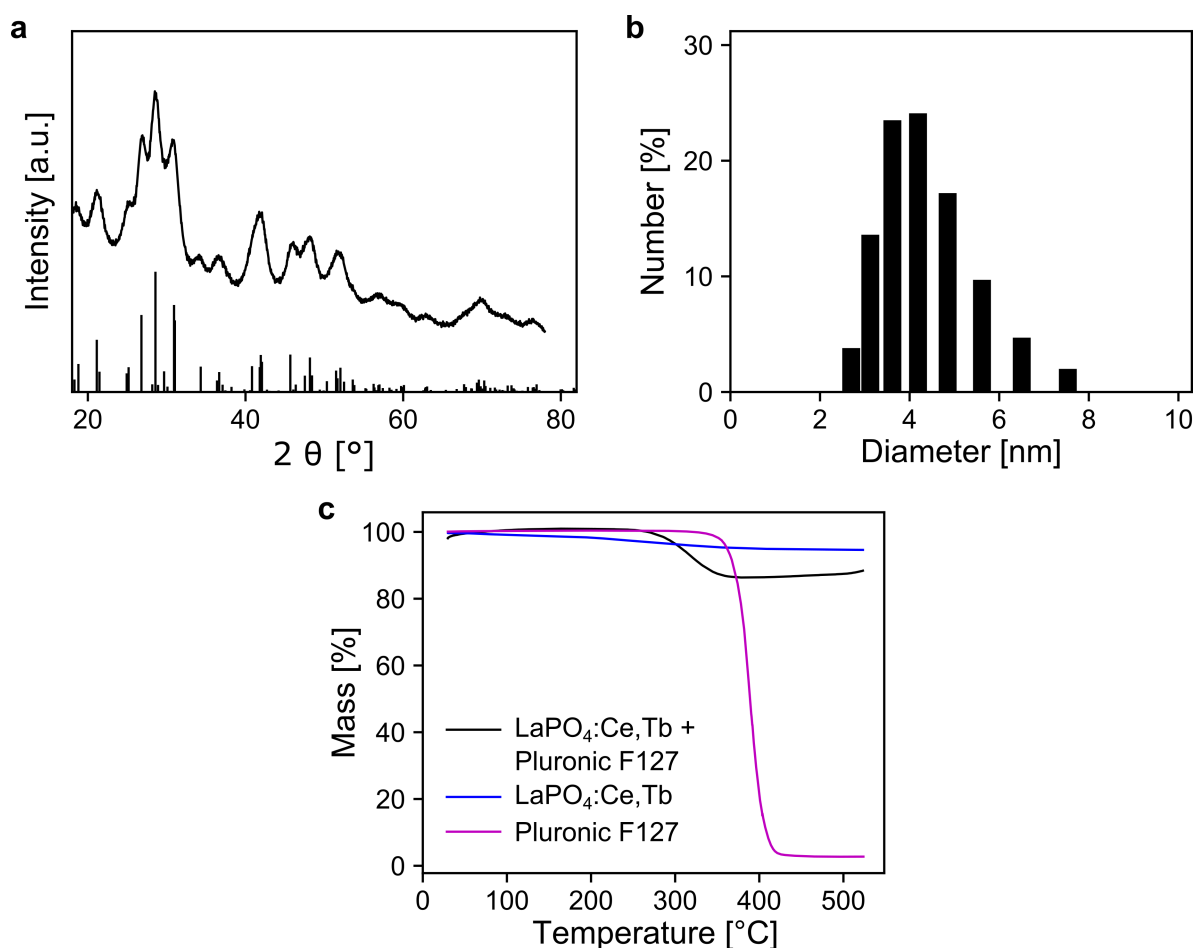


Figure 6.1: a) XRD spectrum of synthesized $\text{La}_{0.4}\text{PO}_4\text{:Ce}_{0.45},\text{Tb}_{0.15}$ nanoparticles and reference for monoclinic LaPO_4 (PDF 01-083-0651). b) DLS of a colloidal $\text{LaPO}_4\text{:Ce,Tb}$ solution. c) Thermogravimetric analysis of the $\text{LaPO}_4\text{:Ce,Tb/Pluronic F127}$ composite and its individual components.

Results and discussion

trolyte and a counter electrode. The $\text{LaPO}_4:\text{Ce},\text{Tb}$ layer was prepared from a colloidal solution of $\text{La}_{0.4}\text{PO}_4:\text{Ce}_{0.45},\text{Tb}_{0.15}$ nanoparticles with an average size of 4 nm, as confirmed by dynamic light scattering (DLS, Figure 6.1b), and spherical shape. The nanoparticles, which were synthesized via an already published procedure^[276], crystallized in the monoclinic structure as confirmed by powder X-ray diffraction (XRD, Figure 6.1a). The nanoparticle thin films were prepared from a mixture of this colloidal solution and a small amount of Pluronic F127 polymer, which was drop casted onto indium tin oxide (ITO) coated glass, followed by heating the electrodes to 200 °C. Addition of the polymer improved film homogeneity and prevented cracking of the layer. While heat treatment ensures adhesion of the film during electrochemical measurements, the temperature of 200 °C is not enough to remove the polymer from the film as shown by thermogravimetric analysis (TGA) of the composite (Figure 6.1c). Due to the nonconducting properties of the nanoparticle films, electrochemical oxidation of Ce^{3+} species through polarization of the electrodes at up to 2 V versus Ag/AgCl in 0.1 M LiClO_4 in acetonitrile could not be achieved. To enable redox reactions of the cerium atoms, redox shuttles were added to the electrolyte to transfer electrons between the current collector and the nanoparticles. As shown in Figure 6.2a the films are nanoporous in the sense that the redox shuttles are able to percolate the film composed of the nanoparticles embedded in a polymer matrix. For the electrochemical oxidation of Ce^{3+} species, redox shuttles are oxidized at the current collector followed by migration into the nanoparticle film. If the redox potential of the redox shuttle (E_S^0) is more positive than the redox potential of

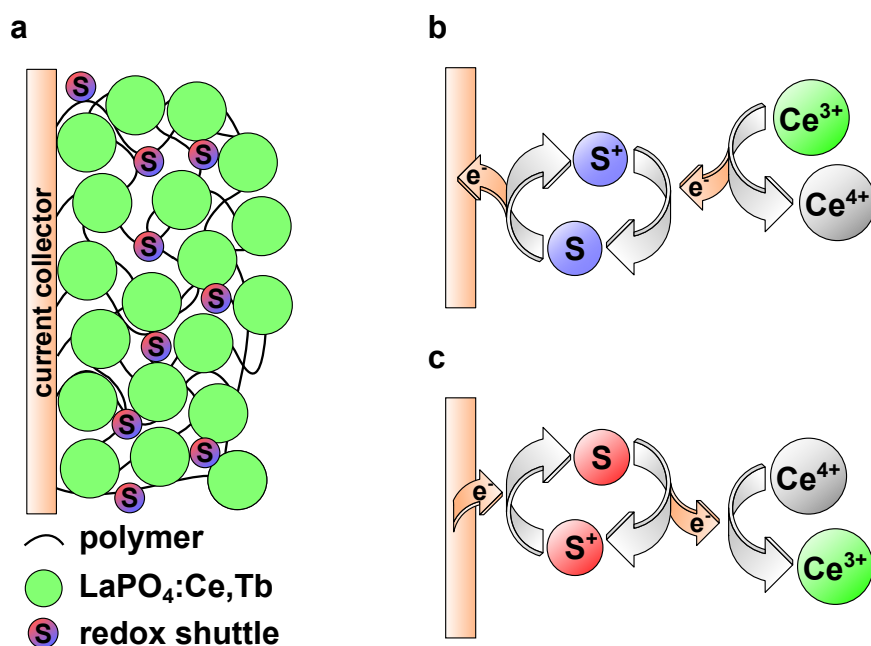


Figure 6.2: Schematic representation of a) nanoparticle/polymer composite thin film with percolating redox shuttles. Redox shuttle assisted electron transfer mechanism for b) oxidation of Ce^{3+} and c) reduction of Ce^{4+} .

Results and discussion

the $\text{Ce}^{3+/4+}$ couple (E_{NP}^0), electrons are transferred from Ce^{3+} ions of the $\text{LaPO}_4:\text{Ce},\text{Tb}$ nanoparticles to the oxidized redox shuttles. Thus, Ce^{4+} species are generated while the previously oxidized redox shuttles are reduced to their initial state and therefore can again undergo oxidation at the current collector, yielding a so called catalytic current. This mechanism is schematically shown in Figure 6.2b. In cyclic voltammetry (CV) measurements (three electrode setup), this electron transfer mechanism results in an increased oxidation current in the first cycle as shown in Figure 6.3a. Accordingly, the luminescence of the nanoparticle film is fully quenched. The electrochemical reduction of Ce^{4+} species follows the same principle when an electrochemically reducible

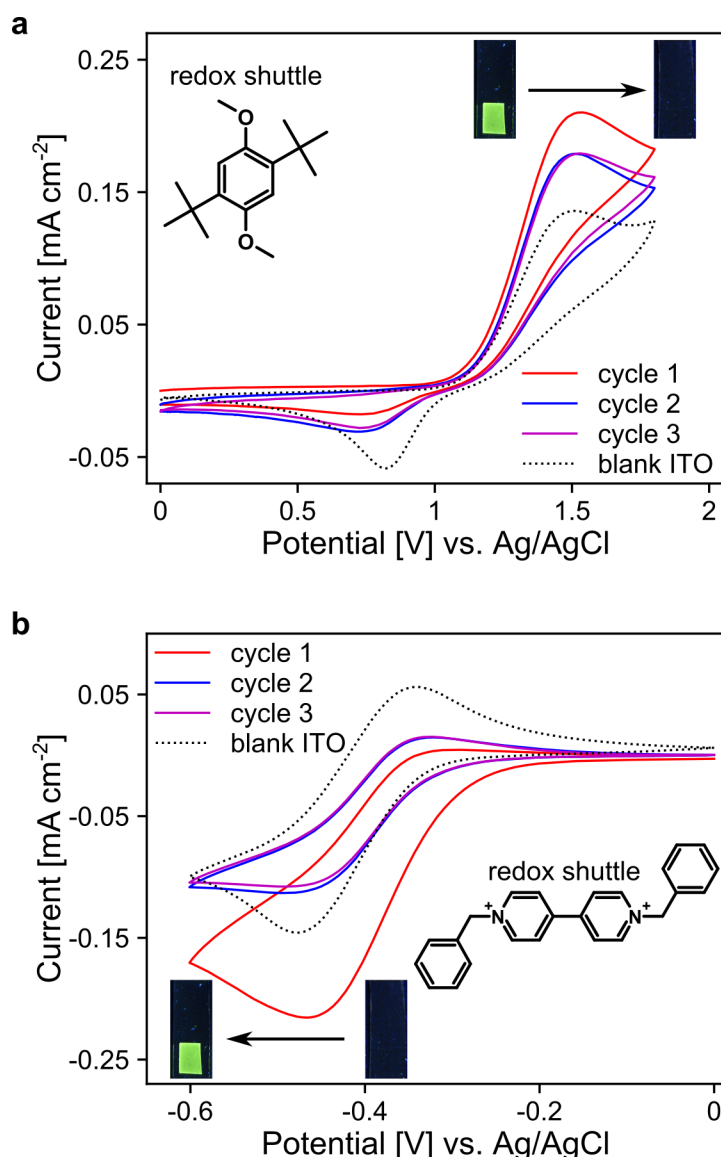


Figure 6.3: CV's of $\text{LaPO}_4:\text{Ce},\text{Tb}$ thin films on ITO for a) oxidation of Ce^{3+} (redox shuttle: 1,4-di-t-butyl-2,5-dimethoxybenzene, 50 mV s^{-1}) and b) reduction of Ce^{4+} (redox shuttle: dibenzylviologen, 20 mV s^{-1}) in 0.1 M LiClO_4 in acetonitrile, dotted line: on bare ITO, along with images of films under UV light before and after measurements.

Results and discussion

redox shuttle is used (Figure 6.2c). Here E_S^0 has to be more negative than E_{NP}^0 . In this case, an increased reduction current is observed in the first cycle of CV measurements (Figure 6.3b), leading to complete restoration of the luminescence.

Further CV's where such kind of catalytic currents were observed are shown in Figure A1 (Appendix). The excess charge between the first and second cycle along with the amount of nanoparticles present in the film allows calculation of the quantity of oxidizable/reducible $Ce^{3+/4+}$ to approx. 2.2%. Another important quantity is the formal redox potential of cerium species at the surface of $LaPO_4:Ce,Tb$ nanoparticles, especially since the redox potential of cerium is known to be strongly influenced by its chemical environment. Therefore, the capability to electrochemically oxidize Ce^{3+} was investigated for redox shuttles with different E_S^0 (molecular structures are shown in Figure A2, Appendix). This variation of E_S^0 shows that E_{NP}^0 has a value between 0.89 V and 1.15 V vs. Ag/AgCl (Figure 6.4 and Table A2, Appendix). Prior to these measurements, the redox potentials E_S^0 of the redox shuttles were determined from CV measurements using a blank ITO working electrode. Repetitive electrochemical oxidation and reduction can now be achieved with two redox shuttles present in the electrolyte, one that oxidizes Ce^{3+} and one that reduces Ce^{4+} .

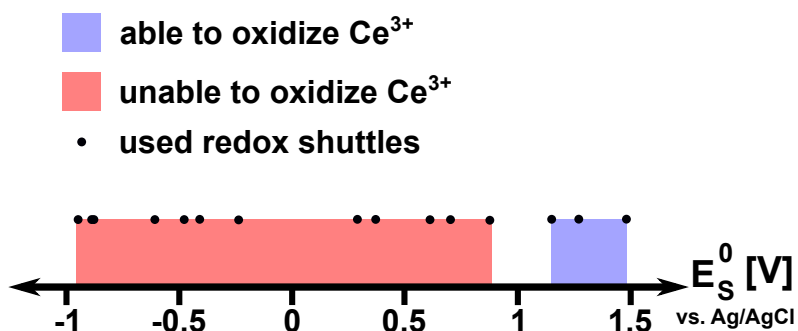


Figure 6.4: Redox potential dependent capability of redox shuttles to electrochemically oxidize Ce^{3+} in $LaPO_4:Ce,Tb$ nanoparticles.

In the experiments mentioned so far, the nanoparticle films had to be removed from the electrochemical cell after the measurements to check the luminescence under the UV light. To realize an in situ observation of the repetitive luminescence switching of the nanoparticles, a full thin-film electrochemical device was built consisting of the nanoparticle/polymer composite layer on ITO coated glass, a separator, the counter electrode and a quartz glass window (Figure 6.5a). For UV excitation of the composite layer, a UV transmitting electrolyte/redox shuttle combination had to be used. A 0.15 M solution of $LiClO_4$ in acetonitrile containing 1,4-di-*t*-butyl-2,5-dimethoxybenzene (2 mM) as oxidizing redox shuttle and 7,8-dihydro-6H-dipyrido[1,2-*a*:2',1'-*c*]-[1,4]diazepinium (0.25 mM) as reducing redox shuttle fulfills this requirement, at least for short path ways. Potentials of 2 V for oxidation and -1 V for reduction were repeatedly applied in intervals of 1

Results and discussion

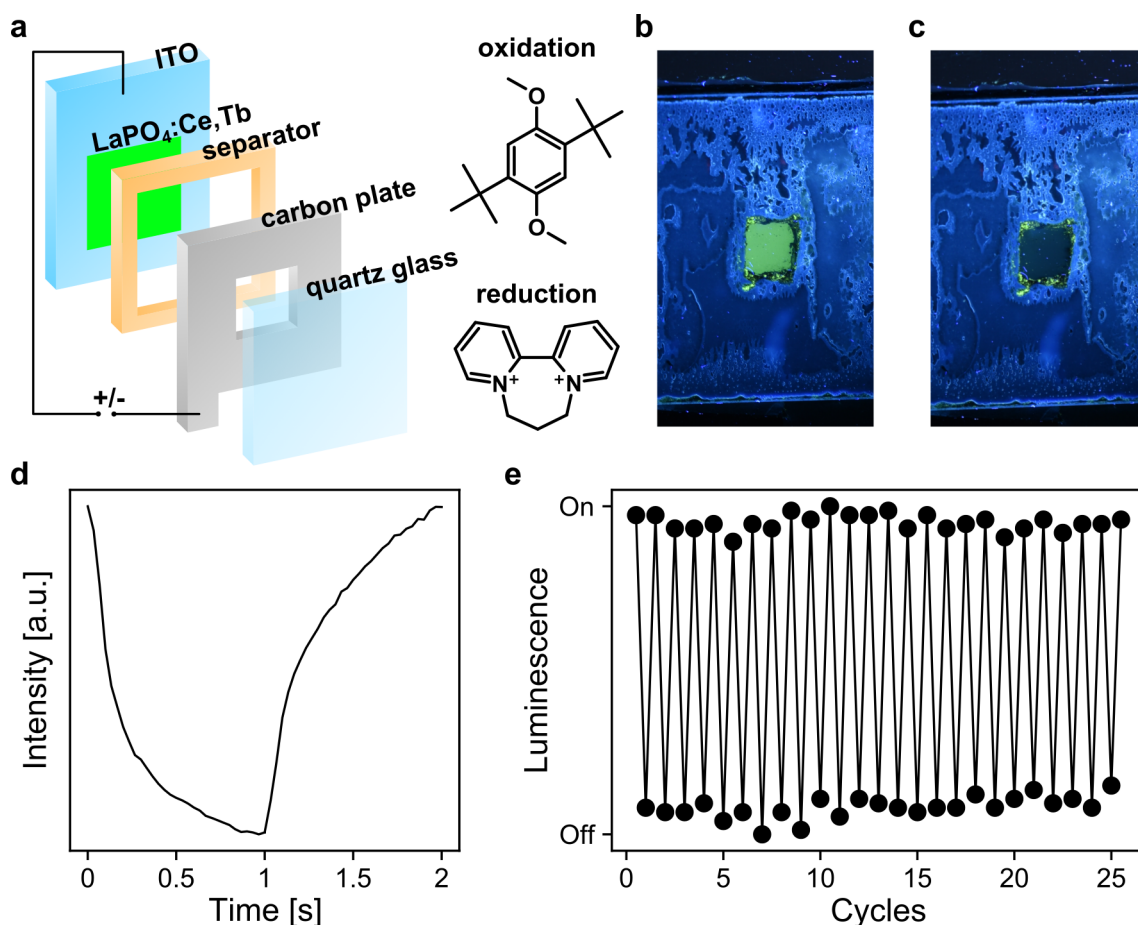


Figure 6.5: a) Schematic setup of the constructed device and chemical structure of the used redox shuttles for oxidation and reduction. Images of the device at b) -1 V (“on” state) and c) 2 V (“off” state). d) Time-resolved intensity change for one switching cycle. e) Luminescence state as a function of cycle number for repetitive switching.

s while UV light was cast through the quartz glass onto the nanoparticle film. Images of the device in the on/off state are displayed in Figure 6.5b,c. A movie showing the switching was recorded from which the intensity change of the nanoparticle film was monitored as a function of time using ImageJ software. Repetitive quenching and restoration of the luminescence was achieved for multiple switching cycles (Figure 6.5e). From the time resolved intensity change over one switching cycle, displayed in Figure 6.5d, the switching times to achieve a 90% change in intensity can be estimated as approx. 550 ms for quenching and approx. 650 ms for restoration of the luminescence. The fast switching times and the complete quenching of the luminescence indicate that the mediators are able to rapidly access most LaPO₄:Ce,Tb nanocrystals of the layer. In fact, switching remains possible even when the layer of LaPO₄:Ce,Tb particles is diluted with an inert solid nanomaterial. Here, LaPO₄:Eu nanocrystals are used since this material cannot be oxidized or reduced within the used potential range. In the diluted device, the nanoparticle layer consisted of a 1:19 mixture of LaPO₄:Ce,Tb and LaPO₄:Eu par-

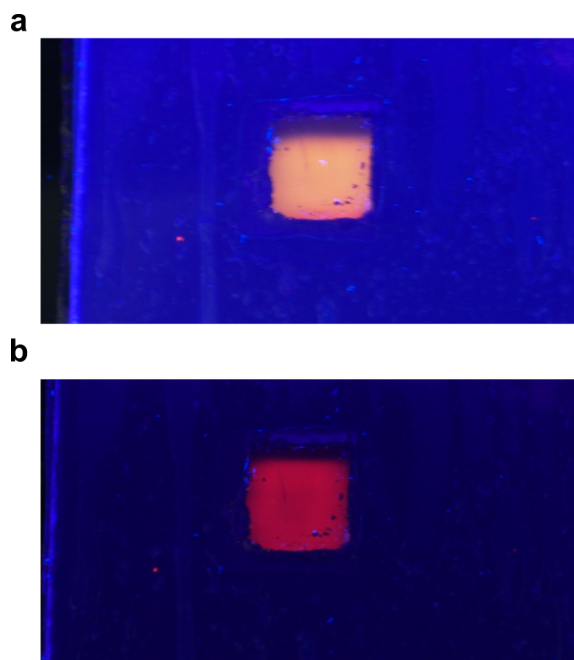


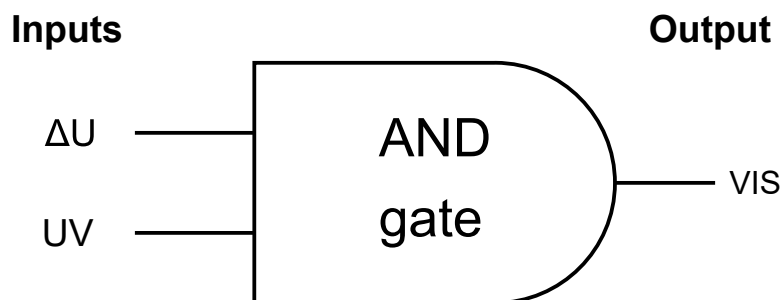
Figure 6.6: Images of a device with a mixed nanoparticle layer of $\text{LaPO}_4\text{:Ce,Tb}$ and $\text{LaPO}_4\text{:Eu}$ at a) -1 V and b) 2 V.

ticles of which the latter alone shows a red color under UV excitation. The device therefore displays a yellow color in the reduced state (-1 V) and red color when cerium species are oxidized ($+2$ V) and shows that not only on/off-switching but also switching between two different emission colors is possible (see Figure 6.6). Furthermore, this indicates that even in this diluted system, with respect to $\text{LaPO}_4\text{:Ce,Tb}$, the redox shuttles reach all nanoparticles within the layer and electrons are not transferred via adjacent $\text{LaPO}_4\text{:Ce,Tb}$ particles. With the applied voltage and UV light as inputs and visible light as output the device based on $\text{LaPO}_4\text{:Ce,Tb}$ represents a logical AND gate (Figure 6.7). The results also show that neither high temperature sintering processes nor the addition of solid conductive additives are required to utilize the redox-dependent optical properties of nonconductive nanoparticles in an electrochemical device. The redox shuttle-based working principle of the device may therefore enable the use of a large variety of different functional materials in opto-electrochemical devices.

6.4 Conclusion

In summary, the electrochemical luminescence switching of $\text{LaPO}_4\text{:Ce,Tb}$ nanoparticle thin films is demonstrated by a mediated electron transfer mechanism via small organic molecules (redox shuttles) present in the electrolyte. The formal redox potential of the $\text{Ce}^{3+/4+}$ species within the nanoparticles was determined within a narrow range by using redox shuttles with different redox potentials. Construction of a device containing

Conclusion



Inputs		Output
Negative potential (-1 V)	UV - light	Emission
on	on	on
off	on	off
on	off	off
off	off	off

Figure 6.7: Schematic representation of the electrochemical device with a $\text{LaPO}_4:\text{Ce},\text{Tb}$ layer as AND gate. “Emission on” means green color and “emission off” means no color.

an oxidizing and a reducing redox shuttle allowed in situ observation of repetitive luminescence on/off switching.

7 Summary

In the present thesis, two types of functional nanoparticles were investigated with respect to their thin-film application in electrochemical devices.

The first kind of particles were n-conductive antimony doped tin oxide (ATO, $\text{SnO}_2:\text{Sb}$) nanocrystals. ATO particles with a size of approx. 3-4 nm are accessible by precipitation of alkaline hexahydroxostannate and hexahydroxoantimonate precursor solutions through the addition of acids. The advantage of this method is the utilization of a pure Sb^{5+} source, which is beneficial for the properties of the nanoparticles. As-prepared nanoparticles obtained by this route, however, do not inherit the desired n-conductive properties as oxygen species (presumably O^{2-} or OH^-) rather than free electrons compensate for the excess charge of Sb^{5+} . Thus, the undesired oxygen species have to be removed from the nanocrystalline particles. Partially, this can be achieved by heating a colloidal solution of the synthesized particles in an autoclave. After this step, the initially colorless colloid is colored blue since the generated free electrons in the nanoparticles absorb light in the IR region. This effect, or more precisely, the plasmon absorption, increases when the nanoparticles are calcined. However, the nanoparticles cannot be re-dispersed into colloids if large aggregates are formed during calcination. Suppression of nanoparticle aggregation requires sufficient spatial separation of the nanoparticles during the heating process. Nanoparticle aerogels provide a highly porous solid structure that does not collapse during calcination and in which the nanoparticles have significantly reduced contact with each other. Thus, the internal structure of an aerogel restricts aggregation of the nanoparticles to the extent that the network structure can be broken and the nanoparticles can be re-dispersed after calcination. For example, ATO particles with a size of 5 nm show a hydrodynamic diameter of only 24 nm in water after calcination at 500 °C. Comparable results were also achieved with titanium dioxide (TiO_2) nanoparticles, and therefore, the presented aerogel route might very well be applicable to obtain colloidal solutions of a variety of calcined functional materials.

The colloidal solutions of nanoparticles after the autoclave treatment present an ideal basis for the preparation of nanoparticle pastes. These can be used for the preparation of mesoporous ATO layers on conductive substrates for application in electrochemistry, particularly for electrochromic devices in which organic dye molecules are anchored to the inner surface of the mesoporous films. Common representatives of such dyes are viologens, which are colored in their reduced state and transparent in their oxidized state. Thus, they require the application of negative potentials to induce the reduction. Depending on the electrolyte composition, this can have undesirable side effects, with

Summary

the main problem being ion intercalation into the nanoparticles of the mesoporous film, resulting in potential performance degradation due to mechanical stress. A comparison of the electrochemical properties of ATO and TiO₂ layers reveals that ATO offers higher electrical conductivity over a much broader potential range. Furthermore, the electrical conductivity of ATO with a non-intercalating electrolyte is nearly as high as with a standard electrolyte containing lithium. Even with a non-intercalating electrolyte, viologen molecules anchored to mesoporous ATO layers display fully reversible coloration and decoloration. This is in strong contrast to TiO₂/viologen layers, where the decoloration is severely restricted when no lithium is present in the electrolyte. These improvements are already observed at low antimony dopant concentrations (2% Sb), resulting in hybrid layers with good electrochemical properties and sufficient transparency in the visible region. Due to the high conductivity of ATO over a broad range of potentials, it can be used on both the working and the counter electrodes in an electrochemical device. With both of the electrodes equipped with suitable dye molecules, a full device was constructed that also utilized a non-intercalating electrolyte. The device displayed remarkably fast switching times (< 0.5 s) and good long-term stability, i.e., a high electrochromic contrast is retained after prolonged switching between the colored and transparent state.

The ATO/viologen electrode can also be combined with an ATO layer as a counter electrode that is not modified with an organic dye as a redox-active molecule but rather an inorganic, optically passive compound. A simple immersion process can decorate the inner surface of mesoporous ATO layers decorated with a cerium complex. Calcination results in the formation of a finely divided cerium compound on the inner surface, leading to improved electrochemical properties compared to bare ATO layers. First, the cerium species can be reversibly oxidized and reduced at the surface of the ATO particles, which therefore greatly increases the charge storage capacity of the layers. The capacity can be further improved by performing multiple decoration cycles to increase the number of cerium species within the layers. Notably, the cerium species is redox-active even when a non-intercalating electrolyte is used. Since the redox potential of the Ce³⁺/Ce⁴⁺ couple is very positive, high antimony doping concentrations (15%) are required as these ATO nanoparticles exhibit the highest conductivity at positive potentials. A high positive potential allows for the oxidization of a large portion of the cerium species contained in the layers. While this is advantageous in terms of the charge storage capacity, layers of ATO particles with high antimony contents show reduced transparency due to the increased plasmon absorption. However, after the decoration of the ATO layers with cerium species and the subsequent calcination, the layers exhibit higher transparency than the bare ATO layers. Due to the combination of both high transparency and high capacity, the cerium-decorated ATO layers fulfill the desired

Summary

requirements of a charge storage layer in electrochromic devices. This is highlighted in a full device composed of the cerium-decorated ATO layer and the aforementioned ATO/viologen layer. Besides the good long-term stability with a non-intercalating electrolyte, the device also allowed for fast switching (< 0.5 s). Due to the broad conductivity range of ATO, the mesoporous layers could potentially also be decorated with other inorganic materials to alter the electrochemical response of the ATO layers.

The second type of nanoparticles used in this thesis for an electrochemical application were luminescent $\text{LaPO}_4:\text{Ce,Tb}$ nanoparticles. Colloidal solutions of these particles with a small size of 4 nm were again utilized to prepare thin films on a conductive substrate with the goal of electrochemically switching the luminescence of the particles. This can be realized by changing the redox state of cerium atoms at the surface of the nanoparticles. Since the particles are not electrically conducting, however, the electrochemical generation of Ce^{4+} cannot be realized by simply applying positive potentials to the electrode composed of the thin nanoparticle film. Instead, organic molecules have to be employed as redox shuttles that transfer electrons between the nanoparticles and the current collector. Thus, with a redox shuttle that has a redox potential more positive than that of the $\text{Ce}^{3+}/\text{Ce}^{4+}$ couple in the $\text{LaPO}_4:\text{Ce,Tb}$ nanoparticles, a small amount of Ce^{3+} can be oxidized to Ce^{4+} which quenches the luminescence of the nanoparticle layer. Likewise, a redox shuttle with low redox potential can reduce all cerium species back to Ce^{3+} and therefore restore the green luminescence. This was highlighted by a special electrochemical device that made it possible to observe the switching in situ. With an oxidizing and a reducing redox shuttle, repeatable on/off switching with remarkable switching times was realized. Further, when a layer of $\text{LaPO}_4:\text{Ce,Tb}$ was diluted with $\text{LaPO}_4:\text{Eu}$, the emission of the device could be switched between yellow (emission of both nanoparticles) and red (emission of only $\text{LaPO}_4:\text{Eu}$).

Appendix

Table A1: Sn and Sb contents of ATO nanoparticles with different antimony doping concentrations, obtained by X-ray fluorescence measurements that were performed with a Panalytical Axios XRF spectrometer.

Desired Sb content	Sn content [%]	Sb content [%]
0%	100	0
2%	97.7	2.3
5%	94.8	5.2
10%	89.6	10.4
15%	85.4	14.5

Appendix

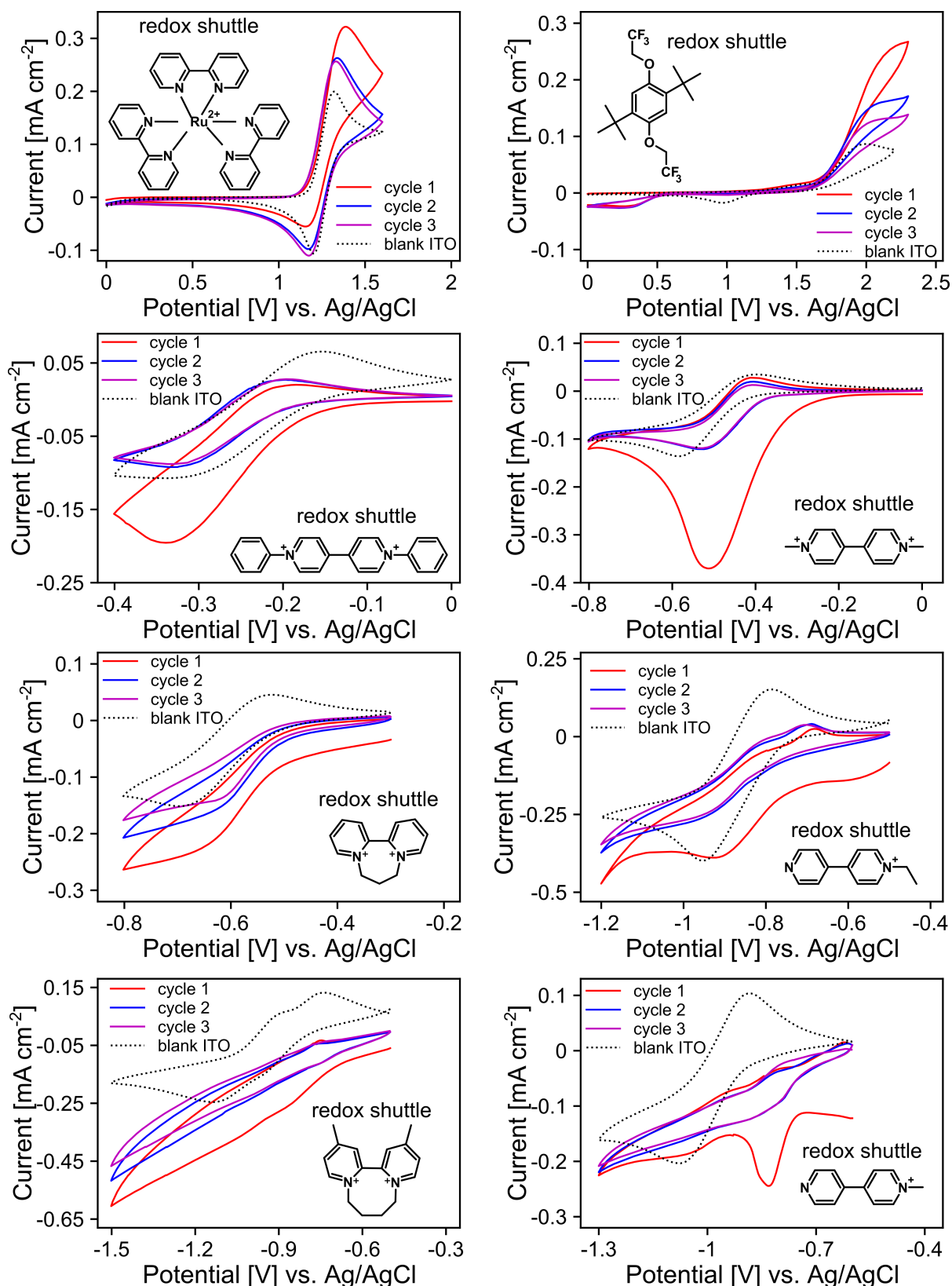


Figure A1: CV's of LaPO₄:Ce,Tb thin films on ITO in 0.1 M LiClO₄/acetonitrile measured at 20 mV s⁻¹ containing the displayed redox shuttles, dotted line: on bare ITO.

Appendix

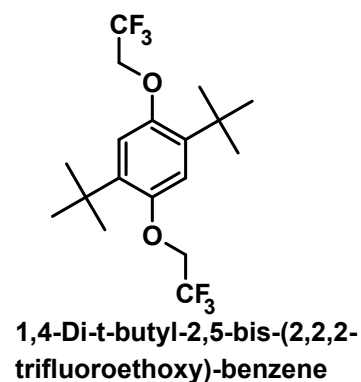
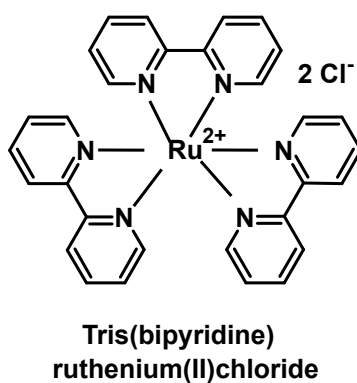
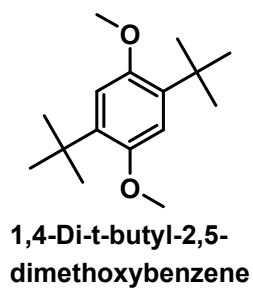
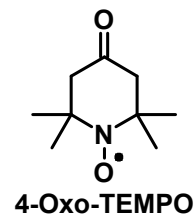
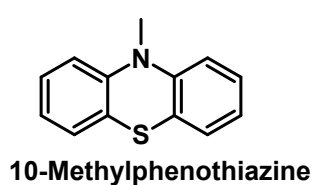
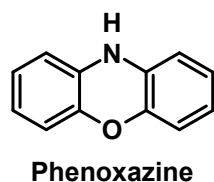
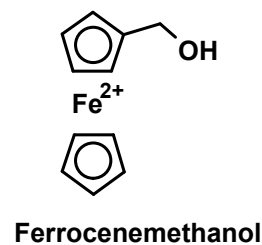
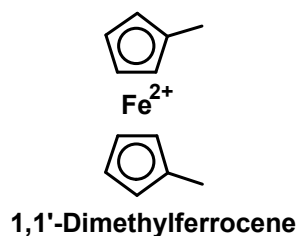
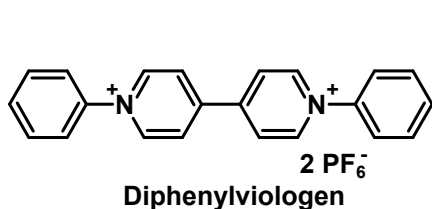
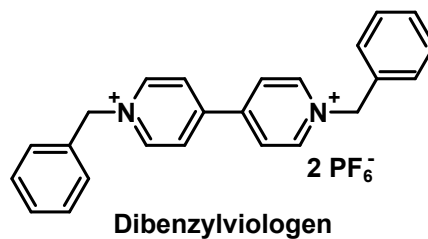
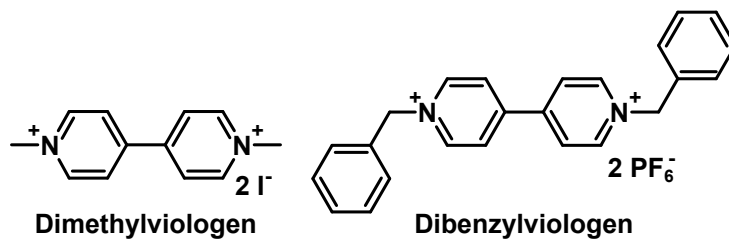
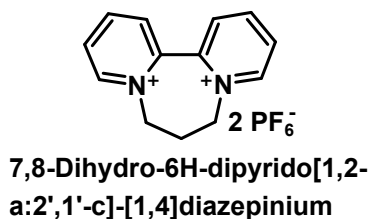
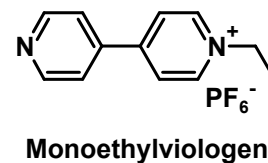
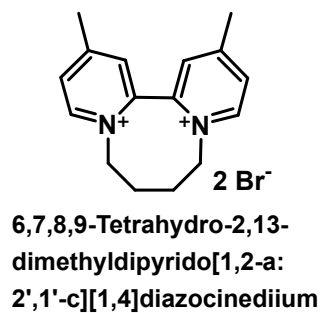
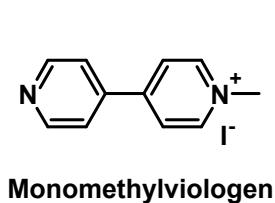


Figure A2: Overview of all used redox shuttles.

Appendix

Table A2: Redox potential and capability to electrochemically oxidize Ce^{3+} in $\text{LaPO}_4:\text{Ce,Tb}$ nanoparticles for all used redox shuttles. The redox potentials were evaluated by cyclic voltammetry of the individual redox shuttles (1 mM concentration) in 0.1 M LiClO_4 in acetonitrile at 50 mV s^{-1} on an ITO working electrode.

Redox shuttle	Redox potential [V] vs. Ag/AgCl	Electrochemical oxidation of Ce^{3+}
Monomethylviologen	-0.97	no
6,7,8,9-Tetrahydro-2,13-dimethylpyrido[1,2-a:2',1'-c][1,4]diazocinediium	-0.88	no
Monoethylviologen	-0.87	no
7,8-Dihydro-6H-dipyrido[1,2-a:2',1'-c]-[1,4]diazepinium	-0.61	no
Dimethylviologen	-0.48	no
Dibenzylviologen	-0.41	no
Diphenylviologen	-0.24	no
1,1'-Dimethylferrocene	0.29	no
Ferrocenemethanol	0.37	no
Phenoxazine	0.61	no
10-Methylphenothiazine	0.7	no
4-Oxo-TEMPO	0.89	no
1,4-Di-t-butyl-2,5-dimethoxybenzene	1.15	yes
Tris(bipyridine)-ruthenium(II)chloride	1.27	yes
1,4-Di-t-butyl-2,5-bis(2,2,2-trifluoroethoxy)-benzene	1.48	yes

References

- [1] S. L. Pal, U. Jana, P. K. Manna, G. P. Mohanta, and R. Manavalan. Nanoparticle: An overview of preparation and characterization. *Journal of Applied Pharmaceutical Science* **2011**, 228–234.
- [2] F. J. Heiligtag and M. Niederberger. The fascinating world of nanoparticle research. *Materials Today* **2013**, 16, 262–271.
- [3] A. N. Shipway, E. Katz, and I. Willner. Nanoparticle Arrays on Surfaces for Electronic, Optical, and Sensor Applications. *ChemPhysChem* **2000**, 1, 18–52.
- [4] Y. Gao and Z. Tang. Design and Application of Inorganic Nanoparticle Superstructures: Current Status and Future challenges. *Small* **2011**, 7, 2133–2146.
- [5] D. G. Shchukin and R. A. Caruso. Template Synthesis and Photocatalytic Properties of Porous Metal Oxide Spheres Formed by Nanoparticle Infiltration. *Chemistry of Materials* **2004**, 16, 2287–2292.
- [6] C.-T. Wang and S.-H. Ro. Surface nature of nanoparticle gold/iron oxide aerogel catalysts. *Journal of Non-Crystalline Solids* **2006**, 352, 35–43.
- [7] Y. Xu and B. Zhang. Recent advances in porous Pt-based nanostructures: synthesis and electrochemical applications. *Chemical Society Reviews* **2014**, 43, 2439–2450.
- [8] C. Zhu, D. Du, A. Eychmüller, and Y. Lin. Engineering Ordered and Nonordered Porous Noble Metal Nanostructures: Synthesis, Assembly, and Their Applications in Electrochemistry. *Chemical Reviews* **2015**, 115, 8896–8943.
- [9] M. Deepa, A. Srivastava, K. Sood, and S. Agnihotry. Nanostructured mesoporous tungsten oxide films with fast kinetics for electrochromic smart windows. *Nanotechnology* **2006**, 17, 2625.
- [10] A. R. Studart, E. Amstad, and L. J. Gauckler. Colloidal Stabilization of Nanoparticles in Concentrated Suspensions. *Langmuir* **2007**, 23, 1081–1090.
- [11] F. Gambinossi, S. E. Mylon, and J. K. Ferri. Aggregation kinetics and colloidal stability of functionalized nanoparticles. *Advances in Colloid and Interface Science* **2015**, 222, 332–349.
- [12] K. H. Kim, S. W. Lee, D. W. Shin, and C. G. Park. Effect of Antimony Addition on Electrical and Optical Properties of Tin Oxide Film. *Journal of the American Ceramic Society* **1994**, 77, 915–921.
- [13] S. S. Lekshmy, G. P. Daniel, and K. Joy. Microstructure and physical properties of sol gel derived SnO₂:Sb thin films for optoelectronic applications. *Applied Surface Science* **2013**, 274, 95–100.
- [14] G. Bühler and C. Feldmann. Microwave-Assisted Synthesis of Luminescent LaPO₄:Ce,Tb Nanocrystals in Ionic Liquids. *Angewandte Chemie International Edition* **2006**, 45, 4864–4867.
- [15] M. Yu, J. Lin, J. Fu, H. Zhang, and Y. Han. Sol-gel synthesis and photoluminescent properties of LaPO₄:a (a=Eu³⁺, Ce³⁺, Tb³⁺) nanocrystalline thin films. *Journal of Materials Chemistry* **2003**, 13, 1413–1419.
- [16] D. Titus, E. J. J. Samuel, and S. M. Roopan. Nanoparticle characterization techniques. In 'Green Synthesis, Characterization and Applications of Nanoparticles', Elsevier, **2019**. 303–319.

References

- [17] S. O'Brien, L. Brus, and C. B. Murray. Synthesis of Monodisperse Nanoparticles of Barium Titanate: Toward a Generalized Strategy of Oxide Nanoparticle Synthesis. *Journal of the American Chemical Society* **2001**, 123, 12085–12086.
- [18] R. Narayanan and M. A. El-Sayed. Catalysis with Transition Metal Nanoparticles in Colloidal Solution: Nanoparticle Shape Dependence and Stability. *The Journal of Physical Chemistry B* **2005**, 109, 12663–12676.
- [19] A. Albanese, P. S. Tang, and W. C. Chan. The Effect of Nanoparticle Size, Shape, and Surface Chemistry on Biological Systems. *Annual Review of Biomedical Engineering* **2012**, 14, 1–16.
- [20] Y. Gogotsi. What Nano Can Do For Energy Storage. *ACS Nano* **2014**, 8, 5369–5371.
- [21] X.-L. Wu, L.-Y. Jiang, F.-F. Cao, Y.-G. Guo, and L.-J. Wan. LiFePO₄ Nanoparticles Embedded in a Nanoporous Carbon Matrix: Superior Cathode Material for Electrochemical Energy-Storage Devices. *Advanced Materials* **2009**, 21, 2710–2714.
- [22] S. Navalón and H. García. Nanoparticles for Catalysis. *Nanomaterials* **2016**, 6, 123.
- [23] M. Arenz, K. J. Mayrhofer, V. Stamenkovic, B. B. Blizanac, T. Tomoyuki, P. N. Ross, and N. M. Markovic. The Effect of the Particle Size on the Kinetics of CO Electrooxidation on High Surface Area Pt Catalysts. *Journal of the American Chemical Society* **2005**, 127, 6819–6829.
- [24] M. De, P. S. Ghosh, and V. M. Rotello. Applications of Nanoparticles in Biology. *Advanced Materials* **2008**, 20, 4225–4241.
- [25] L. Zhang, F. Gu, J. Chan, A. Wang, R. Langer, and O. Farokhzad. Nanoparticles in Medicine: Therapeutic Applications and Developments. *Clinical Pharmacology & Therapeutics* **2008**, 83, 761–769.
- [26] D. F. Moyano and V. M. Rotello. Nano Meets Biology: Structure and Function at the Nanoparticle Interface. *Langmuir* **2011**, 27, 10376–10385.
- [27] T. P. Yadav, R. M. Yadav, and D. P. Singh. Mechanical Milling: a Top Down Approach for the Synthesis of Nanomaterials and Nanocomposites. *Nanoscience and Nanotechnology* **2012**, 2, 22–48.
- [28] M. Naghdi, M. Taheran, S. K. Brar, T. Rouissi, M. Verma, R. Y. Surampalli, and J. R. Valero. A green method for production of nanobiochar by ball milling-optimization and characterization. *Journal of Cleaner Production* **2017**, 164, 1394–1405.
- [29] H. Soleimani, M. K. Baig, N. Yahya, L. Khodapanah, M. Sabet, B. M. Demiral, and M. Burda. Synthesis of ZnO nanoparticles for oil-water interfacial tension reduction in enhanced oil recovery. *Applied Physics A* **2018**, 124, 1–13.
- [30] K. Wegner, B. Walker, S. Tsantilis, and S. E. Pratsinis. Design of metal nanoparticle synthesis by vapor flow condensation. *Chemical Engineering Science* **2002**, 57, 1753–1762.
- [31] F. Kaatz, G. Chow, and A. Edelstein. Narrowing sputtered nanoparticle size distributions. *Journal of Materials Research* **1993**, 8, 995–1000.
- [32] R. Mueller, L. Mädler, and S. E. Pratsinis. Nanoparticle synthesis at high production rates by flame spray pyrolysis. *Chemical Engineering Science* **2003**, 58, 1969–1976.
- [33] M. T. Swihart. Vapor-phase synthesis of nanoparticles. *Current Opinion in Colloid & Interface Science* **2003**, 8, 127–133.

References

- [34] J. Kimling, M. Maier, B. Okenve, V. Kotaidis, H. Ballot, and A. Plech. Turkevich Method for Gold Nanoparticle Synthesis Revisited. *The Journal of Physical Chemistry B* **2006**, 110, 15700–15707.
- [35] G. H. Lee and J.-M. Zuo. Growth and Phase Transformation of Nanometer-Sized Titanium Oxide Powders Produced by the Precipitation Method. *Journal of the American Ceramic Society* **2004**, 87, 473–479.
- [36] M. Parashar, V. K. Shukla, and R. Singh. Metal oxides nanoparticles via sol-gel method: a review on synthesis, characterization and applications. *Journal of Materials Science: Materials in Electronics* **2020**, 31, 3729–3749.
- [37] K. Byrappa and T. Adschiri. Hydrothermal technology for nanotechnology. *Progress in Crystal Growth and Characterization of Materials* **2007**, 53, 117–166.
- [38] C. Homann, L. Krukewitt, F. Frenzel, B. Grauel, C. Würth, U. Resch-Genger, and M. Haase. NaYF₄:yb,er/NaYF₄ Core/Shell Nanocrystals with High Upconversion Luminescence Quantum Yield. *Angewandte Chemie International Edition* **2018**, 57, 8765–8769.
- [39] B. G. Lewis and D. C. Paine. Applications and Processing of Transparent Conducting Oxides. *MRS bulletin* **2000**, 25, 22–27.
- [40] R. A. Afre, N. Sharma, M. Sharon, and M. Sharon. Transparent conducting oxide films for various applications: A review. *Reviews on Advanced Materials Science* **2018**, 53, 79–89.
- [41] E. Della Gaspera, A. S. Chesman, J. Van Embden, and J. J. Jasieniak. Non-injection Synthesis of Doped Zinc Oxide Plasmonic Nanocrystals. *ACS Nano* **2014**, 8, 9154–9163.
- [42] T. Wang and P. V. Radovanovic. Free Electron Concentration in Colloidal Indium Tin Oxide Nanocrystals Determined by Their Size and Structure. *The Journal of Physical Chemistry C* **2011**, 115, 406–413.
- [43] S. Cao, S. Zhang, T. Zhang, A. Fisher, and J. Y. Lee. Metal-doped TiO₂ colloidal nanocrystals with broadly tunable plasmon resonance absorption. *Journal of Materials Chemistry C* **2018**, 6, 4007–4014.
- [44] M. Kojima, H. Kato, and M. Gatto. Blackening of tin oxide thin films heavily doped with antimony. *Philosophical Magazine B* **1993**, 68, 215–222.
- [45] X. Wang, X. Wang, Q. Di, H. Zhao, B. Liang, and J. Yang. Mutual Effects of Fluorine Dopant and Oxygen Vacancies on Structural and Luminescence Characteristics of F Doped SnO₂ Nanoparticles. *Materials* **2017**, 10, 1398.
- [46] N. G. Khlebtsov and L. A. Dykman. Optical properties and biomedical applications of plasmonic nanoparticles. *Journal of Quantitative Spectroscopy and Radiative Transfer* **2010**, 111, 1–35.
- [47] A. Agrawal, S. H. Cho, O. Zandi, S. Ghosh, R. W. Johns, and D. J. Milliron. Localized Surface Plasmon Resonance in Remiconductor Nanocrystals. *Chemical Reviews* **2018**, 118, 3121–3207.
- [48] K. M. Mayer and J. H. Hafner. Localized Surface Plasmon Resonance Sensors. *Chemical Reviews* **2011**, 111, 3828–3857.
- [49] J. Ederth, P. Johnsson, G. Niklasson, A. Hoel, A. Hultåker, P. Heszler, C. Granqvist, A. Van Doorn, M. Jongorius, and D. Burgard. Electrical and optical properties of thin films consisting of tin-doped indium oxide nanoparticles. *Physical Review B* **2003**, 68, 155410.

References

- [50] P. Yang, J. Zheng, Y. Xu, Q. Zhang, and L. Jiang. Colloidal Synthesis and Applications of Plasmonic Metal Nanoparticles. *Advanced Materials* **2016**, 28, 10508–10517.
- [51] P. Mulvaney. Surface plasmon spectroscopy of nanosized metal particles. *Langmuir* **1996**, 12, 788–800.
- [52] S. Link and M. A. El-Sayed. Size and Temperature Dependence of the Plasmon Absorption of Colloidal Gold Nanoparticles. *The Journal of Physical Chemistry B* **1999**, 103, 4212–4217.
- [53] B. J. Wiley, S. H. Im, Z.-Y. Li, J. McLellan, A. Siekkinen, and Y. Xia. Maneuvering the Surface Plasmon Resonance of Silver Nanostructures Through Shape-Controlled Synthesis. *The Journal of Physical Chemistry B* **2006**, 110, 15666–15675.
- [54] S. Underwood and P. Mulvaney. Effect of the Solution Refractive Index on the Color of Gold Colloids. *Langmuir* **1994**, 10, 3427–3430.
- [55] G. Blasse and B. Grabmaier. *Luminescent materials*. Springer, **1994**.
- [56] M. H. Werts. Making sense of lanthanide luminescence. *Science Progress* **2005**, 88, 101–131.
- [57] F. H. Firsching and S. N. Brune. Solubility Products of the Trivalent Rare-Earth Phosphates. *Journal of Chemical and Engineering Data* **1991**, 36, 93–95.
- [58] F. T. Rabouw, S. A. Den Hartog, T. Senden, and A. Meijerink. Photonic effects on the Förster resonance energy transfer efficiency. *Nature Communications* **2014**, 5, 1–6.
- [59] H. Meyssamy, K. Riwozki, A. Kornowski, S. Nased, and M. Haase. Wet-Chemical Synthesis of Doped Colloidal Nanomaterials: Particles and Fibers of LaPO₄:Eu, LaPO₄:Ce, and LaPO₄:Ce,Tb. *Advanced Materials* **1999**, 11, 840–844.
- [60] G. Phaomei, R. Ningthoujam, W. R. Singh, R. S. Loitongbam, N. S. Singh, A. Rath, R. Juluri, and R. Vatsa. Luminescence switching behavior through redox reaction in Ce³⁺ co-doped LaPO₄:Tb³⁺ nanorods: Re-dispersible and polymer film. *Dalton Transactions* **2011**, 40, 11571–11580.
- [61] S. K. Gupta, P. Ghosh, M. Sahu, K. Bhattacharyya, R. Tewari, and V. Natarajan. Intense red emitting monoclinic LaPO₄:Eu³⁺ nanoparticles: host-dopant energy transfer dynamics and photoluminescence properties. *RSC Advances* **2015**, 5, 58832–58842.
- [62] S. E. Lohse and C. J. Murphy. Applications of Colloidal Inorganic Nanoparticles: From Medicine to Energy. *Journal of the American Chemical Society* **2012**, 134, 15607–15620.
- [63] T. Pellegrino, S. Kudera, T. Liedl, A. Muñoz Javier, L. Manna, and W. J. Parak. On the Development of Colloidal Nanoparticles Towards Multifunctional Structures and their Possible Use for Biological Applications. *Small* **2005**, 1, 48–63.
- [64] M. Navlani-García, D. Salinas-Torres, K. Mori, Y. Kuwahara, and H. Yamashita. Tailoring the Size and Shape of Colloidal Noble Metal Nanocrystals as a Valuable Tool in Catalysis. *Catalysis Surveys from Asia* **2019**, 23, 127–148.
- [65] S. D. Burnside, V. Shklover, C. Barbé, P. Comte, F. Arendse, K. Brooks, and M. Grätzel. Self-Organization of TiO₂ Nanoparticles in Thin Films. *Chemistry of Materials* **1998**, 10, 2419–2425.

References

- [66] D. I. Gittins, A. S. Susha, B. Schoeler, and F. Caruso. Dense Nanoparticulate Thin Films via Gold Nanoparticle Self-Assembly. *Advanced Materials* **2002**, 14, 508–512.
- [67] W. B. Russel, W. Russel, D. A. Saville, and W. R. Schowalter. *Colloidal Dispersions*. Cambridge university press, **1991**.
- [68] Y. Dahman, H. Javaheri, J. Chen, and B. A.-C. Sulaiman. Nanoparticles. In 'Nanotechnology and Functional Materials for Engineers', Elsevier, **2017**. 93–119.
- [69] E. Joseph and G. Singhvi. Multifunctional nanocrystals for cancer therapy: a potential nanocarrier. *Nanomaterials for Drug Delivery and Therapy* **2019**, 91–116.
- [70] T. L. Moore, L. Rodriguez-Lorenzo, V. Hirsch, S. Balog, D. Urban, C. Jud, B. Rothen-Rutishauser, M. Lattuada, and A. Petri-Fink. Nanoparticle colloidal stability in cell culture media and impact on cellular interactions. *Chemical Society Reviews* **2015**, 44, 6287–6305.
- [71] B. L. Bischoff and M. A. Anderson. Peptization Process in the Sol-Gel Preparation of Porous Anatase (TiO₂). *Chemistry of Materials* **1995**, 7, 1772–1778.
- [72] S. J. Iyengar, M. Joy, T. Maity, J. Chakraborty, R. K. Kotnala, and S. Ghosh. Colloidal properties of water dispersible magnetite nanoparticles by photon correlation spectroscopy. *RSC Advances* **2016**, 6, 14393–14402.
- [73] S. Elbasuney. Sustainable steric stabilization of colloidal titania nanoparticles. *Applied Surface Science* **2017**, 409, 438–447.
- [74] Y. Wu, L. Wang, M. Xiao, and X. Huang. A novel sonochemical synthesis and nanostructured assembly of polyvinylpyrrolidone-capped CdS colloidal nanoparticles. *Journal of Non-Crystalline Solids* **2008**, 354, 2993–3000.
- [75] L. M. Sanchez, D. A. Martin, V. A. Alvarez, and J. S. Gonzalez. Polyacrylic acid-coated iron oxide magnetic nanoparticles: The polymer molecular weight influence. *Colloids and Surfaces A: Physicochemical and Engineering Aspects* **2018**, 543, 28–37.
- [76] Z. Liu, O. L. Lanier, and A. Chauhan. Poly (Vinyl Alcohol) Assisted Synthesis and Anti-Solvent Precipitation of Gold Nanoparticles. *Nanomaterials* **2020**, 10, 2359.
- [77] L. Zhang, R. He, and H.-C. Gu. Oleic acid coating on the monodisperse magnetite nanoparticles. *Applied Surface Science* **2006**, 253, 2611–2617.
- [78] S. Mourdikoudis and L. M. Liz-Marzán. Oleylamine in Nanoparticle Synthesis. *Chemistry of Materials* **2013**, 25, 1465–1476.
- [79] D. H. Napper. Steric Stabilization. *Journal of Colloid and Interface Science* **1977**, 58, 390–407.
- [80] D. S. Dalavi, R. S. Devan, R. A. Patil, R. S. Patil, Y.-R. Ma, S. B. Sadale, I. Kim, J.-H. Kim, and P. S. Patil. Efficient electrochromic performance of nanoparticulate WO₃ thin films. *Journal of Materials Chemistry C* **2013**, 1, 3722–3728.
- [81] T. D. Lee and A. U. Ebong. A review of thin film solar cell technologies and challenges. *Renewable and Sustainable Energy Reviews* **2017**, 70, 1286–1297.
- [82] D. S. Hinczewski, M. Hinczewski, F. Tepehan, and G. Tepehan. Optical filters from SiO₂ and TiO₂ multi-layers using sol-gel spin coating method. *Solar Energy Materials and Solar Cells* **2005**, 87, 181–196.
- [83] P. Mitra, A. P. Chatterjee, and H. S. Maiti. ZnO thin film sensor. *Materials Letters* **1998**, 35, 33–38.

References

- [84] Z. Liang, M. Liu, C. Ma, L. Shen, L. Lu, and C.-L. Jia. High-performance $\text{BaZr}_{0.35}\text{Ti}_{0.65}\text{O}_3$ thin film capacitors with ultrahigh energy storage density and excellent thermal stability. *Journal of Materials Chemistry A* **2018**, 6, 12291–12297.
- [85] H. T. Chang, N.-M. Wu, and F. Zhu. A kinetic model for photocatalytic degradation of organic contaminants in a thin-film TiO_2 catalyst. *Water Research* **2000**, 34, 407–416.
- [86] A. K. S. Kumar, Y. Zhang, D. Li, and R. G. Compton. A mini-review: How reliable is the drop casting technique? *Electrochemistry Communications* **2020**, 121, 106867.
- [87] R. D. Deegan, O. Bakajin, T. F. Dupont, G. Huber, S. R. Nagel, and T. A. Witten. Capillary flow as the cause of ring stains from dried liquid drops. *Nature* **1997**, 389, 827–829.
- [88] L. Liu, M. Layani, S. Yellinek, A. Kamyshny, H. Ling, P. S. Lee, S. Magdassi, and D. Mandler. “nano to nano” electrodeposition of WO_3 crystalline nanoparticles for electrochromic coatings. *Journal of Materials Chemistry A* **2014**, 2, 16224–16229.
- [89] S. Karuppuchamy, D. P. Amalnerkar, K. Yamaguchi, T. Yoshida, T. Sugiura, and H. Minoura. Cathodic Electrodeposition of TiO_2 Thin Films for Dye-Sensitized Photoelectrochemical Applications. *Chemistry Letters* **2001**, 30, 78–79.
- [90] J. J. Richardson, J. Cui, M. Bjornmalm, J. A. Braunger, H. Ejima, and F. Caruso. Innovation in Layer-by-Layer Assembly. *Chemical Reviews* **2016**, 116, 14828–14867.
- [91] D. Lee, M. F. Rubner, and R. E. Cohen. All-Nanoparticle Thin-Film Coatings. *Nano Letters* **2006**, 6, 2305–2312.
- [92] J. L. Yang, S. J. An, W. I. Park, G.-C. Yi, and W. Choi. Photocatalysis Using ZnO Thin Films and Nanoneedles Grown by Metal-Organic Chemical Vapor Deposition. *Advanced Materials* **2004**, 16, 1661–1664.
- [93] P. A. Pandey, G. R. Bell, J. P. Rourke, A. M. Sanchez, M. D. Elkin, B. J. Hickey, and N. R. Wilson. Physical Vapor Deposition of Metal Nanoparticles on Chemically Modified Graphene: Observations on Metal-Graphene Interactions. *Small* **2011**, 7, 3202–3210.
- [94] J. Halme, J. Saarinen, and P. Lund. Spray deposition and compression of TiO_2 nanoparticle films for dye-sensitized solar cells on plastic substrates. *Solar Energy Materials and Solar Cells* **2006**, 90, 887–899.
- [95] Q. Ma, H.-M. Zheng, Y. Shao, B. Zhu, W.-J. Liu, S.-J. Ding, and D. W. Zhang. Atomic-Layer-Deposition of Indium Oxide Nano-films for Thin-Film Transistors. *Nanoscale Research Letters* **2018**, 13, 1–8.
- [96] J. Rashid, M. Barakat, N. Salah, and S. S. Habib. ZnO -nanoparticles thin films synthesized by RF sputtering for photocatalytic degradation of 2-chlorophenol in synthetic wastewater. *Journal of Industrial and Engineering Chemistry* **2015**, 23, 134–139.
- [97] M. A. Aouaj, R. Diaz, A. Belayachi, F. Rueda, and M. Abd-Lefdil. Comparative study of ITO and FTO thin films grown by spray pyrolysis. *Materials Research Bulletin* **2009**, 44, 1458–1461.
- [98] B. G. Jung, S.-H. Min, C.-W. Kwon, S.-H. Park, K.-B. Kim, and T.-S. Yoon. Colloidal Nanoparticle-Layer Formation Through Dip-Coating: Effect of Solvents and

References

- Substrate Withdrawing Speed. *Journal of The Electrochemical Society* **2009**, 156, K86.
- [99] Y.-K. Hong, H. Kim, G. Lee, W. Kim, J.-I. Park, J. Cheon, and J.-Y. Koo. Controlled two-dimensional distribution of nanoparticles by spin-coating method. *Applied Physics Letters* **2002**, 80, 844–846.
- [100] Y. Natsume and H. Sakata. Zinc oxide films prepared by sol-gel spin-coating. *Thin Solid Films* **2000**, 372, 30–36.
- [101] C. J. Brinker and G. W. Scherer. *Sol-gel science: the physics and chemistry of sol-gel processing*. Academic press, **2013**.
- [102] N. Sahu, B. Parija, and S. Panigrahi. Fundamental understanding and modeling of spin coating process: A review. *Indian Journal of Physics* **2009**, 83, 493–502.
- [103] N. Zavanelli and W.-H. Yeo. Advances in Screen Printing of Conductive Nanomaterials for Stretchable Electronics. *ACS Omega* **2021**, 6, 9344–9351.
- [104] H. M. Mohamed. Screen-printed disposable electrodes: Pharmaceutical applications and recent developments. *TrAC Trends in Analytical Chemistry* **2016**, 82, 1–11.
- [105] N. N. Dinh, N. M. Quyen, D. N. Chung, M. Zikova, and V.-V. Truong. Highly-efficient electrochromic performance of nanostructured TiO₂ films made by doctor blade technique. *Solar Energy Materials and Solar Cells* **2011**, 95, 618–623.
- [106] A. Berni, M. Mennig, and H. Schmidt. Doctor blade. In 'Sol-gel Technologies for Glass Producers and Users', Springer, **2004**. 89–92.
- [107] C. Granqvist. Electrochromism and smart window design. *Solid State Ionics* **1992**, 53, 479–489.
- [108] C. M. Lampert. Large-area smart glass and integrated photovoltaics. *Solar Energy Materials and Solar Cells* **2003**, 76, 489–499.
- [109] L. Wang, M. Guo, J. Zhan, X. Jiao, D. Chen, and T. Wang. A new design of an electrochromic energy storage device with high capacity, long cycle lifetime and multicolor display. *Journal of Materials Chemistry A* **2020**, 8, 17098–17105.
- [110] C. Wang, Z. Wang, Y. Ren, X. Hou, and F. Yan. Flexible Electrochromic Zn Mirrors Based on Zn/Viologen Hybrid Batteries. *ACS Sustainable Chemistry & Engineering* **2020**, 8, 5050–5055.
- [111] J. Livage and D. Ganguli. Sol-gel electrochromic coatings and devices: a review. *Solar Energy Materials and Solar Cells* **2001**, 68, 365–381.
- [112] W.-R. Lian, Y.-C. Huang, Y.-A. Liao, K.-L. Wang, L.-J. Li, C.-Y. Su, D.-J. Liaw, K.-R. Lee, and J.-Y. Lai. Flexible Electrochromic Devices Based on Optoelectronically Active Polynorbornene Layer and Ultratransparent Graphene Electrodes. *Macromolecules* **2011**, 44, 9550–9555.
- [113] W. Dautremont-Smith. Transition metal oxide electrochromic materials and displays: a review: Part 1: oxides with cathodic coloration. *Displays* **1982**, 3, 3–22.
- [114] W. Dautremont-Smith. Transition metal oxide electrochromic materials and displays: a review: Part 2: oxides with anodic coloration. *Displays* **1982**, 3, 67–80.
- [115] K. Bange and T. Gambke. Electrochromic Materials for Optical Switching Devices. *Advanced Materials* **1990**, 2, 10–16.
- [116] Y. Shi, G. Wang, Q. Chen, J. Zheng, and C. Xu. Electrochromism and electrochromic devices of new extended viologen derivatives with various substituent benzene. *Solar Energy Materials and Solar Cells* **2020**, 208, 110413.

References

- [117] B. Gélinas, D. Das, and D. Rochefort. Air-Stable, Self-bleaching Electrochromic Device Based on Viologen- and Ferrocene-Containing Triflimide Redox Ionic Liquids. *ACS Applied Materials & Interfaces* **2017**, 9, 28726–28736.
- [118] K.-W. Kim, J. K. Lee, X. Tang, Y. Lee, J. Yeo, H. C. Moon, S. W. Lee, and S. H. Kim. Novel triphenylamine containing poly-viologen for voltage-tunable multi-color electrochromic device. *Dyes and Pigments* **2021**, 190, 109321.
- [119] Y. Alesanco, A. Viñuales, J. Ugalde, E. Azaceta, G. Cabañero, J. Rodriguez, and R. Tena-Zaera. Consecutive anchoring of symmetric viologens: Electrochromic devices providing colorless to neutral-color switching. *Solar Energy Materials and Solar Cells* **2018**, 177, 110–119.
- [120] Y. J. Kim, H. K. Jeong, J. K. Seo, S. Y. Chai, Y. S. Kim, G. I. Lim, M. H. Cho, I.-M. Lee, Y. S. Choi, and W. I. Lee. Effect of TiO₂ Particle Size on the Performance of Viologen-Anchored TiO₂ Electrochromic Device. *Journal of Nanoscience and Nanotechnology* **2007**, 7, 4106–4110.
- [121] I. Sorar, I. B. Pehlivan, J. Bohlin, C. G. Granqvist, and G. A. Niklasson. Potentiostatic rejuvenation of electrochromic WO₃ thin films: Exploring the effect of polyethylene oxide in LiClO₄-Propylene carbonate electrolytes. *Solar Energy Materials and Solar Cells* **2020**, 218, 110767.
- [122] T.-Y. Wu, W.-B. Li, C.-W. Kuo, C.-F. Chou, J.-W. Liao, H.-R. Chen, C.-G. Tseng et al. Study of Poly(Methyl Methacrylate)-Based Gel Electrolyte for Electrochromic Device. *International Journal of Electrochemical Science* **2013**, 10720–10732.
- [123] S. Agnihotry, S. Sekhon et al. Li⁺ conducting gel electrolyte for electrochromic windows. *Solid State Ionics* **2000**, 136, 573–576.
- [124] E. M. Giroto and M.-A. De Paoli. Flexible Electrochromic Windows: A Comparison Using Liquid and Solid Electrolytes. *Journal of the Brazilian Chemical Society* **1999**, 10, 394–400.
- [125] X. Zhang, Y. Tian, W. Li, S. Dou, L. Wang, H. Qu, J. Zhao, and Y. Li. Preparation and performances of all-solid-state variable infrared emittance devices based on amorphous and crystalline WO₃ electrochromic thin films. *Solar Energy Materials and Solar Cells* **2019**, 200, 109916.
- [126] W. Li, X. Zhang, X. Chen, Y. Zhao, L. Wang, M. Chen, J. Zhao, Y. Li, and Y. Zhang. Effect of independently controllable electrolyte ion content on the performance of all-solid-state electrochromic devices. *Chemical Engineering Journal* **2020**, 398, 125628.
- [127] R. Ahmad, N. O. Laschuk, I. I. Ebralidze, O. V. Zenkina, and E. B. Easton. Probing the Influence of Counter Electrode Structure on Electrochromic-Device Operating Potentials and Performance Using Electrochemical Impedance Spectroscopy. *ChemElectroChem* **2021**, 8, 2193–2204.
- [128] C. Avellaneda and A. Pawlicka. Preparation of transparent CeO₂-TiO₂ coatings for electrochromic devices. *Thin Solid Films* **1998**, 335, 245–248.
- [129] Q. Huang, Q. Zhang, Y. Xiao, Y. He, and X. Diao. Improved electrochromic performance of NiO-based thin films by lithium and tantalum co-doping. *Journal of Alloys and Compounds* **2018**, 747, 416–422.
- [130] J. He, S. Mukherjee, X. Zhu, L. You, B. W. Boudouris, and J. Mei. Highly Transparent Crosslinkable Radical Copolymer Thin Film as the Ion Storage Layer in

References

- Organic Electrochromic Devices. *ACS applied materials & interfaces* **2018**, 10, 18956–18963.
- [131] D. E. Shen, A. M. Österholm, and J. R. Reynolds. Out of sight but not out of mind: the role of counter electrodes in polymer-based solid-state electrochromic devices. *Journal of Materials Chemistry C* **2015**, 3, 9715–9725.
- [132] M. A. Aegerter, N. Leventis, and M. M. Koebel. *Aerogels Handbook*. Springer Science & Business Media, **2011**.
- [133] L. W. Hrubesh. Aerogel applications. *Journal of Non-Crystalline Solids* **1998**, 225, 335–342.
- [134] W. Wan, R. Zhang, M. Ma, and Y. Zhou. Monolithic aerogel photocatalysts: a review. *Journal of Materials Chemistry A* **2018**, 6, 754–775.
- [135] R. Baetens, B. P. Jelle, and A. Gustavsen. Aerogel insulation for building applications: A state-of-the-art review. *Energy and Buildings* **2011**, 43, 761–769.
- [136] N. Awang, A. Nasir, M. Yajid, and J. Jaafar. A review on advancement and future perspective of 3D hierarchical porous aerogels based on electrospun polymer nanofibers for electrochemical energy storage application. *Journal of Environmental Chemical Engineering* **2021**, 9, 105437.
- [137] J. Stergar and U. Maver. Review of aerogel-based materials in biomedical applications. *Journal of Sol-Gel Science and Technology* **2016**, 77, 738–752.
- [138] S. Alwin and X. Sahaya Shajan. Aerogels: promising nanostructured materials for energy conversion and storage applications. *Materials for renewable and sustainable energy* **2020**, 9, 1–27.
- [139] J.-H. Lee and S.-J. Park. Recent advances in preparations and applications of carbon aerogels: A review. *Carbon* **2020**, 163, 1–18.
- [140] M. Kotal, J. Kim, J. Oh, and I.-K. Oh. Recent Progress in Multifunctional Graphene Aerogels. *Frontiers in Materials* **2016**, 3, 29.
- [141] M. A. B. Meador, C. R. Alemán, K. Hanson, N. Ramirez, S. L. Vivod, N. Wilmoth, and L. McCorkle. Polyimide Aerogels with Amide Cross-Links: A Low Cost Alternative for Mechanically Strong Polymer Aerogels. *ACS Applied Materials & Interfaces* **2015**, 7, 1240–1249.
- [142] R. Pekala. Organic aerogels from the polycondensation of resorcinol with formaldehyde. *Journal of Materials Science* **1989**, 24, 3221–3227.
- [143] D. Khedaioui, C. Boisson, F. d’Agosto, and D. Montarnal. Polyethylene Aerogels with Combined Physical and Chemical Crosslinking: Improved Mechanical Resilience and Shape-Memory Properties. *Angewandte Chemie International Edition* **2019**, 58, 15883–15889.
- [144] H. Jin, Y. Nishiyama, M. Wada, and S. Kuga. Nanofibrillar cellulose aerogels. *Colloids and Surfaces A: Physicochemical and Engineering Aspects* **2004**, 240, 63–67.
- [145] N. Leventis, C. Sotiriou-Leventis, G. Zhang, and A.-M. M. Rawashdeh. Nano-engineering Strong Silica Aerogels. *Nano Letters* **2002**, 2, 957–960.
- [146] H. Maleki, L. Durães, and A. Portugal. An overview on silica aerogels synthesis and different mechanical reinforcing strategies. *Journal of Non-Crystalline Solids* **2014**, 385, 55–74.
- [147] A. S. Dorcheh and M. Abbasi. Silica aerogel; synthesis, properties and characterization. *Journal of materials processing technology* **2008**, 199, 10–26.

References

- [148] A. E. Gash, T. M. Tillotson, J. H. Satcher Jr, L. W. Hrubesh, and R. L. Simpson. New sol–gel synthetic route to transition and main-group metal oxide aerogels using inorganic salt precursors. *Journal of Non-Crystalline Solids* **2001**, 285, 22–28.
- [149] H. Schäfer, S. Brandt, B. Milow, S. Ichilmann, M. Steinhart, and L. Ratke. Zirconia-based Aerogels via Hydrolysis of Salts and Alkoxides: The Influence of the Synthesis Procedures on the Properties of the Aerogels. *Chemistry - An Asian Journal* **2013**, 8, 2211–2219.
- [150] F. Matter and M. Niederberger. The importance of the Macroscopic Geometry in Gas-Phase Photocatalysis. *Advanced Science* **2022**, 2105363.
- [151] F. Matter, A. L. Luna, and M. Niederberger. From colloidal dispersions to aerogels: How to master nanoparticle gelation. *Nano Today* **2020**, 30, 100827.
- [152] S. Smitha, P. Shajesh, P. Aravind, S. R. Kumar, P. K. Pillai, and K. Warriar. Effect of aging time and concentration of aging solution on the porosity characteristics of subcritically dried silica aerogels. *Microporous and Mesoporous Materials* **2006**, 91, 286–292.
- [153] H. Maleki, L. Durães, and A. Portugal. An overview on silica aerogels synthesis and different mechanical reinforcing strategies. *Journal of Non-Crystalline Solids* **2014**, 385, 55–74.
- [154] M. Alshrah, M.-P. Tran, P. Gong, H. E. Naguib, and C. B. Park. Development of high-porosity resorcinol formaldehyde aerogels with enhanced mechanical properties through improved particle necking under CO₂ supercritical conditions. *Journal of Colloid and Interface Science* **2017**, 485, 65–74.
- [155] C. García-González, M. Camino-Rey, M. Alnaief, C. Zetzl, and I. Smirnova. Supercritical drying of aerogels using CO₂: Effect of extraction time on the end material textural properties. *The Journal of Supercritical Fluids* **2012**, 66, 297–306.
- [156] C. Buratti, E. Belloni, F. Merli, and M. Zinzi. Aerogel glazing systems for building applications: A review. *Energy and Buildings* **2021**, 231, 110587.
- [157] W. Abdelwahed, G. Degobert, S. Stainmesse, and H. Fessi. Freeze-drying of nanoparticles: Formulation, process and storage considerations. *Advanced Drug Delivery Reviews* **2006**, 58, 1688–1713.
- [158] A. K. Nayak and B. Das. Introduction to polymeric gels. In ‘Polymeric Gels’, Elsevier, **2018**. 3–27.
- [159] S. Karamikamkar, H. E. Naguib, and C. B. Park. Advances in precursor system for silica-based aerogel production toward improved mechanical properties, customized morphology, and multifunctionality: A review. *Advances in Colloid and Interface Science* **2020**, 276, 102101.
- [160] H. Maleki, L. Duraes, and A. Portugal. Development of Mechanically Strong Ambient Pressure Dried Silica Aerogels with Optimized Properties. *The Journal of Physical Chemistry C* **2015**, 119, 7689–7703.
- [161] D. Quintanar-Guerrero, A. Ganem-Quintanar, M. G. Nava-Arzaluz, and E. Piñón-Segundo. Silica xerogels as pharmaceutical drug carriers. *Expert Opinion on Drug Delivery* **2009**, 6, 485–498.
- [162] G. Busca. The surface of transitional aluminas: A critical review. *Catalysis Today* **2014**, 226, 2–13.
- [163] I. Levin and D. Brandon. Metastable Alumina Polymorphs: Crystal Structures

References

- and Transition Sequences. *Journal of the American Ceramic Society* **1998**, 81, 1995–2012.
- [164] Y. Hao, C. Chen, X. Yang, G. Xiao, B. Zou, J. Yang, and C. Wang. Studies on intrinsic phase-dependent electrochemical properties of MnS nanocrystals as anodes for lithium-ion batteries. *Journal of Power Sources* **2017**, 338, 9–16.
- [165] Q. Zhang, L. Gao, and J. Guo. Effects of calcination on the photocatalytic properties of nanosized TiO₂ powders prepared by TiCl₄ hydrolysis. *Applied Catalysis B: Environmental* **2000**, 26, 207–215.
- [166] A. Sadeghzadeh-Attar. Efficient photocatalytic degradation of methylene blue dye by SnO₂ nanotubes synthesized at different calcination temperatures. *Solar Energy Materials and Solar Cells* **2018**, 183, 16–24.
- [167] M. R. Parra and F. Z. Haque. Aqueous chemical route synthesis and the effect of calcination temperature on the structural and optical properties of ZnO nanoparticles. *Journal of Materials Research and Technology* **2014**, 3, 363–369.
- [168] P. Nandi and D. Das. Photocatalytic Degradation of Rhodamine-B Dye by Stable ZnO Nanostructures with Different Calcination Temperature Induced Defects. *Applied Surface Science* **2019**, 465, 546–556.
- [169] C. R. Matias, E. J. Nassar, M. Verelst, and L. A. Rocha. Synthesis and Characterization of Nb₂O₅:La³⁺,Eu³⁺ Phosphors Obtained by the Non-Hydrolytic Sol-Gel Process. *Journal of the Brazilian Chemical Society* **2015**, 26, 2558–2570.
- [170] Y. C. Kang, I. W. Lenggoro, S. B. Park, and K. Okuyama. YAG:Ce phosphor particles prepared by ultrasonic spray pyrolysis. *Materials Research Bulletin* **2000**, 35, 789–798.
- [171] N. Dave, B. Pautler, S. Farvid, and P. Radovanovic. Synthesis and surface control of colloidal Cr³⁺-doped SnO₂ transparent magnetic semiconductor nanocrystals. *Nanotechnology* **2010**, 21, 134023.
- [172] R. O. da Silva, T. G. Conti, A. F. de Moura, D. G. Stroppa, L. C. Freitas, C. Ribeiro, E. R. Camargo, E. Longo, and E. R. Leite. Antimony-Doped Tin Oxide Nanocrystals: Synthesis and Solubility Behavior in Organic Solvents. *ChemPhysChem* **2009**, 10, 841–846.
- [173] Z. Chen, Q. Xie, J. Ding, Z. Yang, W. Zhang, and H. Cheng. Instant Postsynthesis Aqueous Dispersion of Sb-Doped SnO₂ Nanocrystals: The Synergy between Small-Molecule Amine and Sb Dopant Ratio. *ACS Applied Materials & Interfaces* **2020**, 12, 29937–29945.
- [174] I. Maurin, G. Dantelle, J.-P. Boilot, and T. Gacoin. A protected annealing process for the production of high quality colloidal oxide nanoparticles with optimized physical properties. *Journal of Materials Chemistry C* **2013**, 1, 13–22.
- [175] D. Deng and J. Y. Lee. Hollow Core-shell Mesospheres of Crystalline SnO₂ Nanoparticle Aggregates for High Capacity Li⁺ Ion Storage. *Chemistry of Materials* **2008**, 20, 1841–1846.
- [176] K. B. Baharudin, N. Abdullah, and D. Derawi. Effect of Calcination Temperature on the Physicochemical Properties of Zinc Oxide Nanoparticles Synthesized by Coprecipitation. *Materials Research Express* **2018**, 5, 125018.
- [177] A. Revaux, G. Dantelle, N. George, R. Seshadri, T. Gacoin, and J.-P. Boilot. A protected annealing strategy to enhanced light emission and photostability of YAG:Ce nanoparticle-based films. *Nanoscale* **2011**, 3, 2015–2022.

References

- [178] J.-N. Park, A. J. Forman, W. Tang, J. Cheng, Y.-S. Hu, H. Lin, and E. W. McFarland. Highly Active and Sinter-Resistant Pd-Nanoparticle Catalysts Encapsulated in Silica. *Small* **2008**, 4, 1694–1697.
- [179] J. B. Joo, Q. Zhang, I. Lee, M. Dahl, F. Zaera, and Y. Yin. Mesoporous Anatase Titania Hollow Nanostructures through Silica-Protected Calcination. *Advanced Functional Materials* **2012**, 22, 166–174.
- [180] L. Shang, Y. Liang, M. Li, G. I. Waterhouse, P. Tang, D. Ma, L.-Z. Wu, C.-H. Tung, and T. Zhang. “naked” Magnetically Recyclable Mesoporous Au- γ -Fe₂O₃ Nanocrystal Clusters: A Highly Integrated Catalyst System. *Advanced Functional Materials* **2017**, 27, 1606215.
- [181] S. Wintzheimer, F. Miller, J. Prieschl, M. Retter, and K. Mandel. Supraparticles with silica protection for redispersible, calcined nanoparticles. *Nanoscale Advances* **2019**, 1, 4277–4281.
- [182] Y. Liang, H. M. Noh, J. Xue, H. Choi, S. H. Park, B. C. Choi, J. H. Kim, and J. H. Jeong. High quality colloidal GdVO₄:yb,er upconversion nanoparticles synthesized via a protected calcination process for versatile applications. *Materials & Design* **2017**, 130, 190–196.
- [183] F. Rechberger and M. Niederberger. Synthesis of aerogels: from molecular routes to 3-dimensional nanoparticle assembly. *Nanoscale Horizons* **2017**, 2, 6–30.
- [184] C. Ziegler, A. Wolf, W. Liu, A.-K. Herrmann, N. Gaponik, and A. Eychmüller. Modern Inorganic Aerogels. *Angewandte Chemie International Edition* **2017**, 56, 13200–13221.
- [185] D. Wen and A. Eychmüller. 3D assembly of preformed colloidal nanoparticles into gels and aerogels: function-led design. *Chemical Communications* **2017**, 53, 12608–12621.
- [186] N. Shah, T. Rehan, X. Li, H. Tetik, G. Yang, K. Zhao, and D. Lin. Magnetic aerogel: an advanced material of high importance. *RSC Advances* **2021**, 11, 7187–7204.
- [187] W. Liu, A.-K. Herrmann, N. C. Bigall, P. Rodriguez, D. Wen, M. Oezaslan, T. J. Schmidt, N. Gaponik, and A. Eychmüller. Noble Metal Aerogels - Synthesis, Characterization, and Application as Electrocatalysts. *Accounts of chemical research* **2015**, 48, 154–162.
- [188] T. Nütz, U. z. Felde, and M. Haase. Wet-chemical synthesis of doped nanoparticles: Blue-colored colloids of n-doped SnO₂:Sb. *The Journal of Chemical Physics* **1999**, 110, 12142–12150.
- [189] J. Rockenberger, U. Zum Felde, M. Tischer, L. Tröger, M. Haase, and H. Weller. Near edge X-ray absorption fine structure measurements (XANES) and extended x-ray absorption fine structure measurements (EXAFS) of the valence state and coordination of antimony in doped nanocrystalline SnO₂. *The Journal of Chemical Physics* **2000**, 112, 4296–4304.
- [190] C. McGinley, H. Borchert, M. Pflughoeft, S. Al Moussalami, A. De Castro, M. Haase, H. Weller, and T. Möller. Dopant atom distribution and spatial confinement of conduction electrons in sb-doped SnO₂ nanoparticles. *Physical Review B* **2001**, 64, 245312.
- [191] T. Nütz and M. Haase. Wet-Chemical Synthesis of Doped Nanoparticles: Optical Properties of Oxygen-Deficient and Antimony-Doped Colloidal SnO₂. *The Journal of Physical Chemistry B* **2000**, 104, 8430–8437.

References

- [192] R. J. Mortimer. Electrochromic materials. *Chemical Society Reviews* **1997**, 26, 147–156.
- [193] P. R. Somani and S. Radhakrishnan. Electrochromic materials and devices: present and future. *Materials Chemistry and Physics* **2003**, 77, 117–133.
- [194] R. J. Mortimer, A. L. Dyer, and J. R. Reynolds. Electrochromic Organic and Polymeric Materials for Display Applications. *Displays* **2006**, 27, 2–18.
- [195] A. Azens and C. Granqvist. Electrochromic smart windows: energy efficiency and device aspects. *Journal of Solid State Electrochemistry* **2003**, 7, 64–68.
- [196] G. Cai, A. L.-S. Eh, L. Ji, and P. S. Lee. Recent Advances in Electrochromic Smart Fenestration. *Advanced Sustainable Systems* **2017**, 1, 1700074.
- [197] T. Deutschmann and E. Oesterschulze. Integrated electrochromic iris device for low power and space-limited applications. *Journal of Optics* **2014**, 16, 075301.
- [198] A. Hein, N. Longen, C. Kortz, F. Carl, J. Klein, M. Haase, and E. Oesterschulze. Two-dimensional spatial image control using an electrochromic graduated filter with multiple electrode configuration. *Solar Energy Materials and Solar Cells* **2020**, 215, 110549.
- [199] W. Wu, M. Wang, J. Ma, Y. Cao, and Y. Deng. Electrochromic Metal Oxides: Recent Progress and Prospect. *Advanced Electronic Materials* **2018**, 4, 1800185.
- [200] V. Rai, R. S. Singh, D. J. Blackwood, and D. Zhili. A Review on Recent Advances in Electrochromic Devices: A Material Approach. *Advanced Engeneering Material* **2020**, 22, 2000082.
- [201] C. L. Gaupp, D. M. Welsh, and J. R. Reynolds. Poly(ProDOT-Et₂): A High-Contrast, High-Coloration Efficiency Electrochromic Polymer. *Macromolecular Rapid Communications* **2002**, 23, 885–889.
- [202] H.-J. Yen and G.-S. Liou. Solution-processable triarylamine-based electroactive high performance polymers for anodically electrochromic applications. *Polymer Chemistry* **2012**, 3, 255–264.
- [203] G. Sonmez, H. Meng, and F. Wudl. Organic Polymeric Electrochromic Devices: Polychromism with Very High Coloration Efficiency. *Chemistry of Materials* **2004**, 16, 574–580.
- [204] A. A. Argun, A. Cirpan, and J. R. Reynolds. The First Truly All-Polymer Electrochromic Devices. *Advanced Materials* **2003**, 15, 1338–1341.
- [205] T. M. Benedetti, T. Carvalho, D. C. Iwakura, F. Braga, B. R. Vieira, P. Vidinha, J. Gruber, and R. M. Torresi. All solid-state electrochromic device consisting of a water soluble viologen dissolved in gelatin-based ionogel. *Solar Energy Materials and Solar Cells* **2015**, 132, 101–106.
- [206] T. Deutschmann, C. Kortz, L. Walder, and E. Oesterschulze. High contrast electrochromic iris. *Optics Express* **2015**, 23, 31544–31549.
- [207] S. Zhao, W. Huang, Z. Guan, B. Jin, and D. Xiao. A novel bis (dihydroxypropyl) viologen-based all-in-one electrochromic device with high cycling stability and coloration efficiency. *Electrochimica Acta* **2019**, 298, 533–540.
- [208] T. Gerfin, M. Grätzel, and L. Walder. Molecular and Supramolecular Surface Modification of Nanocrystalline TiO₂ Films: Charge-Separating and Charge-Injecting Devices. *Progress in Inorganic Chemistry* **1997**, 44, 345–393.
- [209] C. Kortz, A. Hein, M. Ciobanu, L. Walder, and E. Oesterschulze. Complementary hybrid electrodes for high contrast electrochromic devices with fast response. *Nature Communications* **2019**, 10, 1–7.
-

References

- [210] R. Cinnsealach, G. Boschloo, S. N. Rao, and D. Fitzmaurice. Electrochromic windows based on viologen-modified nanostructured TiO₂ films. *Solar Energy Materials and Solar Cells* **1998**, 55, 215–223.
- [211] D. Weng, Y. Shi, J. Zheng, and C. Xu. High performance black-to-transmissive electrochromic device with panchromatic absorption based on TiO₂-supported viologen and triphenylamine derivatives. *Organic Electronics* **2016**, 34, 139–145.
- [212] K. W. Shah, S.-X. Wang, D. X. Y. Soo, and J. Xu. Viologen-Based Electrochromic Materials: From Small Molecules, Polymers and Composites to Their Applications. *Polymers* **2019**, 11, 1839.
- [213] C. Bird and A. Kuhn. Electrochemistry of the Viologens. *Chemical Society Reviews* **1981**, 10, 49–82.
- [214] F. Campus, P. Bonhôte, M. Grätzel, S. Heinen, and L. Walder. Electrochromic devices based on surface-modified nanocrystalline TiO₂ thin-film electrodes. *Solar Energy Materials and Solar Cells* **1999**, 56, 281–297.
- [215] R. Cinnsealach, G. Boschloo, S. N. Rao, and D. Fitzmaurice. Coloured electrochromic windows based on nanostructured TiO₂ films modified by adsorbed redox chromophores. *Solar Energy Materials and Solar Cells* **1999**, 57, 107–125.
- [216] T. Hitosugi, N. Yamada, S. Nakao, Y. Hirose, and T. Hasegawa. Properties of TiO₂-based transparent conducting oxides. *Physica Status Solidi A* **2010**, 207, 1529–1537.
- [217] P. Bonhôte, E. Gogniat, S. Tingry, C. Barbe, N. Vlachopoulos, F. Lenzmann, P. Comte, and M. Grätzel. Efficient Lateral Electron Transport inside a Monolayer of Aromatic Amines Anchored on Nanocrystalline Metal Oxide Films. *Journal of Physical Chemistry B* **1998**, 102, 1498–1507.
- [218] J. C. Chan, N. A. Hannah, S. B. Rananavare, L. Yeager, L. Dinescu, A. Saraswat, P. Iyer, and J. P. Coleman. Mechanisms of Aging of Antimony Doped Tin Oxide Based Electrochromic Devices. *Japanese Journal of Applied Physics* **2006**, 45, L1300.
- [219] Y. Watanabe, K. Suemori, and S. Hoshino. Improvement of the electrochromic response of a low-temperature sintered dye-modified porous electrode using low-resistivity indium tin oxide nanoparticles. *AIP Advances* **2016**, 6, 065121.
- [220] K. Hoshino, M. Okuma, and K. Terashima. Electrochromic Properties of Metal Oxide Nanoparticles/Viologen Composite Film Electrodes. *Journal of Physical Chemistry C* **2018**, 122, 22577–22587.
- [221] Y. Watanabe, K. Suemori, and S. Hoshino. Electrochromic Response Characteristics of Dye-modified Porous Electrodes Affected by the Porous Film Structure. *Chemistry Letters* **2016**, 45, 1291–1293.
- [222] Y. Watanabe, K. Kanazawa, Y. Komazaki, T. Nobeshima, and S. Uemura. Structure-dependent electrochemical response characteristics of antimony tin oxide nanoparticle-based porous electrodes. *AIP Advances* **2020**, 10, 035226.
- [223] H. K. Jheong, Y. J. Kim, J. H. Pan, T.-Y. Won, and W. I. Lee. Electrochromic property of the viologen-anchored mesoporous TiO₂ films. *Journal of Electroceramics* **2006**, 17, 929–932.
- [224] H. J. Kim, J. K. Seo, Y. J. Kim, H. K. Jeong, G. I. Lim, Y. S. Choi, and W. I. Lee. Formation of ultrafast-switching viologen-anchored TiO₂ electrochromic device by introducing Sb-doped SnO₂ nanoparticles. *Solar Energy Materials and Solar Cells* **2009**, 93, 2108–2112.

References

- [225] H. Kim, K. Kim, D. Choi, M. Lee, W.-S. Chu, S.-H. Ahn, D.-M. Chun, and C. S. Lee. Microstructural Control of the Electrochromic and Ion Storage layers on the Performance of an Electrochromic Device Fabricated by the Kinetic Spray Technique. *International Journal of Precision Engineering and Manufacturing-Green Technology* **2018**, 5, 231–238.
- [226] M. Ciobanu, J. Klein, M. Middendorf, S. M. B. Mousavi, F. Carl, M. Haase, and L. Walder. High contrast hybrid electrochromic film based on cross-linked phosphonated triarylamine on mesoporous antimony doped tin oxide. *Solar Energy Materials and Solar Cells* **2019**, 203, 110186.
- [227] Y. Rong, S. Kim, F. Su, D. Myers, and M. Taya. New effective process to fabricate fast switching and high contrast electrochromic device based on viologen and Prussian blue/antimony tin oxide nano-composites with dark colored state. *Electrochimica Acta* **2011**, 56, 6230–6236.
- [228] D. Cummins, G. Boschloo, M. Ryan, D. Corr, S. N. Rao, and D. Fitzmaurice. Ultrafast Electrochromic Windows Based on Redox-Chromophore Modified Nanostructured Semiconducting and Conducting Films. *Journal of Physical Chemistry B* **2000**, 104, 11449–11459.
- [229] M. Esro, S. Georgakopoulos, H. Lu, G. Vourlias, A. Krier, W. I. Milne, W. P. Gillin, and G. Adamopoulos. Solution processed SnO₂:Sb transparent conductive oxide as an alternative to indium tin oxide for applications in organic light emitting diodes. *Journal of Materials Chemistry C* **2016**, 4, 3563–3570.
- [230] U. Zum Felde, M. Haase, and H. Weller. Electrochromism of Highly Doped Nanocrystalline SnO₂:Sb. *The Journal of Physical Chemistry B* **2000**, 104, 9388–9395.
- [231] S. D. Ponja, B. A. D. Williamson, S. Sathasivam, D. O. Scanlon, I. P. Parkin, and C. J. Carmalt. Enhanced electrical properties of antimony doped tin oxide thin films deposited via aerosol assisted chemical vapour deposition. *Journal of Materials Chemistry C* **2018**, 6, 7257–7266.
- [232] S. Liu, J. Liu, B. Wen, W. Jiang, C. Liu, W. Ding, H. Wang, N. Wang, Z. Zhang, and W. Chai. Structural, morphological, electrical and optical properties of SnO₂ nanoparticles: influence of sb doping. *Journal of Materials Science: Materials in Electronics* **2016**, 27, 6932–6938.
- [233] A. Hein, C. Kortz, and E. Oesterschulze. Tunable graduated filters based on electrochromic materials for spatial image control. *Scientific Reports* **2019**, 9, 1–9.
- [234] S. Sladkevich, A. A. Mikhaylov, P. V. Prikhodchenko, T. A. Tripol'skaya, and O. Lev. Antimony Tin Oxide (ato) Nanoparticle Formation from H₂O₂ Solutions: a New Generic Film Coating from Basic Solutions. *Inorganic chemistry* **2010**, 49, 9110–9112.
- [235] G. Boschloo and D. Fitzmaurice. Spectroelectrochemistry of Highly Doped Nanostructured Tin Dioxide Electrodes. *Journal of Physical Chemistry B* **1999**, 103, 3093–3098.
- [236] D. R. Rosseinsky and R. J. Mortimer. Electrochromic Systems and the Prospects for Devices. *Advanced Materials* **2001**, 13, 783–793.
- [237] C. G. Granqvist. Electrochromics for smart windows: Oxide-based thin films and devices. *Thin Solid Films* **2014**, 564, 1–38.

References

- [238] G. Cai, J. Wang, and P. S. Lee. Next-Generation Multifunctional Electrochromic Devices. *Accounts of Chemical Research* **2016**, 49, 1469–1476.
- [239] D. T. Gillaspie, R. C. Tenent, and A. C. Dillon. Metal-oxide films for electrochromic applications: present technology and future directions. *Journal of Materials Chemistry* **2010**, 20, 9585–9592.
- [240] K. Patel, G. Bhatt, J. Ray, P. Suryavanshi, and C. Panchal. All-inorganic solid-state electrochromic devices: a review. *Journal of Solid State Electrochemistry* **2017**, 21, 337–347.
- [241] K. Madasamy, D. Velayutham, V. Suryanarayanan, M. Kathiresan, and K.-C. Ho. Viologen-based electrochromic materials and devices. *Journal of Materials Chemistry C* **2019**, 7, 4622–4637.
- [242] F. Carpi and D. De Rossi. Colours from electroactive polymers: Electrochromic, electroluminescent and laser devices based on organic materials. *Optics & Laser Technology* **2006**, 38, 292–305.
- [243] S. Y. Choi, M. Mamak, N. Coombs, N. Chopra, and G. A. Ozin. Electrochromic Performance of Viologen-Modified Periodic Mesoporous Nanocrystalline Anatase Electrodes. *Nano letters* **2004**, 4, 1231–1235.
- [244] M. Li, Y. Wei, J. Zheng, D. Zhu, and C. Xu. Highly contrasted and stable electrochromic device based on well-matched viologen and triphenylamine. *Organic Electronics* **2014**, 15, 428–434.
- [245] W. Zhang, H. Li, E. Hopmann, and A. Y. Elezzabi. Nanostructured inorganic electrochromic materials for light applications. *Nanophotonics* **2021**, 10, 825–850.
- [246] W. A. Gazotti Jr, G. Casalbore-Miceli, A. Geri, and M.-A. de Paoli. A Solid-State Electrochromic Device Based on Two Optically Complementary Conducting Polymers. *Advanced Materials* **1998**, 10, 60–64.
- [247] D. Weng, M. Li, J. Zheng, and C. Xu. High-performance complementary electrochromic device based on surface-confined tungsten oxide and solution-phase N-methyl-phenothiazine with full spectrum absorption. *Journal of Materials Science* **2017**, 52, 86–95.
- [248] G. J. Stec, A. Lauchner, Y. Cui, P. Nordlander, and N. J. Halas. Multicolor Electrochromic Devices Based on Molecular Plasmonics. *ACS nano* **2017**, 11, 3254–3261.
- [249] A. Chaudhary, D. K. Pathak, M. Tanwar, P. R. Sagdeo, and R. Kumar. Prussian Blue-Viologen Inorganic-Organic Hybrid Blend for Improved Electrochromic Performance. *ACS Applied Electronic Materials* **2019**, 1, 892–899.
- [250] L.-C. Chen and K.-C. Ho. Design equations for complementary electrochromic devices: application to the tungsten oxide-Prussian blue system. *Electrochimica Acta* **2001**, 46, 2151–2158.
- [251] H. Huang, J. Tian, W. Zhang, Y. Gan, X. Tao, X. Xia, and J. Tu. Electrochromic properties of porous NiO thin film as a counter electrode for NiO/WO₃ complementary electrochromic window. *Electrochimica Acta* **2011**, 56, 4281–4286.
- [252] J. Zhou, G. Luo, Y. Wei, J. Zheng, and C. Xu. Enhanced electrochromic performances and cycle stability of NiO-based thin films via Li-Ti co-doping prepared by sol-gel method. *Electrochimica Acta* **2015**, 186, 182–191.
- [253] B. Orel, U. Opara Krašovec, U. Lavrenčič Štangar, and P. Judeinstein. All Sol-Gel Electrochromic Devices with Li⁺ Ionic Conductor, WO₃ Electrochromic Films and

References

- SnO₂ Counter-Electrode Films. *Journal of sol-gel science and technology* **1998**, 11, 87–104.
- [254] P. Olivi, E. C. Pereira, E. Longo, J. A. Varela, and L. O. d. S. Bulhões. Preparation and Characterization of a Dip-Coated SnO₂ Film for Transparent Electrodes for Transmissive Electrochromic Devices. *Journal of the Electrochemical Society* **1993**, 140, L81.
- [255] H. N. Kim, S. M. Cho, C. S. Ah, J. Song, H. Ryu, Y. H. Kim, and T.-Y. Kim. Electrochromic mirror using viologen-anchored nanoparticles. *Materials Research Bulletin* **2016**, 82, 16–21.
- [256] A. Verma, A. Bakhshi, and S. Agnihotry. Effect of citric acid on properties of CeO₂ films for electrochromic windows. *Solar energy materials and solar cells* **2006**, 90, 1640–1655.
- [257] B. El Idrissi, M. Addou, A. Outzourhit, M. Regragui, A. Bougrine, and A. Kachouane. Sprayed CeO₂ thin films for electrochromic applications. *Solar energy materials and solar cells* **2001**, 69, 1–8.
- [258] C. G. Granqvist. *Handbook of inorganic electrochromic materials*. Elsevier, **1995**.
- [259] P. Baudry, A. Rodrigues, M. A. Aegerter, and L. Bulhoes. Dip-Coated TiO₂-CeO₂ Films as Transparent Counter-Electrode for Transmissive Electrochromic Devices. *Journal of Non-Crystalline Solids* **1990**, 121, 319–322.
- [260] Z. C. Orel and B. Orel. Ion storage properties of CeO₂ and mixed CeO₂/SnO₂ coatings. *Journal of Materials Science* **1995**, 30, 2284–2290.
- [261] M. Veszeli, L. Kullman, A. Azens, C. Granqvist, and B. Hjörvarsson. Transparent ion intercalation films of Zr-Ce oxide. *Journal of Applied Physics* **1997**, 81, 2024–2026.
- [262] B. Zhu, C. Xia, X. Luo, and G. Niklasson. Transparent two-phase composite oxide thin films with high conductivity. *Thin Solid Films* **2001**, 385, 209–214.
- [263] J. Klein, A. Hein, E. Bold, F. Alarlan, E. Oesterschulze, and M. Haase. Intercalation-free, fast switching of mesoporous antimony doped tin oxide with cathodically coloring electrochromic dyes. *Nanoscale Advances* **2022**, 4, 2144–2152.
- [264] A. Paulenova, S. Creager, J. Navratil, and Y. Wei. Redox potentials and kinetics of the Ce³⁺/Ce⁴⁺ redox reaction and solubility of cerium sulfates in sulfuric acid solutions. *Journal of Power Sources* **2002**, 109, 431–438.
- [265] J. Klein, S. M. Beladi-Mousavi, M. Schleutker, D. H. Taffa, M. Haase, and L. Walder. Photo-Electrochemical Device Enabling Luminescence Switching of LaPO₄:Ce,Tb Nanoparticle Layers. *Advanced Optical Materials* **2021**, 9, 2001891.
- [266] G. Guerrero, P. Mutin, and A. Vioux. Anchoring of Phosphonate and Phosphate Coupling Molecules on Titania Particles. *Chemistry of Materials* **2001**, 13, 4367–4373.
- [267] J. Hu, Y. Sun, Y. Xue, M. Zhang, P. Li, K. Lian, S. Zhuiykov, W. Zhang, and Y. Chen. Highly sensitive and ultra-fast gas sensor based on CeO₂-loaded In₂O₃ hollow spheres for ppb-level hydrogen detection. *Sensors and Actuators B: Chemical* **2018**, 257, 124–135.
- [268] V. R. Naganaboina and S. G. Singh. Graphene-CeO₂ based flexible gas sensor: Monitoring of low ppm CO gas with high selectivity at room temperature. *Applied Surface Science* **2021**, 563, 150272.
-

References

- [269] Z. Wang, K. Shen, H. Xie, B. Xue, J. Zheng, and C. Xu. Robust non-complementary electrochromic device based on WO_3 film and cos catalytic counter electrode with TMTU/TMFDS²⁺ redox couple. *Chemical Engineering Journal* **2021**, 426, 131314.
- [270] K. Wang, H. Zhang, G. Chen, T. Tian, K. Tao, L. Liang, J. Gao, and H. Cao. Long-term-stable WO_3 -Pb complementary electrochromic devices. *Journal of Alloys and Compounds* **2021**, 861, 158534.
- [271] K. Wang, D. Qiu, H. Zhang, G. Chen, W. Xie, K. Tao, S. Bao, L. Liang, J. Gao, and H. Cao. Boosting charge-transfer kinetics and cyclic stability of complementary WO_3 -NiO electrochromic devices via SnO_x interfacial layer. *Journal of Science: Advanced Materials and Devices* **2021**, 6, 494–500.
- [272] N. Hashimoto, Y. Takada, K. Sato, and S. Ibuki. Green-luminescent (La,Ce) PO_4 :Tb phosphors for small size fluorescent lamps. *Journal of Luminescence* **1991**, 48, 893–897.
- [273] K. Riwotzki, H. Meyssamy, H. Schnablegger, A. Kornowski, and M. Haase. Liquid-Phase Synthesis of Colloids and Redispersible Powders of Strongly Luminescing LaPO_4 :Ce,Tb Nanocrystals. *Angewandte Chemie International Edition* **2001**, 40, 573–576.
- [274] K. Kömpe, H. Borchert, J. Storz, A. Lobo, S. Adam, T. Möller, and M. Haase. Green-Emitting CePO_4 :Tb/ LaPO_4 Core-Shell Nanoparticles with 70% Photoluminescence Quantum Yield. *Angewandte Chemie International Edition* **2003**, 42, 5513–5516.
- [275] K. Kömpe, O. Lehmann, and M. Haase. Spectroscopic Distinction of Surface and Volume Ions in Cerium(III)-and Terbium(III)-Containing Core and CoreShell Nanoparticles. *Chemistry of Materials* **2006**, 18, 4442–4446.
- [276] A. Oertel, C. Lengler, T. Walther, and M. Haase. Photonic Properties of Inverse Opals Fabricated from Lanthanide-Doped LaPO_4 Nanocrystals. *Chemistry of Materials* **2009**, 21, 3883–3888.
- [277] V. Pankratov, A. Popov, S. Chernov, A. Zharkouskaya, and C. Feldmann. Mechanism for energy transfer processes between Ce^{3+} and Tb^{3+} in LaPO_4 :Ce,Tb nanocrystals by time-resolved luminescence spectroscopy. *Physica Status Solidi B* **2010**, 247, 2252–2257.
- [278] M. Kitsuda and S. Fujihara. Quantitative Luminescence Switching in CePO_4 :Tb by Redox Reactions. *The Journal of Physical Chemistry C* **2011**, 115, 8808–8815.
- [279] C. Lv, W. Di, Z. Liu, K. Zheng, and W. Qin. Luminescent CePO_4 :Tb colloids for H_2O_2 and glucose sensing. *Analyst* **2014**, 139, 4547–4555.
- [280] G. Vinothkumar, A. I. Lalitha, and K. Suresh Babu. Cerium Phosphate-Cerium Oxide Heterogeneous Composite Nanozymes with Enhanced Peroxidase-Like Biomimetic Activity for Glucose and Hydrogen Peroxide Sensing. *Inorganic Chemistry* **2018**, 58, 349–358.
- [281] G. Yan, Y. Zhang, W. Di, and W. Qin. Synthesis of luminescent CePO_4 :Tb/Au composite for glucose detection. *Dyes and Pigments* **2018**, 159, 28–34.
- [282] W. Di, N. Shirahata, H. Zeng, and Y. Sakka. Fluorescent sensing of colloidal CePO_4 :Tb nanorods for rapid, ultrasensitive and selective detection of vitamin C. *Nanotechnology* **2010**, 21, 365501.
- [283] Q. Li and V. W.-W. Yam. Redox Luminescence Switch Based on Energy Transfer in CePO_4 :Tb³⁺ nanowires. *Angewandte Chemie* **2007**, 119, 3556–3559.

References

- [284] Y. Takano and S. Fujihara. Redox-Responsive Luminescence Switching of $\text{CePO}_4:\text{Tb}^{3+}$ Thin Films Prepared by a Sol-Gel Method. *ECS Journal of Solid State Science and Technology* **2012**, 1, R169.
- [285] G. Chen, H. Zhao, F. Rosei, and D. Ma. Effect of Redox Reaction Products on the Luminescence Switching Behavior in $\text{CePO}_4:\text{Tb}$ Nanorods. *The Journal of Physical Chemistry C* **2013**, 117, 10031–10038.
- [286] S. Fujihara, Y. Takano, and M. Kitsuda. Microstructural Aspects of the $\text{CePO}_4:\text{Tb}^{3+}$ Phosphor for Luminescence Sensing. *International Journal of Applied Ceramic Technology* **2015**, 12, 411–417.
- [287] F. P. Van der Zee and F. J. Cervantes. Impact and application of electron shuttles on the redox (bio)transformation of contaminants: A review. *Biotechnology Advances* **2009**, 27, 256–277.
- [288] K. Watanabe, M. Manefield, M. Lee, and A. Kouzuma. Electron shuttles in biotechnology. *Current Opinion in Biotechnology* **2009**, 20, 633–641.
- [289] R. Abe, T. Takata, H. Sugihara, and K. Domen. Photocatalytic overall water splitting under visible light by taon and WO_3 with an IO_3^-/I^- shuttle redox mediator. *Chemical Communications* **2005**, 3829–3831.
- [290] Y.-N. Liu, C.-C. Shen, N. Jiang, Z.-W. Zhao, X. Zhou, S.-J. Zhao, and A.-W. Xu. g- C_3N_4 Hydrogen-Bonding Viologen for Significantly Enhanced Visible-Light Photocatalytic H_2 Evolution. *ACS Catalysis* **2017**, 7, 8228–8234.
- [291] M. L. Sanchez, C.-H. Wu, M. W. Adams, and R. B. Dyer. Optimizing electron transfer from CdSe QDs to hydrogenase for photocatalytic H_2 production. *Chemical Communications* **2019**, 55, 5579–5582.
- [292] Z. Chen, Y. Qin, and K. Amine. Redox shuttles for safer lithium-ion batteries. *Electrochimica Acta* **2009**, 54, 5605–5613.
- [293] J. Chen, C. Buhrmester, and J. Dahn. Chemical Overcharge and Overdischarge Protection for Lithium-Ion Batteries. *Electrochemical and Solid-State Letters* **2004**, 8, A59.
- [294] M. N. Golovin, D. P. Wilkinson, J. T. Dudley, D. Holonko, and S. Woo. Applications of Metallocenes in Rechargeable Lithium Batteries for Overcharge Protection. *Journal of The Electrochemical Society* **1992**, 139, 5.
- [295] J. Dahn, J. Jiang, L. Moshurchak, M. Fleischauer, C. Buhrmester, and L. Krause. High-Rate Overcharge Protection of LiFePO_4 -Based Li-Ion Cells Using the Redox Shuttle Additive 2,5-Ditertbutyl-1,4-dimethoxybenzene. *Journal of the Electrochemical Society* **2005**, 152, A1283.

List of publications

Jonas Klein, Seyyed Mohsen Beladi-Mousavi, Marco Schleutker, Dereje Hailu Taffa, Markus Haase, and Lorenz Walder, "Photo-Electrochemical Device Enabling Luminescence Switching of LaPO₄:Ce,Tb Nanoparticle Layers", *Advanced Optical Materials* **2021**, 9, 2001891.

Jonas Klein, Alexander Hein, Ellen Bold, Fatih Alarслан, Egbert Oesterschulze, and Markus Haase, "Intercalation-free, fast switching of mesoporous antimony doped tin oxide with cathodically coloring electrochromic dyes", *Nanoscale Advances* **2022**, 4, 2144.

Jonas Klein, Fatih Alarслан, Martin Steinhart, and Markus Haase, "Cerium-Modified Mesoporous Antimony Doped Tin Oxide as Intercalation-Free Charge Storage Layers for Electrochromic Devices", *Advanced Functional Materials* **2022**, 4, 2210167.

Jonas Klein, Michael Philippi, Fatih Alarслан, Tim Jähnichen, Dirk Enke, Martin Steinhart, and Markus Haase, "Dispersible SnO₂:Sb and TiO₂ Nanocrystals After Calcination at High Temperature", *Small* **2023**, 19, 2207674.

Marius Ciobanu, Jonas Klein, Maleen Middendorf, Seyyed Mohsen Beladi Mousavi, Frederike Carl, Markus Haase, and Lorenz Walder, "High contrast hybrid electrochromic film based on cross-linked phosphonated triarylamine on mesoporous antimony doped tin oxide", *Solar Energy Materials and Solar Cells* **2019**, 203, 110186.

Seyyed Mohsen Beladi-Mousavi, Jonas Klein, Bahareh Khezri, Lorenz Walder, and Martin Pumera, "Active Anion Delivery by Self-Propelled Microswimmers", *ACS Nano* **2020**, 14, 3434.

Alexander Hein, Nikolas Longen, Carsten Kortz, Frederike Carl, Jonas Klein, Markus Haase, and Egbert Oesterschulze, "Two-dimensional spatial image control using an electrochromic graduated filter with multiple electrode configuration", *Solar Energy Materials and Solar Cells* **2020**, 215, 110549.

Alexander Hein, Nikolas Longen, Frederike Carl, Jonas Klein, Markus Haase, Roman Stoll, Renate Warmers, Gerald Jenke, Christoph Gimmler, Theo Schotten, Michael

List of publications

Haag-Pichl, and Egbert Oesterschulze , "Electrochromic graduated filters with symmetric electrode configuration", *Optics Express* **2020**, 28, 17047.

Seyyed Mohsen Beladi-Mousavi, Shamaila Sadaf, Ann-Kristin Hennecke, Jonas Klein, Arsalan Mado Mahmood, Christian Rüttiger, Markus Gallei, Fangyu Fu, Eric Fouquet, Jaime Ruiz, Didier Astruc, and Lorenz Walder, "The Metallocene Battery: Ultrafast Electron Transfer Self Exchange Rate Accompanied by a Harmonic Height Breathing", *Angewandte Chemie International Edition* **2021**, 60, 13554.

Leiming Guo, Jonas Klein, Jannis Thien, Michael Philippi, Markus Haase, Joachim Wollschläger, and Martin Steinhart, "Phenolic Resin Dual-Use Stamps for Capillary Stamping and Decal Transfer Printing", *ACS Applied Materials and Interfaces* **2021**, 13, 49567.

Seyyed Mohsen Beladi-Mousavi, Jonas Klein, Marius Ciobanu, Shamaila Sadaf, Arsalan Mado Mahmood, and Lorenz Walder, "Flexible, Self-Supported Anode for Organic Batteries with a Matched Hierarchical Current Collector System for Boosted Current Density", *Small* **2021**, 17, 2103885.

Fatih Alarслан, Laura Vittadello, Jonas Klein, Qaiser Ali Khan, Christian Kijatkin, Markus Haase, Helmut Schäfer, Mirco Imlau, and Martin Steinhart, "Thin Patterned Lithium Niobate Films by Parallel Additive Capillary Stamping of Aqueous Precursor Solutions", *Advanced Engineering Materials* **2022**, 24, 2101159.

Fatih Alarслан, Martin Frosinn, Kevin Ruwisch, Jannis Thien, Tim Jähnichen, Louisa Eckert, Jonas Klein, Markus Haase, Dirk Enke, Joachim Wollschläger, Uwe Beginn, and Martin Steinhart, "Reactive Additive Capillary Stamping with Double Network Hydrogel-Derived Aerogel Stamps under Solvothermal Conditions", *ACS Applied Materials and Interfaces* **2022**, 14, 44992.

Declaration of authorship

I hereby declare that the presented thesis was prepared entirely on my own. Outside sources were not used without an explicit declaration in the text. The following persons contributed to this work:

- Simona Webersinn (Universität Osnabrück) synthesized redox dyes and redox shuttles
- Fatih Alarslan (Universität Osnabrück) recorded SEM images and performed EDX analysis
- Dr. Michael Philippi (Universität Osnabrück) recorded SEM images and assisted with supercritical drying of gels
- Henning Eickmeier (Universität Osnabrück) recorded TEM images
- Anja Schuster (Universität Osnabrück) performed XRF analysis
- Tim Jähnichen (Universität Leipzig) performed nitrogen sorption measurements
- Dr. Alexander Hein (Technische Universität Kaiserslautern) performed characterization of an electrochromic device

I have not attempted a promotion before, and this work was not presented to any other institution before.

.....
(place, date)

.....
(signature)